PULSED ELECTRICALLY AND OPTICALLY DETECTED MAGNETIC RESONANCE SPECTROSCOPY OF DISORDERED SEMICONDUCTORS

by

Sang-Yun Lee

A dissertation submitted to the faculty of
The University of Utah
in partial fulfillment of the requirements for the degree of

Doctor of Philosophy

in

Physics

Department of Physics and Astronomy

The University of Utah

August 2011

The University of Utah Graduate School

STATEMENT OF DISSERTATION APPROVAL

The dissertation of **Sang-Yun Lee**

has been approved by the following supervisory committee members:

Christoph Boehme	, Chair	**June 9, 2011** Date Approved
Z. Valy Vardeny	, Member	**June 9, 2011** Date Approved
Mikhail Raikh	, Member	**June 9, 2011** Date Approved
Stephan LeBohec	, Member	**June 9, 2011** Date Approved
Michael H. Bartl	, Member	**June 9, 2011** Date Approved

and by **David Kieda** , Chair of

the Department of **Physics and Astronomy**

and by Charles A. Wight, Dean of The Graduate School.

ABSTRACT

Electrically and Optically detected magnetic resonance (EDMR and ODMR) spectroscopy allows investigation of the microscopic nature of paramagnetic centers which influence the electrical or optoelectronic properties of semiconductors. Traditionally, EDMR and ODMR have been conducted as adiabatic magnetic field sweep spectroscopies under continuous wave (cw) application of electromagnetic fields. It is shown here that information about the dynamics of spin–dependent processes obtained from cwEDMR and cwODMR is determined by many electronic- and spin-relaxation parameters, which make the interpretation of experimental data quantitatively ambiguous. In contrast, it is shown that transient EDMR and ODMR experiments, so called pulsed (p)EDMR and pODMR, are significantly less ambiguous. For spin-dependent processes based on intermediate pairs of paramagnetic states, the cwEDMR and cwODMR as well as pEDMR and pODMR dynamics are derived analytically and the application of these results for the interpretation of experimental data is discussed for two examples: (i) The pEDMR study of spin-dependent recombination in silicon rich hydrogenated amorphous silicon nitride (a-SiN_x:H) which showed the presence of a variety of mechanisms such as dangling bond recombination through weakly spin-coupled paramagnetic states but also recombination through band tail states which were strongly dipolar or exchange coupled. These processes had previously been observed in hydrogenated amorphous silicon (a-Si:H). However, while in a-Si:H, these processes took place solely as geminate recombination, they were of nongeminate nature in the a-SiN_x:H. (ii) The pODMR study of excitonic recombination in a π-conjugated polymer, namely, poly[2-methoxy-5-(20-ethyl-hexyloxy)-1,4-phenylene vinylene] (MEH-PPV). The presence of magnetic resonance induced spin–beat oscillations in the fluorescence intensity was confirmed. Based on the existing polaron–pair recombination model, previously pEDMR–detected beat signals seen here with pODMR in an identical manner. Two types of MEH-PPV, one fully hydrogenated and one partially deuterated were subjected to pODMR. The deuterated materials showed a different beat oscillation dependence of the driving field power pattern which was indicative of smaller hyperfine fields in the deuterated material.

To my wife, Seoyoung Paik.

CONTENTS

LIST OF FIGURES

LIST OF TABLES

ACKNOWLEDGMENTS

I would like to express my gratitude to the people who have been my mentors, advisor, and colleagues during my Ph.D. studies:

I especially thank Prof. Dr. Christoph Boehme who has been my advisor as well as a mentor. He has always encouraged me to overcome many obstacles that I have faced during my studies. And his deep understanding about physics, enthusiasm, and energy always have inspired me. I would like to remark that whenever I knocked on his office door for discussions, I stepped out of his office full of satisfaction.

Dr. Dane McCamey, who had been a postdoctoral researcher in Christoph Boehme's group, showed me how creativity leads to successful scientific research. Discussions with him were always fun and (of course) useful.

Seoyoung Paik, one of my best colleagues and my beloved wife, has always worked with me whenever I had to sit up for very long experiments. She made a most significant contribution to new sample holder which was essential for any pEDMR experiments. Discussions with her always revealed what I didn't know and what I had to study further. Especially she has been my faithful supporter whenever I lost my confidence.

Prof. Dr. John Lupton's comprehensive knowledge has helped me a lot for organic semiconductor research.

Prof. Valy Vardeny, prof. Mikhail Raikh, prof. Stephan Lebohec, and prof. Michael H. Bartl have gladly participated in my supervisory committee and provided me with advice.

I also would like to thank my colleagues: Willian Baker made a contribution for building a new sample holder which has been a prerequisite for pEDMR experiments. Kipp van Schooten kindly prepared organic samples for pODMR experiments.

Finally, I would like to thank my parents and brother who have provided me continuous and firm support while studying abroad.

CHAPTER 1

INTRODUCTION

Properties of electron spins such as the Landé g-factor or the magnetic resonance linewidth are highly dependent on their microscopic environment and local interaction such as with neighbor electron spins, adjacent nuclear magnetic moments, and even their own motion which can result in spin-orbit coupling [1]. One of the most frequently used methods to detect electron spin properties is Electron Spin Resonance (ESR). An electron spin subjected to a static magnetic field (B_0 field) can be in one of two eigenstates which are degenerate in the absence of a magnetic field but nondegenerate due to Zeeman interaction in the presence of a magnetic field. Resonance occurs when the electron absorbs or emits electromagnetic waves whose energy is equal to the energy difference between the split states. Many charge carrier recombination centers in semiconductors possess a spin, they are paramagnetic. Because of this, they are detectable by ESR and since their ESR signals are affected by surrounding environments, ESR has widely been used to study their microscopic nature [2–7].

Most electronic and optoelectronic devices use properties such as charge transport, photoconductivity, photo- and electro-luminescence, or quantum efficiency for technical applications. For many of these materials, the electron spin degree of freedom is not of significance, because of the minute energy scales of electron spin states. However, in some materials with weak spin-orbit coupling, spin properties can determine macroscopic electrical or optical materials properties due to spin-selection rules [8–11]. For these materials, an understanding of the properties of paramagnetic centers as well as their spin- and electronic dynamics is of profound importance for the understanding of the materials behavior.

The first ESR experiment, which also happened to be the first ever magnetic resonance experiment, was reported by Zavoisky [12] in 1945. Since then, many related techniques have been developed: nuclear magnetic resonance spectroscopy (NMR) [13, 14], pulsed ESR [15], pulsed NMR [16, 17], spin echo techniques [15, 16], double magnetic resonance methods such electron-electron double resonance (ELDOR) [18], electron nuclear double resonance (ENDOR) [19] and many others. All these methods follow a common detection

scheme which is based on the emission or absorbtion of electromagnetic radiation from a given spin system. Due to the weak polarization of both electron and nuclear spin systems, magnetic resonance is therefore a comparatively insensitive approach: Conventional ESR is typically limited to a detection limit of 10^{10} spins. Moreover, when electronic processes involving paramagnetic centers are investigated using ESR, it is oftentimes hard to figure out whether an observed ESR signal actually represents the paramagnetic centers involved in the investigated processes or whether it represents other spins under which the signal of interest is buried. For instance, the ESR spectroscopy of bulk crystalline silicon without an extensive surface preparation reveals almost no information about the paramagnetic centers in these materials because any ESR spectrum obtained from a small silicon crystal will be dominated by very strong signals from crystalline silicon surface states [20]. In addition to this problem, pure ESR spectroscopy is also oftentimes not sensitive enough for semiconductor samples, especially when the investigated materials are available only as thin films. The inherent volume sensitivity of magnetic resonance spectroscopy is a great detriment for the investigation of low dimensional materials systems.

The disadvantages of conventional magnetic resonance spectroscopy can be overcome by direct observation of those macroscopic observables which are influenced by spin-dependent processes. By combining conventional ESR with the detection of luminescence, absorption or electric conductivity, a vast amount of information about localized paramagnetic states and the way they influence optical and electrical properties is obtained. These methods are referred to as optically (ODMR) and electrically (EDMR) detected magnetic resonance. First ODMR experiment were carried out by Geschwind et al. in 1959 [21]. A few years thereafter, in 1965, the first EDMR experiment was carried out by Maxwell and Honig [22]. Since then, EDMR and ODMR experiments were performed on many different electronic systems in a broad range of materials systems [23–46]. Most of these studies have been carried out as continuous wave (cw) ODMR or EDMR experiments which are adiabatic field sweep experiments where the spin spectrum is obtained by a gradual sweep of a magnetic field in presence of continuously irradiated electromagnetic radiation with constant frequency and intensity. This experimental approach is simple and it allows us to obtain Landé g-factors of paramagnetic states contributing to luminescence and conductivity. It also gives access to magnetic resonance lineshapes which contain information about disorder, spin-interactions, as well as electronic- and spin relaxation times. This broad range of experimental parameters influencing ODMR and EDMR measurement, is at the same time the origin of the limitations of these methods: Significant uncertainty typically arises for

most cw ODMR and EDMR spectra, because there are too many factors influencing the lineshapes and resonance positions of ESR spectra. Therefore, lineshape analysis can frequently provide ambiguous information especially when complex superpositions of lineshapes due to many overlapping spin signals with a distribution of electron- and spin-dynamics are present in a given semiconductor sample.

Conventional ODMR and EDMR are traditionally performed as magnetic field or radiation field modulated experiments, with subsequent Lock-in detection. This approach allows for an optimized noise suppression yet it also implies, that only one particular frequency component of the investigated spin-dependent processes is detected, namely the component whose frequency is equal to the experimentally chosen modulation frequency. This aspect can be utilized to gradually scan the entire dynamics of ODMR or EDMR detected spin-dependent signals, simply by a gradual measurement of the modulation frequency dependence of an observed spin-dependent signal.

Similar to the modulation frequency dependence scan for cw ODMR and EDMR experiments, the dynamics of spin-dependent processes can also be observed by a direct transient (broad band) measurement. Similar to conventional magnetic resonance spectrocopies, this time dependent measurement approach has evolved in recent years towards so called pulsed (p) ODMR and EDMR spectroscopies. PODMR and pEDMR are not just the time domain equivalent of cw ODMR and cw EDMR. In contrast to those techniques, pODMR and pEDMR employ very strong electromagnetic pulses in order to manipulate the investigated spin states on very short times scales, much shorter than any spin- or electronic relaxation time of the excited species. On these time scales, the spins will therefore propagate coherently, which means they will propagate deterministically in a way that depends on their Hamiltonians. The observation of coherent spin motion therefore opens up direct access to a spins' Hamiltonian and, thus, a broad range of information about its nature.

This dissertation consists of four main parts, which represent, (i) a study of the experimental limitations of the conventional cw ODMR and cw EDMR techniques, (ii) a study of how the pODMR and pEDMR techniques can overcome these limitations as well as applications of pEDMR (iii) and pODMR (iv) to disordered materials spectroscopy which demonstrated how these modern experiments can lead to new insights into the nature of macroscopic optical and electronic properties of an amorphous inorganic semiconductor and an organic semiconductor, respectively.

The results of the work presented in the following led to the first all-analytical description of cw ODMR and EDMR experiments which revealed that fits of experimentally

observed modulation frequency dependence measurements determined by electronic and spin-relxation parameters are profoundly ambiguous and that previously made assignments based on this approach may not be accurate. In contrast, the investigation of the dynamics of pODMR and pEDMR experiments showed that due to the enhanced access to experimental parameters, these methods are inherently less ambiguous. The application of pEDMR for the investigation of hydrogenated silicon rich amorphous silicon nitride then showed that a broad range of qualitatively and quantitatively different spin-dependent processes is present in this material and that the observation of these processes gives important insight into the optoelectronic properties of this material and their potential applicability for photovoltaic and photoelectrochemical device applications. Finally, the application of pODMR to the investigation of spin-dependent processes in a π-conjugated polymer confirmed the previously reported [47] but at the same time disputed [44] spin-dependent exciton formation process, namely the so called polaron pair process which describes the formation of strongly exchange coupled excitonic states through initial formation of weakly spin-coupled excitonic precursor states, so called polaron pairs. This insight is of significance due to the extraordinary technological importance of exciton processes in organic semiconductors for light emitting and photovoltaic devices.

1.1 References

[1] N. M. Atherton. *Principles of electron spin resonance*. Ellis Horwood series in physical chemistry. Ellis Horwood, Chichester, 1993.

[2] R. C. Fletcher, W. A. Yager, G. L. Pearson, and F. R. Merritt. *Physical Review*, 95:844, 1954.

[3] G. Feher, R. C. Fletcher, and E. A. Gere. *Physical Review*, 100:1784, 1955.

[4] D. J. Lépine. *Physical Review B*, 2:2429, 1970.

[5] M. H. Brodsky and R. S. Title. *Physical Review Letters*, 23:581, 1969.

[6] P. A. Thomas, M. H. Brodsky, D. Kaplan, and D. Lepine. *Physical Review B*, 18:3059, 1978.

[7] M. Stutzmann, W. B. Jackson, and C. C. Tsai. *Physical Review B*, 32:23, 1985.

[8] M. Reufer, M. J. Walter, P. G. Lagoudakis, A. B. Hummel, J. S. Kolb, H. G. Roskos, U. Scherf, and J. M. Lupton. *Nature Materials*, 4:340 – 346, 2005.

[9] M. Wohlgenannt and Z. V. Vardeny. *Journal of Physics: Condensed Matter*, 15:R83, 2003.

[10] J. S. Wilson, A. S. Dhoot, A. J. A. B. Seeley, M. S. Khan, A. Kohler, and R. H. Friend. *Nature*, 413:828–831, 2001.

[11] K. Held, E. Eisenberg, and B. L. Altshuler. *Physical Review Letters*, 90:106802, 2003.

[12] E. Zavoiski. *Journal of Physics USSR*, 9:211, 1945.

[13] F. Bloch, W. W. Hansen, and M. Packard. *Physical Review*, 70:474, 1946.

[14] E. M. Purcell, H. C. Torrey, and R. V. Pound. *Physical Review*, 69:37, 1946.

[15] R. J. Blume. *Physical Review*, 109:1867, 1958.

[16] E. L. Hahn. *Physical Review*, 80:580, 1950.

[17] R. R. Ernst and W. A. Anderson. *Review of Scientific Instruments*, 37:93–102, 1966.

[18] K. D. Bowers and W. B. Mims. *Physical Review*, 115:285, 1959.

[19] G. Feher. *Physical Review*, 103:834, 1956.

[20] P. M. Lenahan and J. J. F. Conley. *Journal of Vacuum Science and Technology B*, 16:2134–2153, 1998.

[21] S. Geschwind, R. J. Collins, and A. L. Schawlow. *Physical Review Letters*, 3:545, 1959.

[22] R. Maxwell and A. Honig. *Physical Review Letters*, 17:188, 1966.

[23] D. K. Biegelsen, J. C. Knights, R. A. Street, C. Tsang, and R. M. White. *Philosophical Magazine Part B*, 37:477–488, 1978.

[24] K. Morigaki, D. J. Dunstan, B. C. Cavenett, P. Dawson, J. E. Nicholls, S. Nitta, and K. Shimakawa. *Solid State Communications*, 26:981–985, 1978.

[25] D. J. Dunstan and J. J. Davies. *Journal of Physics C: Solid State Physics*, 12:2927–2944, 1979.

[26] B. C. Cavenett. *Advances in Physics*, 30:475–538, 1981.

[27] R. A. Street. *Physical Review B*, 26:3588–3604, 1982.

[28] F. Boulitrop. *Physical Review B*, 28:6192, 1983.

[29] E. v. Oort, N. B. Manson, and M. Glasbeek. *Journal of Physics C: Solid State Physics*, 21:4385, 1988.

[30] L. S. Swanson, J. Shinar, and K. Yoshino. *Physical Review Letters*, 65:1140, 1990.

[31] L. S. Swanson, J. Shinar, A. R. Brown, D. D. C. Bradley, R. H. Friend, P. L. Burn, A. Kraft, and A. B. Holmes. *Physical Review B*, 46:15072, 1992.

[32] B. Stich, S. Greulich-Weber, and J. M. Spaeth. *Journal of Applied Physics*, 77:1546–1553, 1995.

[33] E. R. Glaser, T. A. Kennedy, K. Doverspike, L. B. Rowland, D. K. Gaskill, J. A. Freitas, M. Asif Khan, D. T. Olson, J. N. Kuznia, and D. K. Wickenden. *Physical Review B*, 51:13326, 1995.

[34] V. Dyakonov, G. Rösler, M. Schwoerer, and E. L. Frankevich. *Physical Review B*, 56:3852, 1997.

[35] E. Lifshitz, L. Bykov, M. Yassen, and Z. Chen-Esterlit. *Chemical Physics Letters*, 273:381–388, 1997.

[36] M. S. Brandt, M. W. Bayerl, M. Stutzmann, and C. F. O. Graeff. *Journal of Non-Crystalline Solids*, 227-230:343–347, 1998.

[37] V. Dyakonov and E. Frankevich. *Chemical Physics*, 227:203–217, 1998.

[38] T. Eickelkamp, S. Roth, and M. Mehring. *Molecular Physics: An International Journal at the Interface Between Chemistry and Physics*, 95:967–972, 1998.

[39] E. Lifshitz, A. Glozman, I. D. Litvin, and H. Porteanu. *The Journal of Physical Chemistry B*, 104:10449–10461, 2000.

[40] M. Stutzmann, M. S. Brandt, and M. W. Bayerl. *Journal of Non-Crystalline Solids*, 266-269:22, 2000.

[41] A. P. Nizovtsev, S. Y. Kilin, C. Tietz, F. Jelezko, and J. Wrachtrup. *Physica B: Condensed Matter*, 308-310:608–611, 2001.

[42] L. Langof, E. Ehrenfreund, E. Lifshitz, O. I. Micic, and A. J. Nozik. *Journal of Physical Chemistry B*, 106:1606–1612, 2002.

[43] E. J. W. List, U. Scherf, K. Müllen, W. Graupner, C. H. Kim, and J. Shinar. *Physical Review B*, 66:235203, 2002.

[44] M. Segal, M. A. Baldo, M. K. Lee, J. Shinar, and Z. G. Soos. *Physical Review B*, 71:245201, 2005.

[45] C. G. Yang, E. Ehrenfreund, and Z. V. Vardeny. *Physical Review Letters*, 99:4, 2007.

[46] T. D. Nguyen, G. Hukic-Markosian, F. Wang, L. Wojcik, X.-G. Li, E. Ehrenfreund, and Z. V. Vardeny. *Nature Materials*, 9:345–352, 2010.

[47] D. R. McCamey, K. J. v. Schooten, W. J. Baker, S.-Y. Lee, S.-Y. Paik, J. M. Lupton, and C. Boehme. *Physical Review Letters*, 104:017601, 2010.

CHAPTER 2

UNDERSTANDING THE MODULATION FREQUENCY DEPENDENCE OF CONTINUOUS WAVE EDMR AND ODMR SPECTROSCOPIES

Electron spin resonance (ESR) is a useful tool for the investigation of microscopic properties of paramagnetic states in a wide variety of materials. In conventional ESR experiments, the total polarization of the investigated spin ensemble is observed by the measurement of microwave absorption. In some materials, there are other observables which can be used to detect electron spin states. For instance, when electron spins control electronic transitions such as transport or recombination, macroscopic materials properties such as photoluminescence, electroluminescence or conductivity can change under spin resonance. The advantage of these electrically detected magnetic resonance (EDMR) and optically detected magnetic resonance (ODMR) spectroscopies is that they are significantly more sensitive than conventional ESR (spin polarization is usually low and single microwave photons can not be detected), and these methods provide a direct insight into how paramagnetic states in semiconductors affect some of the technologically most widely used electrical and optical materials properties. ODMR has been used in a wide range of research areas since its first invention [1, 2]. ODMR and EDMR are about 8 to 9 orders more sensitive than ESR, they both are proven to have single spin sensitivity ESR [3–7], and they both can directly link a paramagnetic center to a specific luminescence center [3–5, 8]. Thanks to these advantages, ODMR can be used to deconvolute unresolved, overlapping luminescence bands in semiconductors [9]. EDMR provides information about electronically active paramagnetic centers in a similar way, again with higher sensitivity than ESR [7, 10]. In the early stage (until about the 1980s), ODMR was mainly conducted on inorganic semiconductors to identify paramagnetic recombination centers and to investigate their spin-dependent processes [3, 11]. ODMR played an important role in investigating spin-dependent processes

especially in amorphous silicon (a-Si) and revealed a variety of defect states which influence recombination in a-Si [4, 5, 9, 12–15].

Continuous wave ODMR and EDMR (cwODMR and cwEDMR) have been used in a wide range of research fields: They have been used to investigate spin-dependent transitions involving phosphorous donors in crystalline silicon [10, 16], trapping centers and their recombination dynamics in nanocrystals [6, 17–19], transport and recombination in microcrystalline hydrogenated silicon [20], GaN [21, 22], and SiC [23], and spin-dependent recombination in nitrogen vacancy centers in diamond [24–26]. Because cwODMR and cwEDMR can be used to distinguish overlapping recombination bands and their dynamics in disordered materials, they have also been used to investigate (usually amorphous) organic semiconductors: cwODMR and cwEDMR have provided information about spin-pairs dominating electronic processes and their transitions in conducting polymers [27–38], small molecules [39–41], and polymer or small molecule/fullerene blends [42, 43]. The effect of isotopic modification on magnetic field effects in organic semiconductors also has been observed by ODMR [44], and the intersystem-crossing time has been extracted from the modulation frequency dependence [45].

Experimentally, cwODMR and cwEDMR are similar to conventional ESR except that luminescence intensity and electric current are picked up instead of the microwave absorption. Two magnetic fields, a static field B_0 and oscillating field B_1, are applied to a sample with $B_0 \perp B_1$. The frequency of the sinusoidal B_1 field is matched with the Larmor frequency of the paramagnetic center to satisfy the resonance condition. As for most ESR spectrometers, X-band ($\approx$ 9.7GHz) is used, a frequency in the microwave (MW) range. In the case of cwODMR, to allow for optical detection, optical or electrical excitation of electronic states is necessary. Depending on the excitation method, photoluminescence detected magnetic resonance (PLDMR) or electroluminescence detected magnetic resonance (ELDMR) can be performed. In the case of PLDMR, constant optical excitation is applied using, for example, a Laser, and the resulting photoluminescence (PL) is detected. To increase the signal to noise ratio, lock-in detection is oftentimes employed. Two different modulation methods can be used. One method involves modulation of the static magnetic field, B_0, as used for conventional cwESR. The other approach is based on the modulation of the MW amplitude. Experimentally, B_0 modulation has been found to give weaker signals than MW amplitude modulation [3]. Square modulation of the microwaves at a fixed reference frequency is generally used. The PL intensity reflecting the varying MW amplitude is then fed into a lock-in amplifier, and both in-phase and out-of-phase signals are obtained. In

some studies found in the literature [20, 29, 37, 40, 46], the out-of-phase signal are ignored. However, doing so can result in the loss of important information, as will be explained later.

When the optical excitation is modulated with the same reference frequency as the MW, a double modulated PLDMR (DM-PLDMR) becomes possible [37]. An experimental setup for a MW modulated ODMR experiment is shown in Fig. 2.1. For EDMR, the optical detection is replaced by a current measurement. The metallic contacts needed for this require a design that prevents the distortion of the MW field.

In both cwEDMR and cwODMR, the responses of the observables to the induced magnetic resonances are determined by the underlying electronic processes. The time scales on which these processes occur depend on various experimental parameters, such as excitation density [4, 5, 12, 40, 47, 48] (or an injection current for EDMR [29, 40]), temperature [4, 9, 29, 40], and MW power (equivalently B_1 field strength) [4, 5, 11, 16–19, 25, 39, 42, 45, 49–52]. The dependencies of cwODMR and cwEDMR signals on these parameters can allow us to distinguish overlapping transitions and to understand their dynamics. For cwODMR, spectral information also can provide additional information to distinguish overlapping luminescence bands [4, 9, 25].

Another experimental parameter that can influence the observed cwODMR and cwEDMR signals is the modulation frequency, as the lock-in detected signals depend on the transient responses to the modulated MW [4, 9, 12, 19, 53]. Modulation frequency effects have often been ignored in the literature, and, as a result, studies often reported results obtained using only one (or a small number of) modulation frequencies (usually the one which maximized the obtained signal). One can, however, find a number of reports showing modulation frequency dependence. Different signals at different modulation frequencies were reported for the first time by Biegelsen et al. [50]. Other investigators have noticed that modulation frequency effects play an important role in the observed signal, which can change drastically as a function of the modulation frequency [3, 9, 12]. Qualitative reports of modulation frequencies dependencies can be found in the early ODMR and EDMR literature [3, 9, 13] which were sometimes used to identify the overlap of separate spin-dependent signals [5]. Even so, very little systematic research into modulation frequency effects was undertaken before the late 1990s, when research into this question became more common [18, 19, 25, 30, 36–38, 45, 47, 48].

A number of researchers have attempted to understand modulation frequency effects by developing rate models. Dunstan and Davies were the first to develop solutions for ODMR transients [11]. Next, Street and Depinna et al. developed rate models and found transient

solutions [4, 12]. Lenahan et al. explained their observed modulation frequency dependence using a simple rate model described by only one time constant [14]. A number of studies based on the steady-state solutions of such rate models have been reported [16, 17, 47, 49, 51]. However, to understand the modulation frequency effects the exact solutions for the frequency dependence are necessary. There have been a number of efforts to find the solutions for modulation frequency dependence [6, 19, 30, 36–38, 42, 45, 48]. However, no closed form analytical solutions have been reported, and important aspects of modulation frequency effects remain not well understood. This has led to a number of debates regarding the underlying physical mechanisms of cwODMR and cwEDMR signals, because modulation frequency dependencies observed by different groups on similar systems have sometimes led to completely different spin-dependent transition models. For example, the source of the signal seen in organic semiconductors has been attributed to both a spin-dependent polaron model [38, 45, 54] and a triplet exciton-polaron quenching model [36, 37, 53].

Lock-in detected cwODMR and cwEDMR signals can be either positive or negative depending on the shapes of transient responses [4, 9, 12, 19, 53]. A variety of spin-dependent models have been developed based on the observed signs of cwODMR and cwEDMR signals as well as experimental parameters, like pair generation rates, temperature, MW power, and modulation frequency. Examples for such studies exist for a-si [4, 5, 7, 9, 9, 11–13, 15, 50, 55], InP nanocrystal [19], II-IV semiconductor quantum dots [18], PbI_2 nanoparticles [17], and organic semiconductors [29, 30, 33, 34, 36, 38, 41, 43, 47, 48]. For instance, it has been generally accepted that radiative and nonradiative recombination result in enhancement and quenching of cwODMR signals, respectively [5, 7, 17, 56], and all recombination processes and all detrapping processes result in quenching and enhancement of cwEDMR signals, respectively [7, 56]. The qualitative explanation for signs of cwODMR signals is as follows: spin resonance induces mixing between triplet and singlet pairs, and because initial states are generally dominated by triplet pairs due to the fast recombination of singlet pairs, the number of singlet pairs is increased at resonance. Thereby, the overall transition rate increases [7]. Some studies even conclude that a certain channel is radiative or nonradiative, based on the sign of the ODMR signal [4, 9, 12, 55]. The idea here is that when a nonradiative recombination process is enhanced under spin-resonance, the competing optically detected radiative channels must be quenched.

The above examples show how critical it is to understand how MW modulation affects the observed cwODMR and cwEDMR signals. In this report, we employ the widely accepted spin-dependent transition model based on weakly coupled electron-hole pairs [57], and find

its closed-form analytical solutions. We then use this solution to explain how a broad range of electronic transitions, including recombination, dissociation, intersystem-crossing, pair generation, and spin-flip can affect the cwODMR and cwEDMR signals. We show how serious ambiguities related to the modulation frequency dependencies can arise, which make it difficult to determine the fundamental physical processes responsible for the observed cwEDMR or cwODMR frequency dependence. For example, extensive ODMR studies have been conducted on organic semiconductors to determine their dominant recombination processes. A variety of models have been suggested based on the observations of the signs of cwODMR and cwEDMR such as the singlet exciton quenching model [34, 36, 47], the triplet-triplet annihilation model [48], the polaron-to-bipolaron decay [29, 33], and the polaron pair recombination [38]. We show that most in many cases, the modulation frequency dependence cannot be used for such assignments, since the sign of these signals can be negative or positive for both radiative or nonradiative processes. This ambiguity is one of the reasons why cwODMR and cwEDMR spectroscopies have been increasingly substituted by transient, pulsed EDMR and ODMR techniques which will be discussed in the following chapters [58–66].

2.1 Models for the description of spin-dependent transition rates

The first quantitative model explaining spin-dependent recombination was suggested by Lepin [67] who described a thermal polarization model which predicted a relative change in photoconductivity of less than 10^{-6} at 300 K for X-band ESR. Microwave frequency and temperature dependencies were also predicted. However, it turned out that this model could neither explain the signal intensity of more than 10^{-3} that was observed in undoped a-Si:H at R.T. [67], and the very weak dependencies on microwave frequency [68] and temperature [15, 69]. These problems were soon resolved by another model developed by Kaplan, Solomon and Mott (KSM model) [57]. In the KSM model, intermediate pair states exist prior to a spin-dependent transition and the spin pair states may recombine or dissociate. In addition, it is assumed that spin pairs in the triplet state can be annihilated only when one of pair partners is flipped by the spin-lattice relaxation process or the induced ESR otherwise pairs dissociate. Thus, the recombination of triplet pairs happens only when they experience a transition to the singlet state.

In the past decades, a number of refinements were introduced to the KSM model, in which spin-spin interactions such as exchange and dipolar interactions exist within the pair, and spin-orbit coupling that is weak but not negligible is permitted such that weak triplet

transitions become possible [59]. Because the intermediate pairs, consisting of two spins with s=1/2, can experience spin-spin interactions, the pair eigenbasis consists in general of two parallel states ($|T_+\rangle$ and $|T_-\rangle$) and two mixed states ($|2\rangle$ and $|3\rangle$) which change continuously from $|\uparrow\downarrow\rangle$ and $|\downarrow\uparrow\rangle$ to $|S\rangle$ and $|T_0\rangle$, respectively, as the spin-spin interaction increases. ESR can induce transitions of $|T_+\rangle \leftrightarrow |\uparrow\downarrow\rangle$, $|T_-\rangle \leftrightarrow |\uparrow\downarrow\rangle$, $|T_+\rangle \leftrightarrow |\downarrow\uparrow\rangle$, and $|T_-\rangle \leftrightarrow |\downarrow\uparrow\rangle$. Thus, when the spin-spin interaction is weak, there can appear transitions among all four eigenstates, and the transition probabilities are functions of the spin-spin interaction strength. Note that transitions of $|\downarrow\uparrow\rangle \leftrightarrow |\uparrow\downarrow\rangle$ are ESR forbidden but possible due to T_1 relaxation, and $|2\rangle \leftrightarrow |3\rangle$ transitions are possible via mixed relaxation processes. To understand the change of spin pair densities by ESR induced transitions, a mathematical approach will be given. Boehme and Lips have found the effective changes of spin densities by solving a Louville equations describing the propagation of a spin ensemble during an ESR excitation [59]. The density changes of each spin state are then given by,

$$\begin{aligned} \rho_{1,4}(\tau) &= \rho^0_{1,4}\Delta^u(\tau), \\ \rho_{2,3}(\tau) &= \rho^0_{2,3}\Delta^v(\tau) \pm \rho^0_{2,3}\frac{J+D}{\hbar\omega_\Delta}\Delta^w(\tau) \end{aligned} \tag{2.1}$$

where indices 1 and 4 represent the states $|T_+\rangle$ and $|T_-\rangle$, respectively, ρ^0_i is the initial density, J and D are the exchange and dipolar coupling constant, respectively, ω_Δ represents the half of the frequency separation between the states $|2\rangle$ and $|3\rangle$. $\Delta^u(\tau)$, $\Delta^v(\tau)$, and $\Delta^w(\tau)$ represent the ESR duration time (τ) dependencies. When the Larmor separation (which is the difference of the two Larmor frequencies within a pair) is larger than the applied B_1 field strength, only one pair partner can be flipped. In this case the τ dependencies become,

$$\begin{aligned} \Delta^v(\tau) &= \frac{\gamma^2 B_1^2}{\Omega^2}\sin^2(\frac{\Omega\tau}{2}) \equiv \Delta(\tau), \\ \Delta^u(\tau) &= 1-\Delta(\tau), \\ \Delta^w(\tau) &= 0 \end{aligned} \tag{2.2}$$

where $\Omega = 2\pi f$ represents the Rabi frequency of the flipped pair partner. Therefore, the density changes of each eigenstates become

$$\begin{aligned} \rho_{1,4}(\tau) &= \rho^0_{1,4}(1-\Delta(\tau)), \\ \rho_{2,3}(\tau) &= \rho^0_{2,3}\Delta(\tau). \end{aligned} \tag{2.3}$$

Because either one of the states 2 or 3 is always involved in a possible transition among four eigenstates, any transition will cause a decrease or increase of ρ_2 or ρ_3. Density changes in state 2 and 3 are equivalent to density changes of singlet and triplet pair states. Therefore we

don't need to deal with four state problems. Instead two pair densities of singlet and triplet pairs are enough to describe recombination processes as long as any coherent spin motion is not of interest. Note that this is a valid statement because modulation frequency is typically not faster than the time scale of coherent spin motions so that all coherent phenomena will be averaged out. An illustration of the resulting spin pair rate model is given in Fig. 2.2. Prior to a spin pair transition to a singlet state, it is in the intermediate pair state. This pair is created with a certain rate, G_s for a singlet pair and G_t for a triplet pair. If this process is due to optical generation of electron-hole pairs and spin-orbit coupling is infinitely small, G_t can be considered to be infinitely small. In the other case, if pair generation is achieved due to electrical injection of an electron and hole, G_t/G_t becomes three, because a pair will be created with a random spin configuration. The pair can recombine to an excitonic state with a recombination rate, r_s for a singlet pair and r_t for a triplet pair. This pair may dissociate into two free charge carriers without recombination. This happens at a dissociation rate, d_s for a singlet pair and d_t for a triplet pair. Before a pair recombines or dissociates, it can change its spin configuration from singlet to triplet or vice versa. This transition is possible via two spin mixing processes. One is intersystem-crossing, which is equivalent to a longitudinal spin relaxation process which can be defined as a "radiationless transition between two electronic states having different spin multiplicities" [70]. Intersystem-crossing rate is described by k_{ISC}. The other process is ESR induced spin-mixing as can be seen from eq. (2.2) and (2.3). This ESR-induced transition rate is given by α which is proportional to the microwave power ($\propto B_1^2$) and dependent on the spin-spin interaction controlled oscillator strength of the pair [71].

In the following section, a large number of quantitative models will be tested with analytical solutions for the observables of cwEDMR and cwODMR. Using realistic values for each transition probability, we consider experimentally relevant values for the cwODMR experiment. A wide range of transition rates have been reported. Examples include PL lifetimes in a-Si which span 11 decades from $10^{-9}\,s$ to $10^{2}\,s$ [72]; bound pair decay (e-h pair dissociation) life times of $5 \times 10^{-5}\,s$ in polymer-fullerene blends [73]; fluorescence life times of $2 \times 10^{-7}\,s$ and phosphorescence life times of $10^{-4}\,s$ in conjugated polymers [74]; microsecond-millisecond time scales of recombination in nanocrystalline TiO_2 thin films [75]; radiative decay rates of $10^6 \sim 10^7\,s^{-1}$, nonradiative decay rates of $10^9 \sim 10^{10}\,s^{-1}$, and dissociation rates of $10^7\,s^{-1}$ in organic semiconductors [76], and a lower limit of intersystem-crossing time of $10^{-5}\,s$ in organic semiconductors [77]. In the following work, we vary the electronic transition rates, including recombination, dissociation, intersystem-crossing, and

flip-flop, in the range between 10^{-4} and $10^{9}s^{-1}$ to cover as wide a range of experimentally observed parameters as possible.

2.1.1 Rate equations

CwODMR is fundamentally similar to conventional ESR spectroscopy - the one major modification is that the observable of ODMR is not the magnetization but the changes in the number of photons induced by ESR. Generally, a lock-in detected modulation of the B_0 or the B_1 field is used to enhance the resulting ODMR signal. For the B_1 field modulation, a square modulated microwave is continuously applied, and the responses to this excitation contain various harmonic frequency components. We will focus in the following on this kind of experiment.

Based on the rate model explained in Sec. 2.1, two coupled rate equations for the singlet and triplet pair densities can be written as below,

$$\frac{dn_s}{dt} = G_s - C_s n_s + \alpha(n_t - n_s) - k_{ISC}(n_s - \rho n_s) + k_{ISC}(n_t - (1-\rho)n_t), \tag{2.4}$$

$$\frac{dn_t}{dt} = G_t - C_t n_t + \alpha(n_s - n_t) - k_{ISC}(n_t - (1-\rho)n_t) + k_{ISC}(n_s - \rho n_s), \tag{2.5}$$

where ρ is the Fermi-Dirac distribution function, $\rho = (1 + e^{\frac{\Delta E}{kT}})^{-1}$, which approaches zero at low temperature and 1/2 at high temperature. It should be noted that α is turned on and off for each half cycle because of the square modulated microwave with frequency of 1/T. C_s and C_t are singlet and triplet pair annihilation rate coefficients, respectively. They consist of recombination and dissociation rate coefficients, $C_{s,t} = r_{s,t} + d_{s,t}$. Some aspects with regard to radiative and nonradiative recombination rate coefficients should be mentioned: For radiative recombination, the spatial correlation between the electron and the hole affects the transition probability so r_t and r_s are dependent on separation between an electron and hole [20, 78]. Therefore, because higher generation rate causes less separation, the radiative recombination probability is also a function of generation rate. However, this effect will not be considered in this report, as we assume that the average separation is larger than the localization radii of electrons and holes. Note that this transition corresponds to the radiative tunneling in hydrogenated amorphous silicon [78]. Nonradiative recombination includes all recombination processes which are not mediated by emission of photons, but phonons and hot carriers: phonon emission, Auger processes, surface and interface recombination, and recombination through defect states [79]. Nonradiative processes quench radiation efficiency in both organic semiconductors [80] and inorganic semiconductors [79]. As treated by List et al. [47] and Dyakonov et al. [46], we consider

both radiative and nonradiative recombination processes, and thus $C_s = (r_s + r_{s,nr} + d_s)$ and $C_t = (r_t + r_{t,nr} + d_t)$ where the subscript nr indicates nonradiative recombination.

Given the above definitions, the PL intensity and electric conductivity become

$$I \propto r_s n_s + r_t n_t, \tag{2.6}$$

$$\sigma \propto d_s n_s + d_t n_t. \tag{2.7}$$

It should be noted that nonradiative recombination behaves as pair annihilation process as other radiative recombination and dissociation, but they do not appear as proportionality constants in eq. 2.6 and eq. 2.7. In this section, only radiative recombination will be considered ($r_{s,nr}$, $r_{t,nr} = 0$) for simplicity and the contributions of nonradiative recombination will be discussed in Sec. 2.6.

Rate equations similar to eq. (2.4) and (2.5) can be found throughout the literature. However, usually only steady state solutions were found for the consideration of cwODMR and cwEDMR experiments [16, 47, 81]. In some cases, only the time dependence was considered [11, 12, 42]. Modulation frequency dependence solutions also have been reported, but there have been no reports of closed-form analytical solutions. Some solutions reported in the literature were obtained from a simplified rate model [14, 30, 48], some solutions were based on the steady state [36, 37], some solutions based on the rate model reported here were solely reported as numerical solutions [6, 19, 38, 45, 54], or the described observable was not the number of photons or electrons but total spin densities [30, 38, 45]. One solution given by Hiromitsu et al. was based on an assumed steady state for the half cycle where the MW is off [42].

The rate equations corresponding to eq. (2.4) and (2.5) are solved for the two separated time regions where the pulse is on and off, and the closed-form solutions can be explicitly expressed as:

$$n_{s1}(t) = A_{11}e^{-m_{11}t} + A_{21}e^{-m_{21}t} + n_{s1}^0, \tag{2.8}$$

$$n_{t1}(t) = B_{11}e^{-m_{11}t} + B_{21}e^{-m_{21}t} + n_{t1}^0, \tag{2.9}$$

$$n_{s2}(t) = A_{12}e^{-m_{12}\left(t-\frac{T}{2}\right)} + A_{22}e^{-m_{22}\left(t-\frac{T}{2}\right)} + n_{s2}^0, \tag{2.10}$$

$$n_{t2}(t) = B_{12}e^{-m_{12}\left(t-\frac{T}{2}\right)} + B_{22}e^{-m_{22}\left(t-\frac{T}{2}\right)} + n_{t2}^0, \tag{2.11}$$

where n_{s1} and n_{t1} are the singlet and triplet populations when the MW pulse is on, and n_{s2} and n_{t2} are the singlet and triplet populations when the MW pulse is off. Those solutions consist of double exponential functions as is often found in the literature regarding pulsed experiments [58, 59, 63, 77].

The introduced constants in the above solutions are summarized below,

$$m_{1j} = \frac{C_s + w_{1j} + C_t + w_{2j} - \sqrt{(C_s + w_{1j} - C_t - w_{2j})^2 + 4w_{1j}w_{2j}}}{2}, \tag{2.12}$$

$$m_{2j} = \frac{C_s + w_{1j} + C_t + w_{2j} + \sqrt{(C_s + w_{1j} - C_t - w_{2j})^2 + 4w_{1j}w_{2j}}}{2}, \tag{2.13}$$

$$n^0_{sj} = \frac{w_{2j}G_t + (C_t + w_{2j})\,G_s}{(C_s + w_{1j})\,(C_t + w_{2j}) - w_{1j}w_{2j}}, \tag{2.14}$$

$$n^0_{tj} = \frac{w_{1j}G_s + (C_s + w_{1j})\,G_t}{(C_s + w_{1j})\,(C_t + w_{2j}) - w_{1j}w_{2j}}, \tag{2.15}$$

$$\begin{aligned} w_{11} = \alpha + k_{ISC}(1-\rho),\ w_{21} = \alpha + k_{ISC}\cdot\rho, \\ w_{12} = k_{ISC}(1-\rho),\ w_{22} = k_{ISC}\cdot\rho, \end{aligned} \tag{2.16}$$

where j=1 or 2. It should be noted that the exponents, m_{1j} and m_{2j}, are independent on either the generation rates or the modulation frequency. It can be easily seen that m_{2j} is decided by the fastest rate coefficient, but it is difficult to predict m_{1j}. However, it is clear that m_{2j} is always larger than m_{1j}. Two constant terms, n^0_{sj} and n^0_{tj}, are the steady-state solutions which the system assumes for very low modulation frequency [16, 38, 45, 47, 81]. It should also be noted that the singlet and triplet pair populations will approach values at the end of each half cycle which are at the same time as initial values of the following half cycle. Therefore, the frequency dependence might be able to be explained in terms of the differences between the populations at the end of each half cycle [38, 45], $n_{s1}(T/2) - n_{s2}(T)$ and $n_{t1}(T/2) - n_{t2}(T)$. However, lock-in detected signals are not simply decided by these quantities. The observables are not the population changes, but the changes in the number of photons, which incoprorates both the population change and the recombination probability.

2.1.2 Boundary conditions

Because the spin populations assume the steady state only for a modulation frequency f=0, the time dependent solutions must be solved to explain the transient behavior at arbitrary modulation frequencies. To find the exact solution, the expressions for the eight unknown coefficients A_{ij} and B_{ij} (i, j=1 or 2) in eqs. 2.8, 2.9, 2.10, and 2.11 must be derived by application of eight boundary conditions.

Four of the boundary conditions can be easily found from the periodicity of the solution: $n_{s1}(0) = n_{s2}(T)$, $n_{t1}(0) = n_{t2}(T)$, $n_{s1}\left(\frac{T}{2}\right) = n_{s2}\left(\frac{T}{2}\right)$, and $n_{t1}\left(\frac{T}{2}\right) = n_{t2}\left(\frac{T}{2}\right)$. From these boundary conditions, we obtain

$$A_1 + A_2 + n_{s1}^0 = A_3 e^{(-m_{12}T/2)} + A_4 e^{(-m_{22}T/2)} + n_{s2}^0 \tag{2.17}$$

$$B_1 + B_2 + n_{t1}^0 = B_3 e^{(-m_{12}T/2)} + B_4 e^{(-m_{22}T/2)} + n_{t2}^0 \tag{2.18}$$

$$A_1 e^{(-m_{11}T/2)} + A_2 e^{(-m_{21}T/2)} + n_{s1}^0 = A_3 + A_4 + n_{s2}^0 \tag{2.19}$$

$$B_1 e^{(-m_{11}T/2)} + B_2 e^{(-m_{21}T/2)} + n_{t1}^0 = B_3 + B_4 + n_{t2}^0 \tag{2.20}$$

After each half cycle, the number of each singlet and triplet pair is decreased or increased. These changes depend on the given rate coefficients: the number of singlet or triplet pair is either decreased or increased by spin mixing and increased by pair generation, decreased by the dissociation and recombination processes. From this condition, the other four equations can be found as

$$n_{s1}\left(\frac{T}{2}\right) - n_{s1}(0) = G_s\frac{T}{2} + \int_0^{\frac{T}{2}} \left(w_{21}n_{t1} - (C_s + w_{11})\, n_{s1}\right) dt, \tag{2.21}$$

$$n_{s2}(T) - n_{s2}\left(\frac{T}{2}\right) = G_s\frac{T}{2} + \int_{\frac{T}{2}}^{T} \left(w_{22}n_{t2} - (C_s + w_{12})\, n_{s2}\right) dt \tag{2.22}$$

$$n_{t1}\left(\frac{T}{2}\right) - n_{t1}(0) = G_t\frac{T}{2} + \int_0^{\frac{T}{2}} \left(w_{11}n_{t1} - (C_t + w_{21})\, n_{t1}\right) dt, \tag{2.23}$$

$$n_{t2}(T) - n_{t2}\left(\frac{T}{2}\right) = G_t\frac{T}{2} + \int_{\frac{T}{2}}^{T} \left(w_{12}n_{t2} - (C_t + w_{22})\, n_{t2}\right) dt \tag{2.24}$$

By plugging the eqs. 2.8, 2.10, 2.9, and 2.11 into the above eight equations, we obtain

$$\begin{aligned} &A_1(e^{(-m_{11}T/2)} - 1) + A_2(e^{(-m_{21}T/2)} - 1) \\ &= -\frac{w_{21}B_1 - (C_s + w_{11})A_1}{m_{11}}(e^{(-m_{11}T/2)} - 1) \\ &\quad -\frac{w_{21}B_2 - (C_s + w_{11})A_2}{m_{21}}(e^{(-m_{21}T/2)} - 1) \end{aligned} \tag{2.25}$$

$$\begin{aligned} &A_3(e^{(-m_{12}T/2)} - 1) + A_4(e^{(-m_{22}T/2)} - 1) \\ &= -\frac{w_{22}B_3 - (C_s + w_{11})A_3}{m_{12}}(e^{(-m_{12}T/2)} - 1) \\ &\quad -\frac{w_{22}B_4 - (C_s + w_{12})A_4}{m_{22}}(e^{(-m_{22}T/2)} - 1) \end{aligned} \tag{2.26}$$

$$\begin{aligned} &B_1(e^{(-m_{11}T/2)} - 1) + B_2(e^{(-m_{21}T/2)} - 1) \\ &= -\frac{w_{11}A_1 - (C_t + w_{21})B_1}{m_{11}}(e^{(-m_{11}T/2)} - 1) \\ &\quad -\frac{w_{11}A_2 - (C_t + w_{21})B_2}{m_{21}}(e^{(-m_{21}T/2)} - 1) \end{aligned} \tag{2.27}$$

$$
\begin{aligned}
&B_3(e^{(-m_{12}T/2)}-1)+B_4(e^{(-m_{22}T/2)}-1)\\
=&-\frac{w_{12}A_3-(C_t+w_{22})B_3}{m_{12}}(e^{(-m_{12}T/2)}-1)\\
&-\frac{w_{12}A_4-(C_t+w_{22})B_4}{m_{22}}(e^{(-m_{22}T/2)}-1). \qquad (2.28)
\end{aligned}
$$

Note that the terms $G_s + w_{21}n^0_{t1} - (C_s + w_{11})n^0_{s1} = 0$, $G_s + w_{22}n^0_{t2} - (C_s + w_{12})n^0_{s2} = 0$, $G_t + w_{11}n^0_{s1} - (C_t + w_{21})n^0_{t1} = 0$, $G_t + w_{12}n^0_{s2} - (C_t + w_{22})n^0_{t2} = 0$ are used here, which are obtained from eqs. 2.14 and 2.15.

Solving eq. (2.17)-(2.20), (2.25)-(2.28), and by introducing the parameters $\beta_{ij} = \frac{C_s+w_{1j}-m_{1j}}{w_{2j}}$, $\Delta n^0_s = n^0_{s2} - n^0_{s1}$, $\Delta n^0_t = n^0_{t2} - n^0_{t1}$, and $\gamma_{ij} = e^{-m_{ij}\frac{T}{2}}$, we realized that $B_{ij} = A_{ij}\beta_{ij}$ and four simplified equations

$$
\begin{pmatrix} 1 & 1 & -\gamma_{12} & -\gamma_{22} \\ \beta_{11} & \beta_{21} & -\beta_{12}\gamma_{12} & -\beta_{22}\gamma_{22} \\ \gamma_{11} & \gamma_{21} & -1 & -1 \\ \beta_{11}\gamma_{11} & \beta_{21}\gamma_{21} & -\beta_{12} & -\beta_{22} \end{pmatrix} \begin{pmatrix} A_{11} \\ A_{21} \\ A_{12} \\ A_{22} \end{pmatrix} = \begin{pmatrix} \Delta n^0_s \\ \Delta n^0_t \\ \Delta n^0_s \\ \Delta n^0_t \end{pmatrix}. \qquad (2.29)
$$

are obtained for A_{ij}.

Equation 2.29 is a fully determined system of linear equation, which can be

$$
\begin{aligned}
A_{22} \;=\;& (((\beta_{21}-\beta_{11})\cdot(\Delta n^0_s-\gamma_{11}\Delta n^0_s)-(\Delta n^0_t-\beta_{11}\Delta n^0_s)\cdot(\gamma_{21}-\gamma_{11}))\\
&\cdot((\beta_{21}-\beta_{11})\cdot(\beta_{11}\gamma_{11}\gamma_{12}-\beta_{12})-(\beta_{11}\gamma_{12}-\beta_{12}\gamma_{12})\cdot(\beta_{21}\gamma_{21}-\beta_{11}\gamma_{11}))\\
&-((\beta_{21}-\beta_{11})\cdot(\gamma_{11}\gamma_{12}-1)-(\beta_{11}\gamma_{12}-\beta_{12}\gamma_{12})\cdot(\gamma_{21}-\gamma_{11}))\\
&\cdot((\beta_{21}-\beta_{11})\cdot(\Delta n^0_t-\beta_{11}\gamma_{11}\Delta n^0_s)-(\Delta n^0_t-\beta_{11}\Delta n^0_s)\cdot(\beta_{21}\gamma_{21}-\beta_{11}\gamma_{11})))\\
&/(((\beta_{21}-\beta_{11})\cdot(\gamma_{11}\gamma_{22}-1)-(\beta_{11}\gamma_{22}-\beta_{22}\gamma_{22})\cdot(\gamma_{21}-\gamma_{11}))\\
&\cdot((\beta_{21}-\beta_{11})\cdot(\beta_{11}\gamma_{11}\gamma_{12}-\beta_{12})-(\beta_{11}\gamma_{12}-\beta_{12}\gamma_{12})\cdot(\beta_{21}\gamma_{21}-\beta_{11}\gamma_{11}))\\
&-((\beta_{21}-\beta_{11})\cdot(\gamma_{11}\gamma_{12}-1)-(\beta_{11}\gamma_{12}-\beta_{12}\gamma_{12})\cdot(\gamma_{21}-\gamma_{11}))\\
&\cdot((\beta_{21}-\beta_{11})\cdot(\beta_{11}\gamma_{11}\gamma_{22}-\beta_{22})-(\beta_{11}\gamma_{22}-\beta_{22}\gamma_{22})\cdot(\beta_{21}\gamma_{21}-\beta_{11}\gamma_{11}))), \qquad (2.30)
\end{aligned}
$$

$$
\begin{aligned}
A_{12} \;=\;& ((\beta_{21}-\beta_{11})\cdot(\Delta n^0_s-\gamma_{11}\Delta n^0_s)-(\Delta n^0_t-\beta_{11}\Delta n^0_s)\cdot(\gamma_{21}-\gamma_{11})\\
&-((\beta_{21}-\beta_{11})\cdot(\gamma_{11}\gamma_{22}-1)-(\beta_{11}\gamma_{22}-\beta_{22}\gamma_{22})\cdot(\gamma_{21}-\gamma_{11}))\cdot A_{22})\\
&/((\beta_2-\beta_{11})\cdot(\gamma_{11}\gamma_{12}-1)-(\beta_{11}\gamma_{12}-\beta_{12}\gamma_{12})\cdot(\gamma_{21}-\gamma_{11})), \qquad (2.31)
\end{aligned}
$$

$$
\begin{aligned}
A_{21} \;=\;& ((\Delta n^0_t-\beta_{11}\Delta n^0_s)\cdot(\beta_{21}\gamma_{21}-\beta_{11}\gamma_{11})\\
&-(\beta_{11}\gamma_{12}-\beta_{12}\gamma_{12})\cdot(\beta_{21}\gamma_{21}-\beta_{11}\gamma_{11})\cdot A_{12}\\
&-(\beta_{11}\gamma_{22}-\beta_{22}\gamma_{22})\cdot(\beta_{21}\gamma_{21}-\beta_{11}\gamma_{11})\cdot A_{22})\\
&/((\beta_{21}-\beta_{11})\cdot(\beta_{21}\gamma_{21}-\beta_{11}\gamma_{11})), \qquad (2.32)
\end{aligned}
$$

$$A_{11} = \Delta n_s^0 - A_{21} + \gamma_{12} \cdot A_{12} + \gamma_{22} \cdot A_{22}. \tag{2.33}$$

Equations 2.30, 2.31, 2.32, 2.33 represent exact and general analytical solutions for the singlet and triplet density functions during a cwODMR modulation cycle. We are thus in a position to determine the temporal evolution of the cwODMR observable.

2.2 Transient behavior of cwODMR

The observable in cwODMR is the emission rate of photons, and, as described in eq. 2.6, the time dependence can be obtained by adding the contribution from the singlet and triplet pair populations multiplied by the singlet and triplet recombination rate coefficients, respectively

$$I_1 = (r_s A_{11} + r_t B_{11})\, e^{-m_{11} t} + (r_s A_{21} + r_t B_{21})\, e^{-m_{21} t} + r_s n_{s1}^0 + r_t n_{t1}^0, \tag{2.34}$$

$$I_2 = (r_s A_{12} + r_t B_{12})\, e^{-m_{12}\left(t - \frac{T}{2}\right)} + (r_s A_{22} + r_t B_{22})\, e^{-m_{22}\left(t - \frac{T}{2}\right)} + r_s n_{s2}^0 + r_t n_{t2}^0. \tag{2.35}$$

Here, I_1 and I_2 are the photon emission rate due to recombination of both singlet and triplet pairs when the pulse is on and off, respectively. The dash-dotted curve in Fig. 2.3 is a numerical example of the time dependence. Because m_{1j} and m_{2j} are always positive and $m_{2j} > m_{1j}$, the first and second terms in both eq. 2.34 and eq. 2.35 determine the faster and slower decay, respectively. It is difficult to predict which response will show an enhancement or quenching behavior because the overall response depends not only on m_{1j} and m_{2j} but also on $r_s A_{ij} + r_t B_{ij}$. Since the coefficients of all exponential terms have very complicated dependencies on a variety of parameters (see eqs. 2.30, 2.31, 2.32, and 2.33), it is clear that sign predictions depend on the magnitudes of many parameters at the same time. Using the above solution, we have been able to reproduce a wide variety of cwODMR transients reported in the literature [4, 9, 11, 12, 19].

2.3 Modulation frequency dependence

The time dependence solutions, eqs. 2.34 and 2.35, are the collective responses to the modulated B_1 field over all frequency ranges. However, in experimental implementations which utilize a lock-in technique, only the component of the transient signal which has the same frequency as the reference will be obtained. With lock-in quadrature detection, both the in- an out-of-phase components are available. While the out-of-phase components have often been ignored in the literature [20, 29, 37, 40, 46], we note that the out-of-phase components contain important information.

To find the in-phase and out-of-phase components at the given modulation frequency, it is better to find the Fourier series of eqs. 2.34 and 2.35, and the frequency responses will be decided from the Fourier coefficients according to the definition of the Fourier series as below,

$$I_{Fs}(t) = \frac{I_0}{2} + \sum_{l=1}^{\infty}\left(I_c \cos\left(\frac{2l\pi}{T}t\right) + I_s \sin\left(\frac{2l\pi}{T}t\right)\right), \tag{2.36}$$

$$I_c = \frac{2}{T}\int_0^T I(t)\cos\left(\frac{2l\pi}{T}t\right)dt, \tag{2.37}$$

$$I_s = \frac{2}{T}\int_0^T I(t)\sin\left(\frac{2l\pi}{T}t\right)dt. \tag{2.38}$$

Then the obtained two coefficients as well as the zero frequency component are:

$$\begin{aligned} I_c &= \frac{2m_{11}}{T}(r_s A_{11} + r_t B_{11})\left(\frac{1 - e^{-m_{11}T/2}\cos(l\pi)}{{m_{11}}^2 + 4l^2\pi^2/T^2}\right) \\ &+ \frac{2m_{21}}{T}(r_s A_{21} + r_t B_{21})\left(\frac{1 - e^{-m_{21}T/2}\cos(l\pi)}{{m_{21}}^2 + 4l^2\pi^2/T^2}\right) \\ &+ \frac{2m_{12}}{T}(r_s A_{12} + r_t B_{12})\left(\frac{\cos(l\pi) - e^{-m_{12}T/2}}{{m_{12}}^2 + 4l^2\pi^2/T^2}\right) \\ &+ \frac{2m_{22}}{T}(r_s A_{22} + r_t B_{22})\left(\frac{\cos(l\pi) - e^{-m_{22}T/2}}{{m_{22}}^2 + 4l^2\pi^2/T^2}\right), \end{aligned} \tag{2.39}$$

$$\begin{aligned} I_s &= \frac{4l\pi}{T^2}(r_s A_{11} + r_t B_{11})\left(\frac{1 - e^{-m_{11}T/2}\cos(l\pi)}{{m_{11}}^2 + 4l^2\pi^2/T^2}\right) \\ &+ \frac{4l\pi}{T^2}(r_s A_{21} + r_t B_{21})\left(\frac{1 - e^{-m_{21}T/2}\cos(l\pi)}{{m_{21}}^2 + 4l^2\pi^2/T^2}\right) \\ &+ \frac{4l\pi}{T^2}(r_s A_{12} + r_t B_{12})\left(\frac{\cos(l\pi) - e^{-m_{12}T/2}}{{m_{12}}^2 + 4l^2\pi^2/T^2}\right) \\ &+ \frac{4l\pi}{T^2}(r_s A_{22} + r_t B_{22})\left(\frac{\cos(l\pi) - e^{-m_{22}^2T/2}}{{m_{22}}^2 + 4l^2\pi^2/T^2}\right) \\ &+ \left(r_s\Delta n_s^0 + r_t\Delta n_t^0\right)\left(\frac{\cos(l\pi) - 1}{l\pi}\right), \end{aligned} \tag{2.40}$$

$$\begin{aligned} I_0 &= \frac{2}{T}(r_s A_{11} + r_t B_{11})\left(\frac{1 - e^{-m_{11}T/2}}{m_{11}}\right) + \frac{2}{T}(r_s A_{21} + r_t B_{21})\left(\frac{1 - e^{-m_{21}T/2}}{m_{21}}\right) \\ &+ \frac{2}{T}(r_s A_{12} + r_t B_{12})\left(\frac{1 - e^{-m_{12}T/2}}{m_{12}}\right) + \frac{2}{T}(r_s A_{22} + r_t B_{22})\left(\frac{1 - e^{-m_{22}T/2}}{m_{22}}\right) \\ &+ r_s(n_{s1}^0 + n_{s2}^0) + r_t(n_{t1}^0 + n_{t2}^0). \end{aligned} \tag{2.41}$$

The Fourier series in eq. 2.36 can be simplified by introducing $V_0 = \sqrt{{I_c}^2 + {I_s}^2}$ and $\varphi = \tan^{-1}\left(\frac{I_c}{I_s}\right)$ as below,

$$I_{Fs}(t) = \frac{I_0}{2} + \sum_{l=1}^{\infty} V_0 \sin(2l\pi f t + \varphi), \tag{2.42}$$

where f is the frequency of the square modulation, 1/T. A Lock-in amplifier multiplies the input signal by its own internal reference signals, $\sin(\omega_L t + \theta_L)$ and $\cos(\omega_L t + \theta_L)$, to detect in-phase and out-of-phase signals, respectively. At this moment, the in-phase V_{in} and out-of-phase V_{out} signals are

$$\begin{aligned} V_{in} &= \frac{I_0}{2} V_L \sin(\omega_L t + \theta_L) \\ &\quad + \sum_{l=1}^{\infty} \frac{V_L V_0}{2} \left(\cos\left((2l\pi f - \omega_L)t + \varphi - \theta_L\right) - \cos\left((2l\pi f + \omega_L)t + \varphi + \theta_L\right)\right) \end{aligned} \tag{2.43}$$

$$\begin{aligned} V_{out} &= \frac{I_0}{2} V_L \sin(\omega_L t + \theta_L) \\ &\quad + \sum_{l=1}^{\infty} \frac{V_L V_0}{2} \left(\sin\left((2l\pi f + \omega_L)t + \varphi + \theta_L\right) + \sin\left((2l\pi f - \omega_L)t + \varphi - \theta_L\right)\right) \end{aligned} \tag{2.44}$$

where V_L is the amplitude of the reference signals. After these signals pass through a low pass filter, only the nonAC signals will remain. And the frequency of the internal reference signal is fixed such that it has a phase which is the same as the phase of the external reference signal. Thanks to this condition, $\omega_L \approx 2\pi f$, and the in-phase and out-of-phase signals become

$$V_{in} = \frac{V_{01}}{2} \cos(\varphi_1) = \frac{1}{2} I_{s1}, \tag{2.45}$$

$$V_{out} = \frac{V_{01}}{2} \sin(\varphi_1) = \frac{1}{2} I_{c1} \tag{2.46}$$

where $V_{01} = V_0$, $I_{s1} = I_s$, $I_{c1} = I_c$, and $\varphi_1 = \varphi$ at $l = 1$, and, θ_L is usually set to zero.

Thus the in-phase and out-of-phase cwODMR signals are the Fourier coefficients of the lowest frequency sine and cosine terms of the Fourier series solution (eq. 2.36), respectively. Examples are shown in Fig. 2.3 to explain the decomposed in-phase and out-of-phase components of the time response. It should be noted that the cwEDMR solutions also can be obtained in a similar way by replacing r_s and r_t in front of the exponential functions in eqs. 2.34 and 2.35 with d_s and d_t, respectively, as shown in eq. 2.7.

Similarly the solutions for B_0 field modulated cwODMR and cwEDMR can be found in the same way as for microwave modulated cwODMR and cwEDMR. While the difference

between these two modulation techniques is that the spin resonance is modulated by a square function and a harmonic function, the lock-in detected observables are identical since the lock-in technique is sensitive to the lowest harmonic component in either case.

2.3.1 At low modulation frequency

We use the low modulation frequency limit to check the solution of our model, by varifying that these solutions can explain the cwODMR response. From the solutions above, the low frequency behavior is seen to be

$$\begin{aligned} V_{in,lf} &= \frac{(r_s+r_t)(G_t+G_s)\alpha+(r_tr_s+r_sw_{22}+r_tw_{12})(G_t+G_s)+r_td_sG_t+r_sd_tG_s}{(C_s+C_t)\alpha+(C_s+w_{12})(C_t+w_{22})-w_{12}w_{22}}\cdot\frac{2}{\pi} \\ &\quad -\frac{(r_tr_s+r_sw_{22}+r_tw_{12})(G_t+G_s)+r_td_sG_t+r_sd_tG_s}{(C_s+w_{12})(C_t+w_{22})-w_{12}w_{22}}\cdot\frac{2}{\pi}, \end{aligned} \tag{2.47}$$

$$V_{out,lf}=0. \tag{2.48}$$

The out-of-phase component vanishes since the transient response can easily follow the slow modulation. The in-phase component shows a typical microwave power dependence: it vanishes at small power (when $\alpha \to 0$) and it becomes saturated at high power (i.e., it has a nonzero constant value). MW power dependence of eqs. 2.47 and 2.48 will be explained in the section 2.4.

2.3.2 Ambiguity of cwODMR measurements

To understand the modulation frequency dependence of cwODMR, we inspected a large number of quantitative models. There is an extremely large number of possible qualitative and quantitative relationships betwen the model parameters. To limit the number of cases that we inspected, we chose a number of relationships between these parameters. We considered that i) the triplet recombination coefficient is the smallest one among all the recombination and dissociation rate coefficients ($r_t < r_s,\ d_s,\ d_t$) (unless otherwise noted), and ii) the singlet dissociation rate coefficient is smaller than the triplet dissociation rate coefficient ($d_s < d_t$) which means that the singlet intermediate state is assumed to be energetically lower than the triplet intermediate state (unless otherwise noted). Under these assumptions, a large number of quantitative models were investigated by varying r_t, r_s, d_s, d_t, k_{ISC}, and α in the range from 10^{-4} to $10^{9}\ s^{-1}$. We investigated almost a thousand different variations of the relationship between different parameters.

After looking through these cases, we find that it is almost impossible to distinguish some of the quantitative models based on their modulation frequency behaviors. Fig. 2.4 illustrates this ambiguity. Figure 2.4 (a), (b), and (c) show nearly identical frequency

dependencies of three very different quantitative models. The frequencies at which the in-phase signals have their maximum slope and the out-of-phase signals show their local maximum values are almost identical, and their shapes are also indistinguishable. The patterns shown in Fig. 2.4 represent in fact the most common frequency dependency that we have found out by the tested quantitative models. This illustrates the difficulty in extracting correct values for the corresponding coefficients from a simple frequency dependence - one can find a wide range of values which can reproduce it. This ambiguity is the most serious disadvantage of using the cwODMR or cwEDMR frequency dependence to determine the rate of underlying physical processes and the realization of their ambiguity puts many interpretations of cwODMR data reported in the literature in questions.

Of the nearly thousand models we tested, we were able to describe them all with only four different frequency dependency patterns. These are shown in Fig. 2.5. We find that those patterns are determined mostly by the recombination rate coefficients, the microwave power, the spin mixing rates, as well as the generation rates. How each parameter influences the frequency dependence will be discussed in the following sections. The most trivial cases, seen in Fig. 2.5 (a) and (c), will be discussed first.

2.3.3 Trivial case (small spin mixing rates)

To understand the behavior of the response to the modulation frequency, the trivial patterns will be discussed. "Trivial" means that the spin mixing rates, both k_{ISC} and α are negligible when compared to all the other rates. In this case, only the spin pair annihilation processes determined by the recombination and dissociation rate coefficients become dominant. All the patterns in Fig. 2.4 as well as the patterns in Fig. 2.5 (a) and (c) are obtained under the assumption of insignificant spin mixing rates, k_{ISC} and α. The pattern in Fig. 2.5 (c) is identical to the one in (a), but inverted due to different ratios between G_s and G_t. We found that the sign of the lock-in detected signal depends on almost all transition processes as one can deduce from Table 2.1.

The most often seen patterns in Fig. 2.5 (a) and (c) are easily described qualitatively: at low frequencies, the in-phase signal has a constant nonzero value with no out-of-phase component. This is because approach to the steady-state takes place on a time scale much faster than the modulation period, and the recorded transient response looks like the applied microwave pulse train shown in Fig. 2.6 (a). These in-phase and out-of-phase responses are not seriously changed until the modulation frequency approach the slowest time constant, m_{1j}^{-1}, and this can be confirmed by the low-frequency responses in Fig. 2.4. For all cases in Fig. 2.4 and in Fig. 2.6, m_{1j} and m_{2j} are in the ranges of $10^2 \sim 10^4$ and

$10^4 \sim 10^6$, respectively. As the modulation frequency approaches m_{1j}, the system begins to lag behind the applied MW modulation, and the overall response ceases to resemble the simple harmonic function. This results in a decrease of the in-phase signal and an increase of the out-of-phase signal as seen in Fig. 2.6 (b). At very high frequencies, much faster than than the fastest time constant, $m_{2j}^{-1} \sim 10^{-6}$, both the in- and out-of-phase components tend to approach zero. This behavior is explained by the exponential decay functions which become linear with small arguments and thus, they become constants (no change) when $T \to 0$ [14, 48].

2.3.4 Recombination, dissociation, and flip-flop

Because cwODMR measures emission rates of photons, which are usually determined by the dominant singlet recombination rate $r_s n_s$, one might expect that r_s should have a dominant role in determining the frequency dependence pattern. In general, this is not the case though: other rate coefficients, especially spin mixing rates, can be most significant for the behavior of an cwODMR signal. Fig. 2.7 shows one of the most frequently observed examples of the frequency dependence patterns influenced by both r_s and α.

When α is small, an increasing r_s changes little in the observed frequency dependence (Fig. 2.7 (a) and (b)). The most significant effect is a shift of the frequencies where both the in-phase and the out-of-phase components show their maximum rate changes. This is due to the the increase of the time constants, m_{ij}^{-1}, from $m_{1j} \sim 10^4$ and $m_{2j} \sim 10^6$ to $m_{1j} \sim 10^6$ and $m_{2j} \sim 10^7$, due to very fast r_s. It should be noted that d_t is 10^6 in all examples in Fig. 2.7 and r_s is 10^7 in Fig. 2.7 (b) and (d). The frequency dependence also shows little change when r_s remains small and α is increased (Fig. 2.7 (c)). This corresponds to Fig. 2.5. However, when α becomes fast enough to compete with the slower time constant, m_{1j}^{-1}, or even faster than m_{2j}^{-1}, and r_s becomes faster than any dissociation rate coefficients, a more complicated frequency dependence emerges. The in-phase signal does not show the simple behavior as it has a local extremum. The out-of-phase signal does not only show the local extremum (as in the simple pattern) but also a zero-crossing point, due to a sign change (Fig. 2.7 (d)). This pattern corresponds to Fig. 2.5 (b) and (d). It should be noted that the intersystem-crossing rate, k_{ISC}, has been assumed to be small to investigate the influence of α, and this pattern also appears when k_{ISC} becomes large with a small α. This aspect will be explained further in the following section. Note that for cwODMR experiments this pattern appears only when r_s becomes faster than any dissociation rate coefficient and α or k_{ISC} is fast too. It can also be seen only for cwEDMR experiment when the dissociation rate coefficients and α or k_{ISC} are fast (not shown here). We can thus infer that the effect

of dissociation in cwEDMR is very similar to that of recombination in cwODMR.

2.3.5 The influence of intersystem-crossing on cwODMR experiments

Because the intersystem-crossing rate, k_{ISC}, also represents a spin mixing processes, it acts in a similar way as α even though k_{ISC} is always on, in contrast to α which turns on and off periodically. To investigate the influence of k_{ISC}, α is assumed to be small in this section.

When k_{ISC} is slow, very little change of the frequency dependence as a function of r_s is seen, similar to the behavior described in the previous section. In contrast to the case of a large α and small r_s, a major change in the frequency dependence pattern can be seen at fast k_{ISC} and slow r_s (Fig. 2.8 (c)). A second local extremum appears in the out-of-phase component and a small bump at high frequency in the in-phase component. When both k_{ISC} and r_s increase enough to compete with each other, a new pattern appears (Fig. 2.8 (d)). Note that this pattern is similar to Fig. 2.7 (d). But they become similar to the pattern in Fig. 2.5 (e) and (f) when $V_{in,lf} \to 0$ at small α (eq. (2.47)).

2.3.6 Pair generation

Due to spin-selection rules, optically generated electron-hole pairs are formed in singlet states and remain in this configuration unless strong spin-orbit coupling is present [82]. Thus, we can assume $G_s \gg G_t$. Figure 2.5 (a) corresponds to this case in which the in-phase and the out-of-phase components are always negative and positive, respectively. This case represents the frequency dependence of photoluminescence detected ODMR (PLDMR). Used parameters are $r_s = 10^6$, $r_t = 10^{-2}$, $d_s = 10^2$, $d_t = 10^4$, $k_{ISC} = 1$, $\alpha = 10^{-3}$, $\rho = 0.75$, $G_s = 10^{24}$, $G_t = 10^{20}$. In contrast to optical generation, spin configuration of electron-hole pairs formed electrically, i.e., via electrical injection, is determined by spin statistics and we can assume $3G_s \approx G_t$. All parameters in Fig. 2.5 (a) and (c) are the same except that $3G_s = G_t = 10^{20}$ in Fig. 2.5 (c). We can see from these calculations that electroluminescence detected ODMR (also called ELDMR) can show the opposite sign compared to PLDMR, for very similar underlying physical processes. It should be noted that this inversion could be found only for certain parameter sets, and this inversion can also happen when $3G_s \neq G_t$ but $G_s > G_t$. For example, the sign of the in-phase component also becomes positive (not shown here) if every parameter remains the same except for $G_s = 10 \times G_t$. Thus, cwODMR can result in a positive in-phase and negative out-of phase signal even though G_t can be orders of magnitude but not many orders of magnitude smaller than G_s. This is because

the sign inversion is also determined by rate coefficients and not just the generation rates. These cases will be discussed in Section 2.6.

2.4 Power dependence

The spin flip rate coefficient, α, is proportional to the applied microwave power [71]. Thus we can calculate the power dependence of cwODMR signals. Examples are shown in Fig. 2.9. For low modulation frequencies, (see Fig. 2.9 (a)), a simple saturation behavior is predicted by eqs. 2.47 and 2.48. Note that the out-of-phase is not always zero, but approaches zero at low frequencies, as expected from eq. 2.48. The saturation characteristics become more complicated as the modulation frequency increases. At 10^4 Hz, the in-phase component shows a local extremum before it returns to a saturation value (Fig. 2.9 (b)). Similar behavior has been reported recently for low magnetic field cwEDMR on crystalline silicon interface defects [16]. At high modulation frequency, the in-phase component shows the usual saturation behavior (even though its saturation occurs at much higher power) but the out-of-phase component shows a local extremum before it approaches a saturation value. It also has a different sign than at lower frequencies (Fig. 2.9 (c)). This shows that one can find opposite signs of in-phase and out-of-phase signals at high MW power and high MW modulation frequencies.

2.5 Signal sign dependencies on the modulation frequency

Sign changes of cwEDMR and cwODMR signal have been found in InP nanoparticles [19] and organic semiconductors [38, 45]. The sign change of cwODMR response in organic semiconductor has been attributed to the imbalance between changes in the numbers of singlet and triplet pairs when the pulse is on and off, which are equivalent to $n_{s1}(T/2) - n_{s2}(T)$ and $n_{t1}(T/2) - n_{t2}(T)$ in our model. The zero-crossing point of the modulation frequency dependence function has also been used to estimate the intersystem-crossing time [38, 45]. According to those reports, the zero-crossing can appear at a certain frequency where the increase in the number of singlet pairs is matched with the decrease of the number of triplet pairs so that the change in the total number of pairs is zero. However, we show here that the zero-crossing can be due to not only the imbalance of changes between singlet and triplet pairs but also to other more complicated relationships betwen physical parameters.

As can be seen in the solutions of the rate equations given above, the frequency dependence is not simply obtained from $n_{s1}(T/2) - n_{s2}(T)$ and $n_{t1}(T/2) - n_{t2}(T)$, but has a complicated dependence on various parameters. Among the quantitative models tested

here , zero-crossing behavior is rarely seen. Fig. 2.10 shows one example: no zero-crossing is observed for small r_t, but when r_t becomes larger and very close to r_s, zero-crossing is observed (Fig. 2.10 (a), (b)). It should be noted that the origin of this zero-crossing is not obvious because of the complexity of the solutions, although we note that $n_{s1}(T/2) - n_{s2}(T)$ and $n_{t1}(T/2) - n_{t2}(T)$ do not meet each other at the zero-crossing point in this case, in contrast to the model described elsewhere [38, 45]. Thus the imbalance between changes in n_s and n_t cannot be the reason for the observed zero-crossing. We note that zero-crossing also can appear due to an overlap of two different spin-dependent recombination mechanisms whose signs are opposite (e.g., in cwODMR of a radiative and a nonradiative channel). Note however that all zero-crossing effects demonstrated here are obtained from a single recombination process. The existence of zero-crossing indicates that one can observe different signs of cwODMR and cwEDMR signals from the identical sample at different modulation frequencies.

2.6 The interpretation of cwEDMR and cwODMR signal signs

The signs of the cwEDMR and cwODMR signals have long been considered important indicators for the natures of electronic transitions. For example, it has been generally accepted that radiative recombination results in positive ODMR in-phase signal [5, 7, 17]. However, the recent observations of sign changes [19, 38, 45] at certain frequencies suggest that signs may depend on complicated processes and the interpretation based soley on the sign of a modulated cwODMR or cwEDMR signal is not possible.

CwEDMR and cwODMR signal signs are determined by the transient responses of optical or electrical observables to a repeated change between on- and off-resonance, as described in Section 2.3. Because the time constants and prefactors of the double exponential functions in eq. (2.8), (2.9), (2.10), and (2.11) are functions of all the transition rate coefficients, there are many scenarios which can produce quenching and enhancement signals for both radiative and nonradiative ODMR signals as well as for EDMR signals. Many transitions are competing with each other. For instance, recombination as well as dissociation are pair annihilation processes but only recombination causes PL while dissociation does not. Thus when a radiative recombination process is slow but dissociation is faster the resonant response may lead to quenching. This example shows that the following qualitative description of the sign of cwODMR signals is important.

The study of the cwODMR signal the sign change as functions of all individual parameters is beyond the scope of this work. Instead, only the low modulation frequency behavior

will be discussed. This is a reasonable restriction because the sign does not change as long as there is no zero crossing.

The solution for the in-phase cwODMR signal at low modulation frequency is given in eq. (2.47). A quantitative analysis has been done by calculating $V_{in,lf}$ while changing some parameters, for an example shown in Fig. 2.11 for which it is assumed that both singlet and triplet dissociation probabilities are not distinguishable, two mixing rate coefficients, k_{ISC} and α, are slower than any other recombination and dissociation, and total generation rate, $G_s + G_t$ is fixed to 10^{16}, r_t to 1, and ρ to 0.75. Fig. 2.11 (a) shows the zero frequency in-phase cwODMR signal, $V_{in,lf}$, as a function of the relative ratio of the triplet generation rate to the singlet generation rate, G_t/G_s, and the ratio of the dissociation rate coefficient to the singlet recombination rate coefficient which is fixed to $r_s = 10^4$. Color reflects the normalized intensity of $V_{in,lf}$. It should be noted that positive and negative values are intentionally placed in different scales to make them clearly distinguishable. One can find two noticeable features. (i) The intensity tends to increase as G_t/G_s becomes larger and becomes negative at low G_t as in Fig. 2.11 (b). (ii) The intensity also depends on the dissociation rate coefficients: when d is larger or smaller than the singlet recombination rate coefficient r_s, $V_{in,lf}$ becomes very small, and shows an extremum and sign change. Fig. 2.11 (a), (b), and (c) show that the signs are positive at high triplet generation rates and low dissociation rates or, equivalently, high recombination rates. When dissociation is not fast, signs are positive as long as triplet generation is not too much slower than singlet generation rate. This means that changing the pair generation method between optical and electrical methods can induce a sign change in cwODMR. This behavior can be more easily understood by means of competing singlet and triplet pairs. In Fig. 2.11 (d) and (e), the differences $n^0_{s1} - n^0_{s2}$ and $n^0_{t1} - n^0_{t2}$, are calculated and plotted as the same parameters as (a). Note that the low-frequency solution for the in-phase cwODMR signal, $V_{in,lf}$, is proportional to $r_t(n^0_{s1} - n^0_{s2}) + r_s(n^0_{t1} - n^0_{t2})$. Both plots show different behavior compared to $V_{in,lf}$ but the boundaries dividing positive and negative values are very similar. When the pair annihilation is dominated only by singlet recombination process, one can infer that the number of singlet pairs quickly decreases in the steady-state offresonance condition. Thus, the steady-state is dominated by triplet pairs. Consequently a resonant MW converts triplet pairs to singlet pairs, it increases the number of singlet pairs which results in an enhancement of cwODMR signal.

This qualitative pictures applies to the region where $n^0_{s1} - n^0_{s2}$ is positive and $n^0_{t1} - n^0_{T2}$ is negative, in the upper left regions in Fig. 2.11 (a), (d), and (e) for example. In contrast, if

the triplet generation is too low ($G_t < \frac{r_t+d_t}{r_s+d_s}G_s$), (lower-left corners in Fig. 2.11 (a), (d), and (e)), only a small number of triplet pairs forms during the off resonance steady-state, and the steady-state at offresonance is dominated by singlet pairs. In this case spin resonance induced changes to the number of singlet pairs can become negative.

The statements above are based on the assumption of low k_{ISC} and α. When k_{ISC} becomes larger than the other rates, patterns of $V_{in,lf}$ (not shown here) similar to the pattern in Fig. 2.11 are found, but the slight shifts of boundaries dividing positive and negative can exist as well. Similar shifts have been found at different ρ. Consequently, cwODMR and cwEDMR signs also depend on intersystem-crossing rate k_{ISC} and the temperature (Note that ρ is a function of temperature). We could not identify a shift of boundaries due to a change of α but this does not exclude the possible case that α can also cause sign changes. We note again that sign changes can also occur at a certain modulation frequency as already explained above.

Therefore, we conclude that dissociation, recombination, relative ratio between singlet and triplet generation, intersystem-crossing, temperature, and modulation frequency are the factors which all can change the sign of cwODMR signals.

Finally, we want to address the question of whether radiative and nonradiative recombination results in opposite cwODMR signal signs. We have checked a number of quantitative models and two examples are shown in Fig. 2.12. In contrast to all other cases discussed above, the nonradiative singlet recombination coefficients, $r_{s,nr}$ is taken into account. In Fig. 2.12 (a) and (c), $r_{s,nr}$ is assumed to be smaller than r_s to simulate the modulation frequency dependence in which radiative recombination is dominant. In Fig. 2.12 (b) and (d), $r_{s,nr}$ is assumed to be the larger than r_s to investigate the nonradiative process. It should be mentioned again that $r_{s,nr}$ contributes to the pair annihilation process but it does not contribute to the radiative emission rate term as explained in Section 2.1.1. Note that Fig. 2.12 (a) shows one of the modulation frequency dependence patterns that are discussed above. The in-phase signal is negative even though r_s is most dominant because $G_s \gg G_t$.

Fig. 2.12 (b) shows a zero-crossing behavior. Thus, the in-phase component can be positive and negative even though $r_{s,nr}$ is dominant. In contrast to the cwODMR cases, the signs of the cwEDMR in-phase signals are positive in both cases as shown in (c) and (d). To summarize, our results show that cwODMR signals can be negative and positive for both, radiative and nonradiative recombination processes. Any conclusion about the nature of a spin-dependent recombination process from the sign of an observed cwODMR signal is therefore prohibitive.

2.7 Summary and conclusion

A set of rate equations based on an intermediate pair recombination model are presented and generalized analytical solutions have been obtained. These solutions have been used to calculate modulation frequency dependencies of cwEDMR and cwODMR signals. It has then been investigated how experimental parameters affect these modulation frequency dependencies which revealed that a large number of quantitatively different models show nondistinguishable modulation frequency dependence patterns. This implies that the interpretation of cwODMR and cwEDMR experiments can be very ambiguous. It is further shown that signs of cwODMR and cwEDMR signals depend on most rate coefficients as well as experimental parameters such as temperature and modulation frequency. Thus, there are many variables which can reverse the sign of cwEDMR and cwODMR signals and consequently, conclusions about the radiative or nonradiative nature of an observed spin–dependent transition solely based on the sign of an observed spin–dependent process or its modulation frequency dependence is not possible.

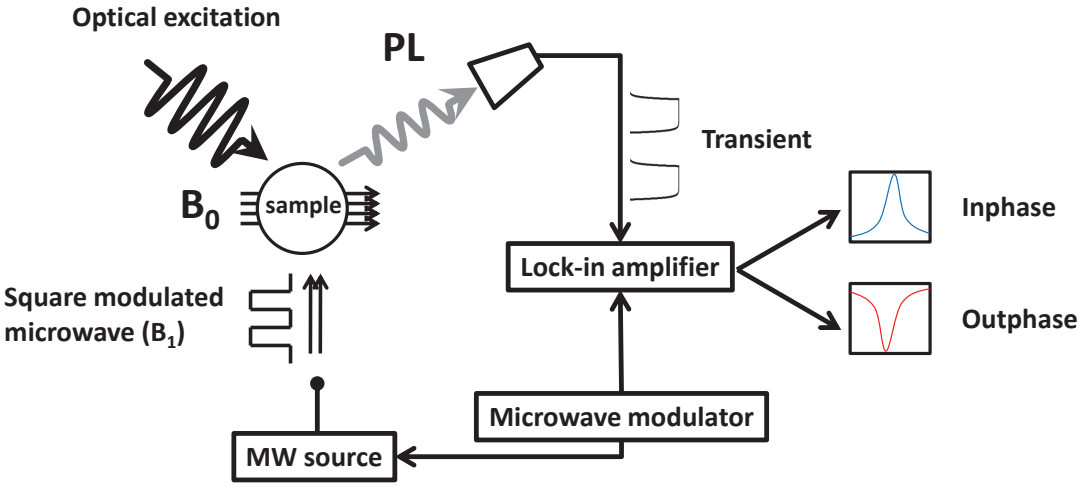

Figure 2.1. Sketch of a setup of cwODMR. The basic principle of cwODMR is the same as that of conventional ESR. Square microwave modulation can be used instead of continuous B_0 field modulation and a lock-in amplifier is employed to increase the signal-to-noise ratio.

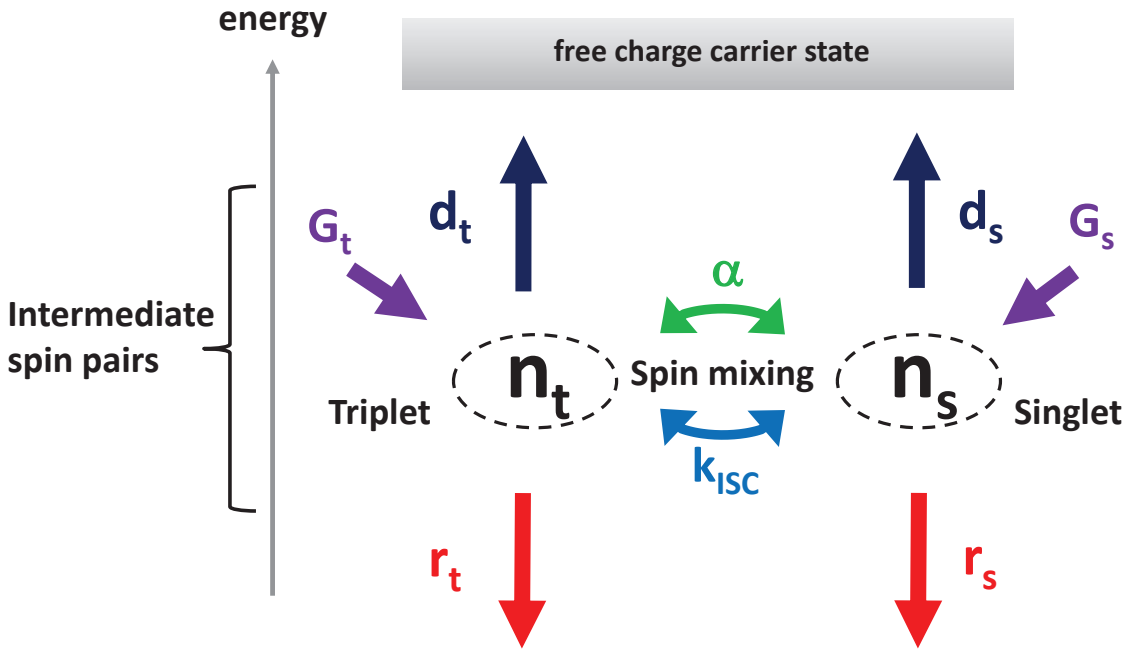

Figure 2.2. The intermediate pair recombination model (KSM) as relevant for cwODMR and cwEDMR. Triplet and singlet pairs are formed with two constant generation rates G_t and G_s, respectively. Those pairs can dissociate into free charge carrier states with certain probabilities d_t and d_s (dissociation rates) or can recombine to excitonic state with recombination rates r_t and r_s. A spin mixing process can be introduced by ESR externally and this rate is described by α. Another spin mixing process, intersystem-crossing process is described by k_{ISC}. Note that n_t and n_s represent triplet and singlet pair densities, respectively. They do no necessarily correspond to eigenstate densities.

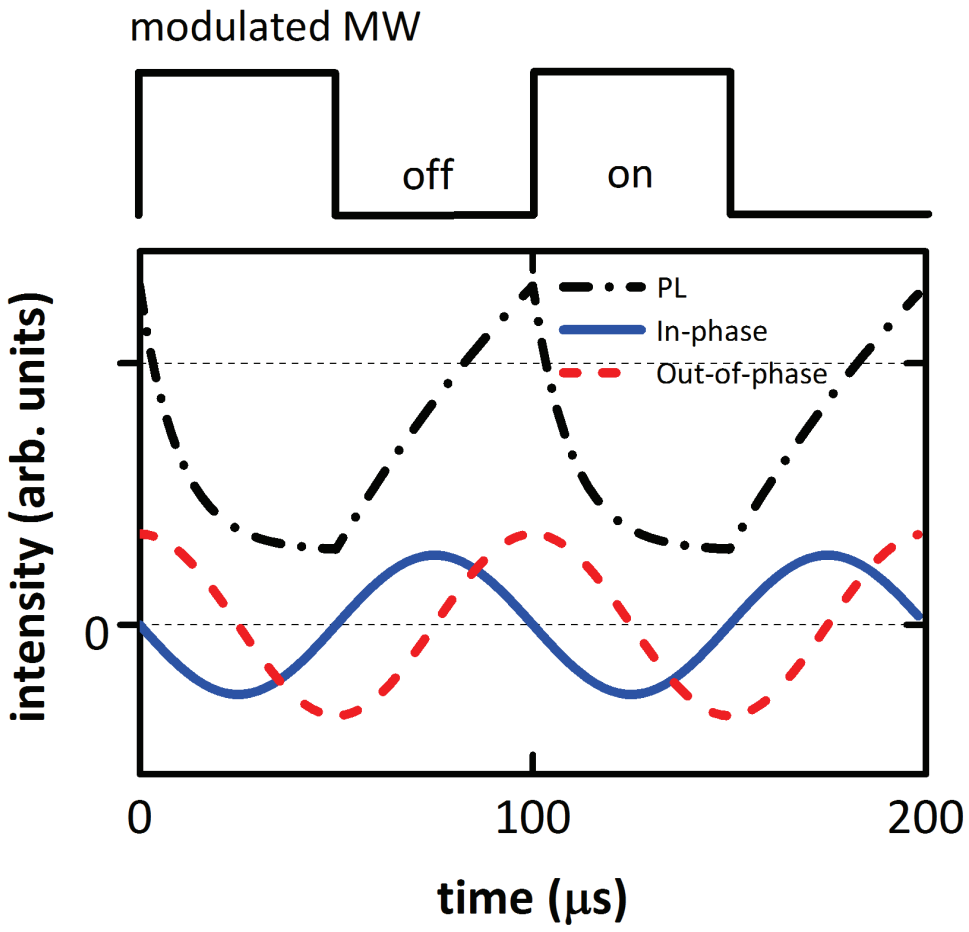

Figure 2.3. A time transient calculated from a numerical model described by a combination of parameters as $r_s = 10^4$, $r_t = 10^0$, $d_s = 10^2$, $d_t = 10^6$, $k_{ISC} = 10^{-2}$, $\alpha = 10^5$, $\rho = 0.75$, $G_s = 10^{23}$, and $G_t = 10^{20}$. The dash-dotted curve shows the overall response obtained from eqs. 2.34 and 2.35. The blue solid and red dashed curves are the in-phase and the out-of-phase components described by $I_{s1}\sin(\frac{2\pi}{T}t)$ and $I_{c1}\cos(\frac{2\pi}{T}t)$, respectively. See detail in text.

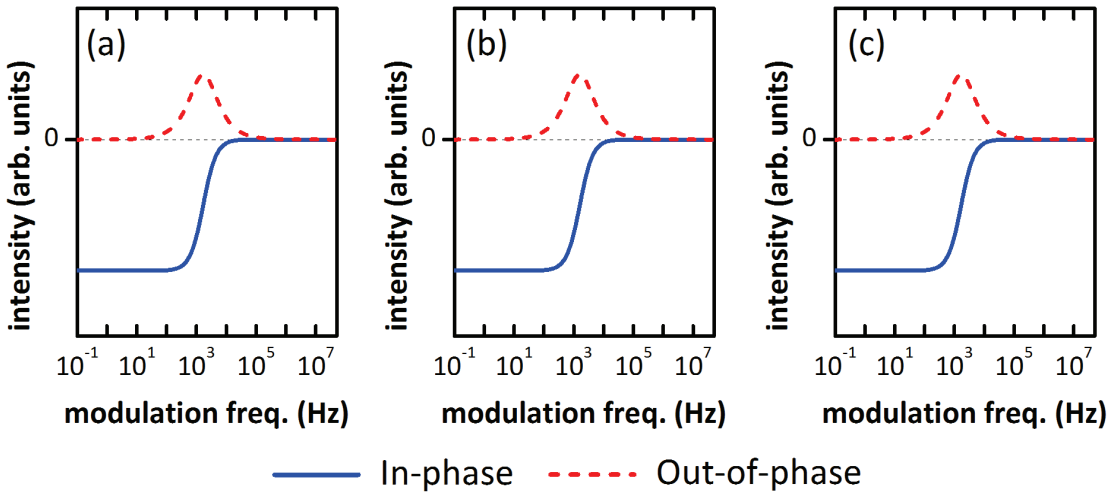

Figure 2.4. Three different quantitative models result in indistinguishable frequency dependencies. Each quantitative model is determined by a different set of parameters. Refer to Table 2.1 for all used values.

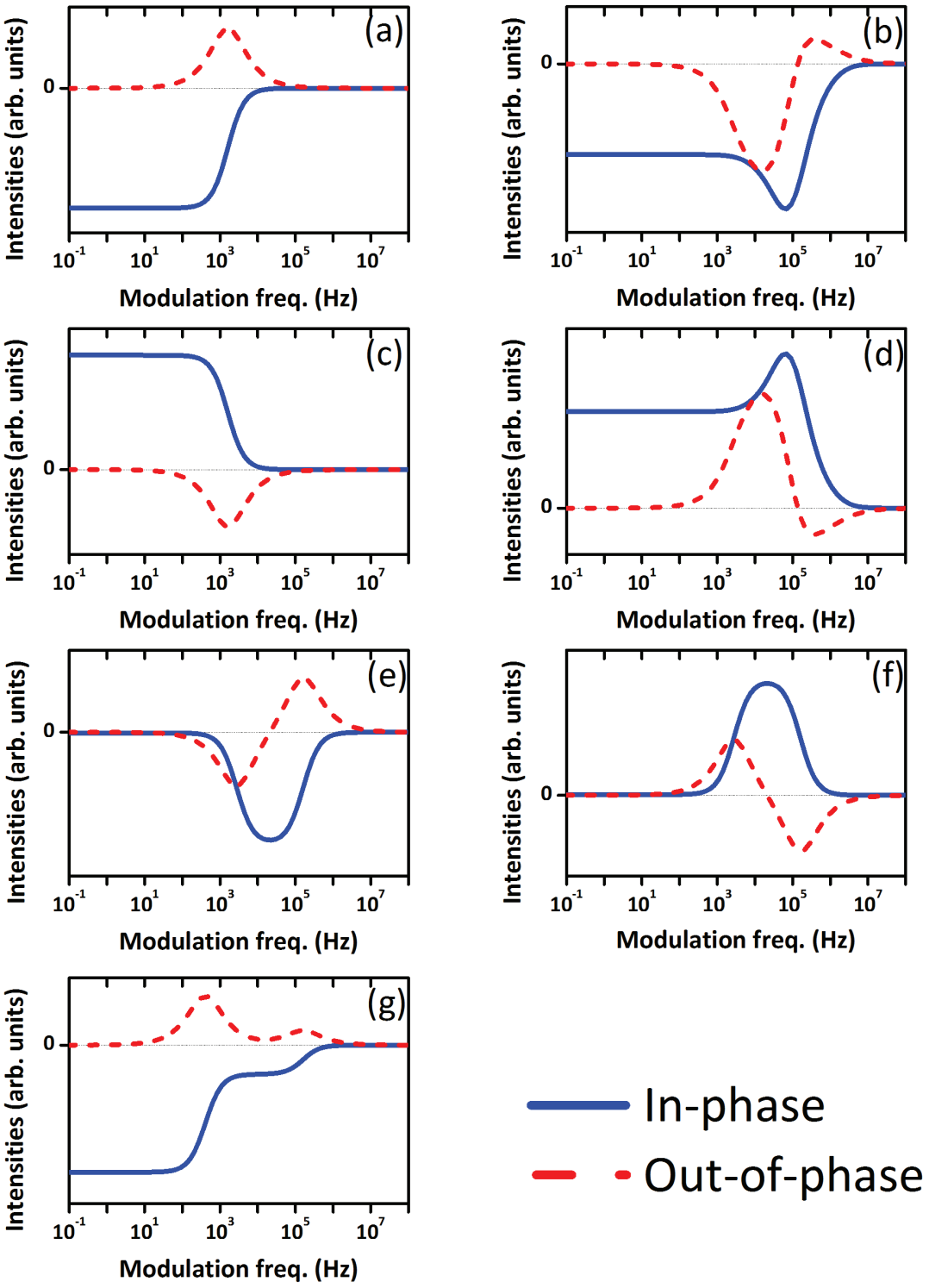

Figure 2.5. Seven distinguishable patterns of the modulation frequency dependence of cwODMR have been found out of almost a thousand quantitative models. (b), (d), and (f) are equivalent with (a), (c), and (e), respectively, but with opposite signs. Note that the parameters used for these data are listed in Table 2.1.

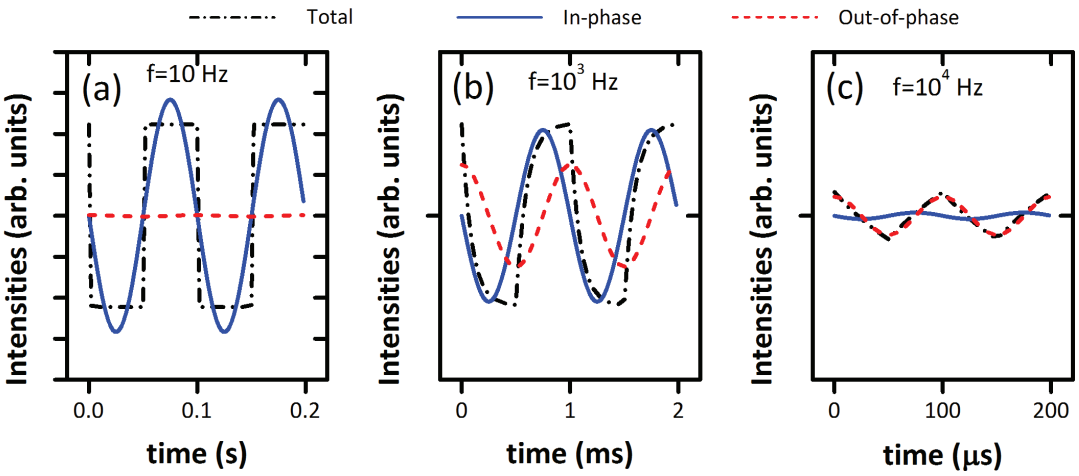

Figure 2.6. Calculated transient behaviors at different modulation frequencies. Black dash-dot line is overall response and blue solid line and red dashed line are in-phase and out-of phase components of it. Parameters are the same as those in Fig. 2.4 (a). The three graphs are normalized by the same scaling factor. Thus the relative intensities among three graphs can be compared.

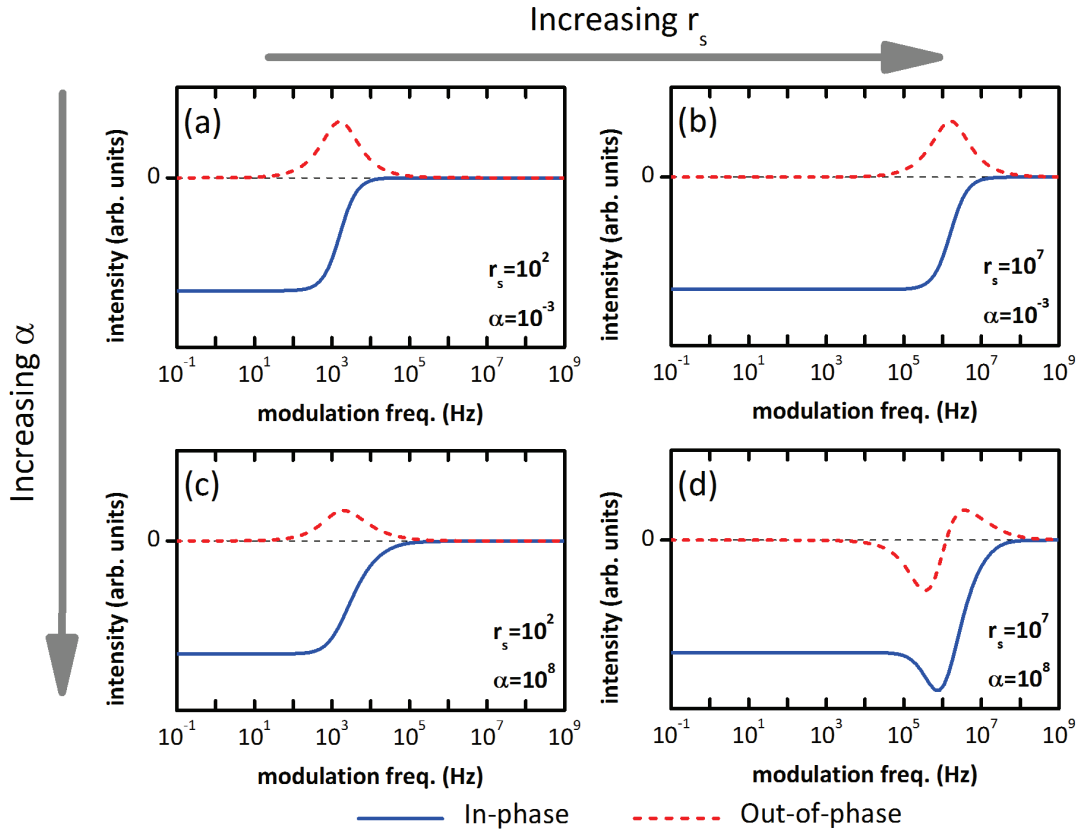

Figure 2.7. Role of the singlet recombination rate, r_s. When r_s is small, no significant change in the frequency dependence pattern is found when α is increased (from (a) to (c)). But for large r_s, a pattern change is observed when α is increased (from (b) to (d)). All four quantitative models have same combinations of parameters but (a) $r_s = 10^2$, $\alpha = 10^{-3}$, (b) $r_s = 10^7$, $\alpha = 10^{-3}$, (c) $r_s = 10^2$, $\alpha = 10^8$, and (d) $r_s = 10^7$, $\alpha = 10^8$. Values for the other parameters used for these data are listed in Table 2.1.

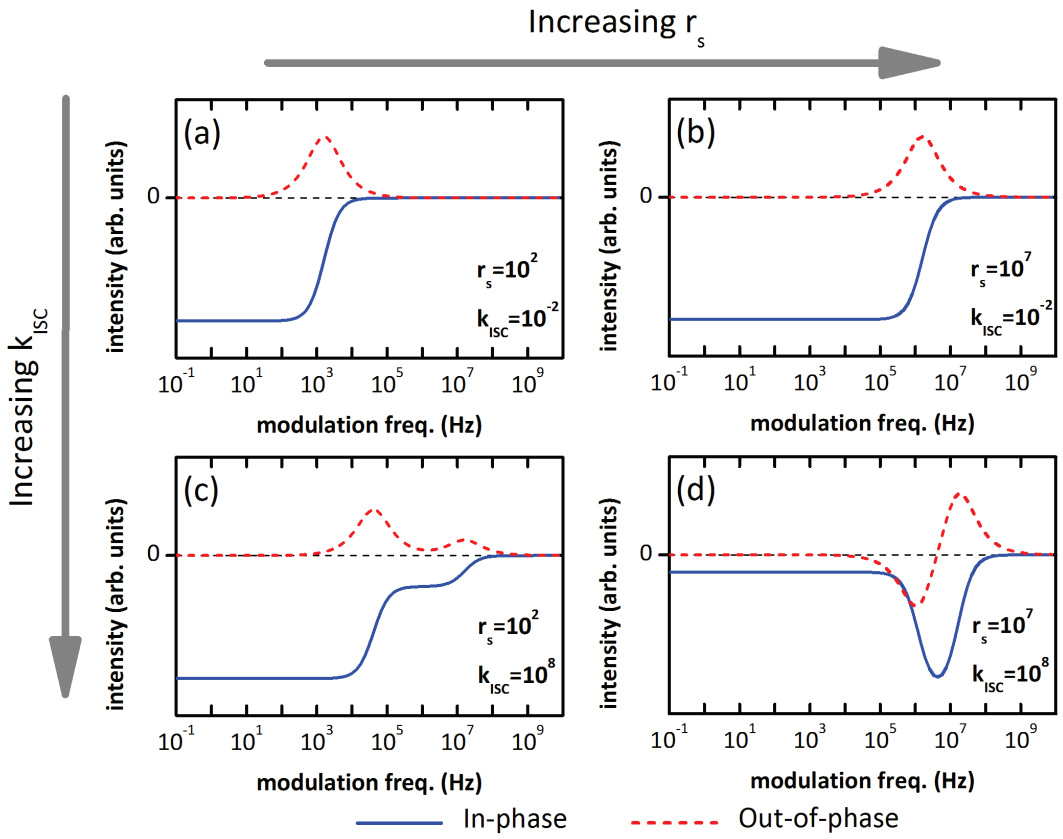

Figure 2.8. Role of the intersystem-crossing rate, k_{ISC}. At small r_s, it has been observed that there appear bumps on both in-phase and out-of-phase signal at high frequency region when k_{ISC} becomes large (from (a) to (c)). At large r_s, different pattern change also has been found. The in-phase shows local extrema and out-of-phase shows change of sign as k_{ISC} being increased (from (b) to (d)). All four quantitative models have same combinations of parameters but (a) $r_s = 10^2$, $k_{ISC} = 10^{-2}$, (b) $r_s = 10^7$, $k_{ISC} = 10^{-2}$, (c) $r_s = 10^2$, $k_{ISC} = 10^8$, (d) $r_s = 10^7$, $k_{ISC} = 10^8$. The other parameter values used for these data are listed in Table 2.1.

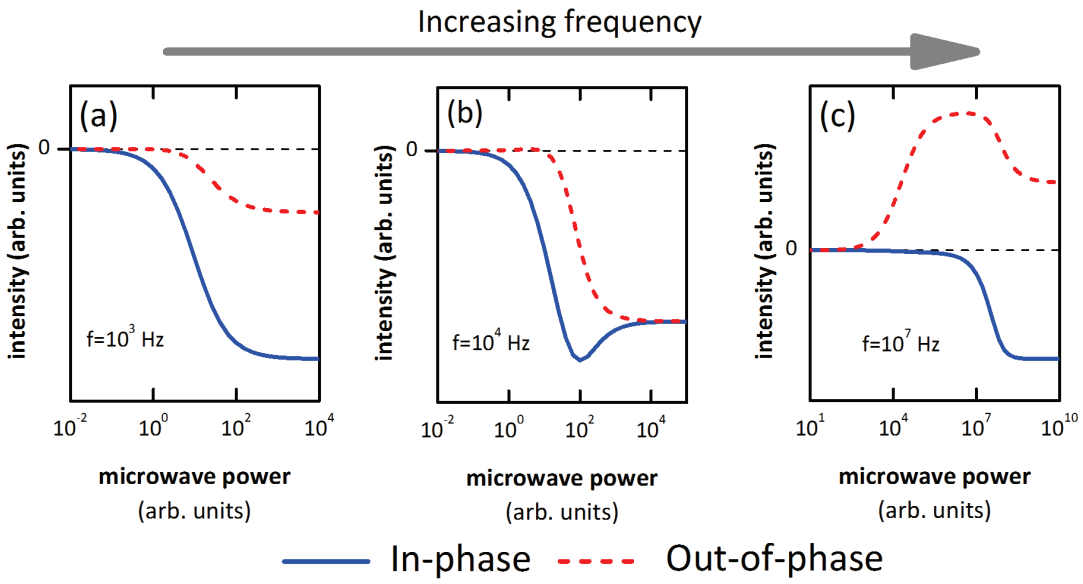

Figure 2.9. MW power dependence. All four quantitative models have the same combinations of parameters but (a) $f = 10^3$, (b) $f = 10^4$, (c) $f = 10^7$. At low modulation frequencies, typical saturation curves can be found. At high modulation frequency, a nontrivial saturation behavior occurs. Refer to Table 2.1 for the values used for the other parameters.

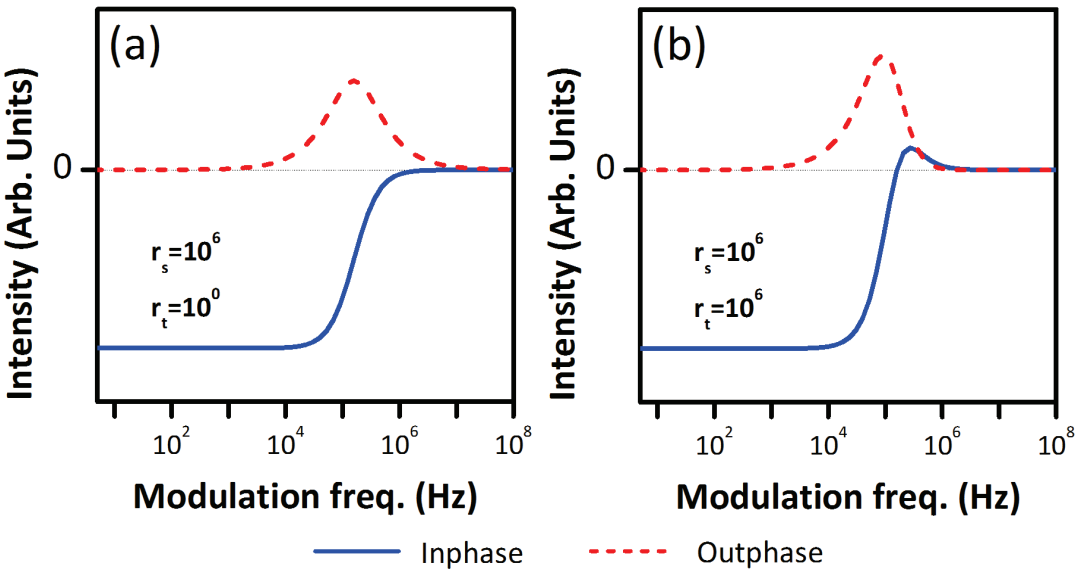

Figure 2.10. Example of a modulation frequency dependence function showing a change from nonzero-crossing pattern to a zero-crossing pattern. The only difference between the two quantitative models can be found in the triplet recombination rate coefficients. (a) $r_t = 10^0$, (b) $r_t = 10^6$. Values for the other parameters are listed in Table 2.1.

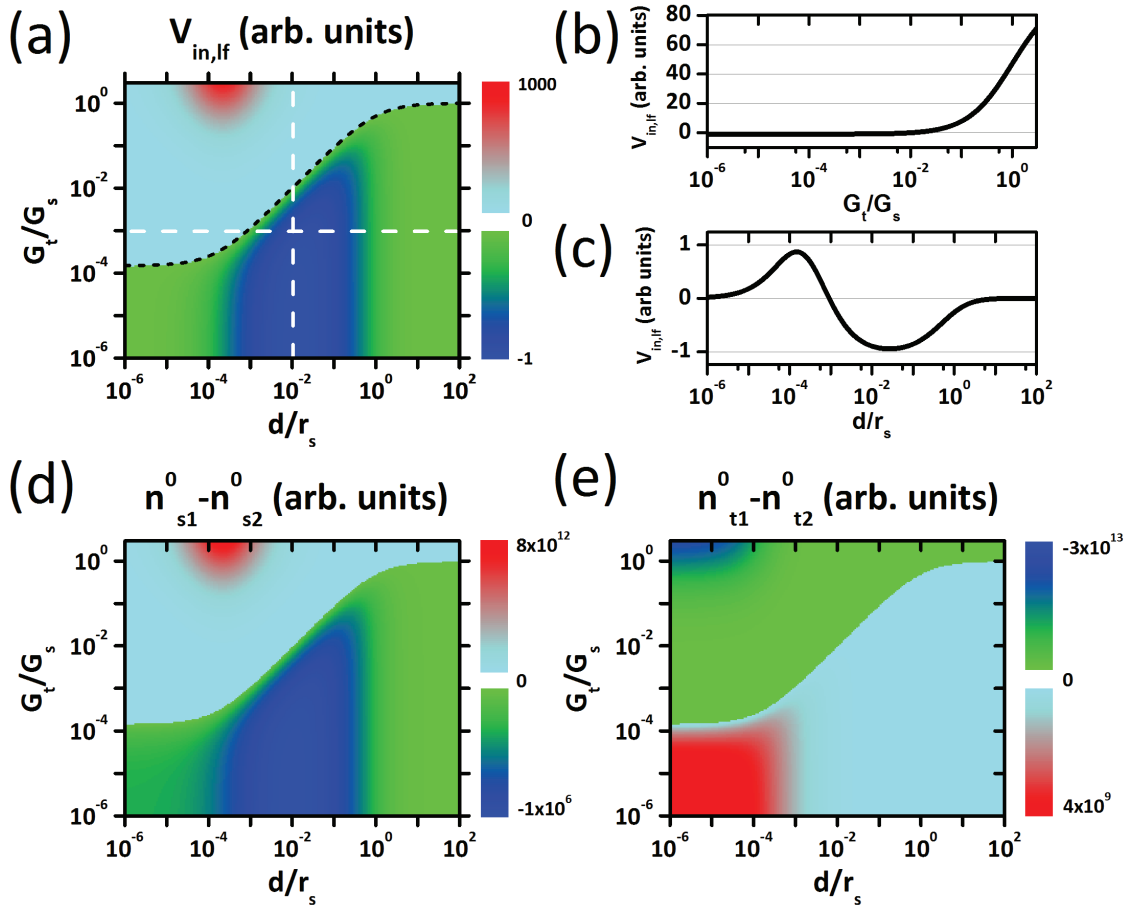

Figure 2.11. Sign changes due to various rate coefficients. (a) In-phase intensities of the zero modulation frequency component as a function of G_t/G_s and d/r_s. To distinguish positive values and negative values, different color scales are used (positive in upper left corner, and negative in lower right corner). The black dotted line describes the boundary separating positive values and negative values. (b) and (c) are two randomly chosen two dimensional subsets of the data in (a) representing a generation rate ratio slice and dissociation rate ratio dependencies. These slices are shown as white dashed lines in (a). Intensities in (a), (b), and (c) are normalized but in the same scale. (d) Changes in the numbers of singlet pairs, $n^0_{s1} - n^0_{s2}$ as a function of the same parameters as in (a). (e) Changes in the number of triplets pairs, $n^0_{t1} - n^0_{t2}$ as a function of the same parameters as in (a). Intensities in (d) and (e) are normalized but in the same scale. All calculations in this figure are obtained from the same condition of $r_s = 10^4$, $r_t = 1$, $k_{ISC} = 1$, $\alpha = 1$, $\rho = 0.75$, $G_s + G_t = 10^{16}$.

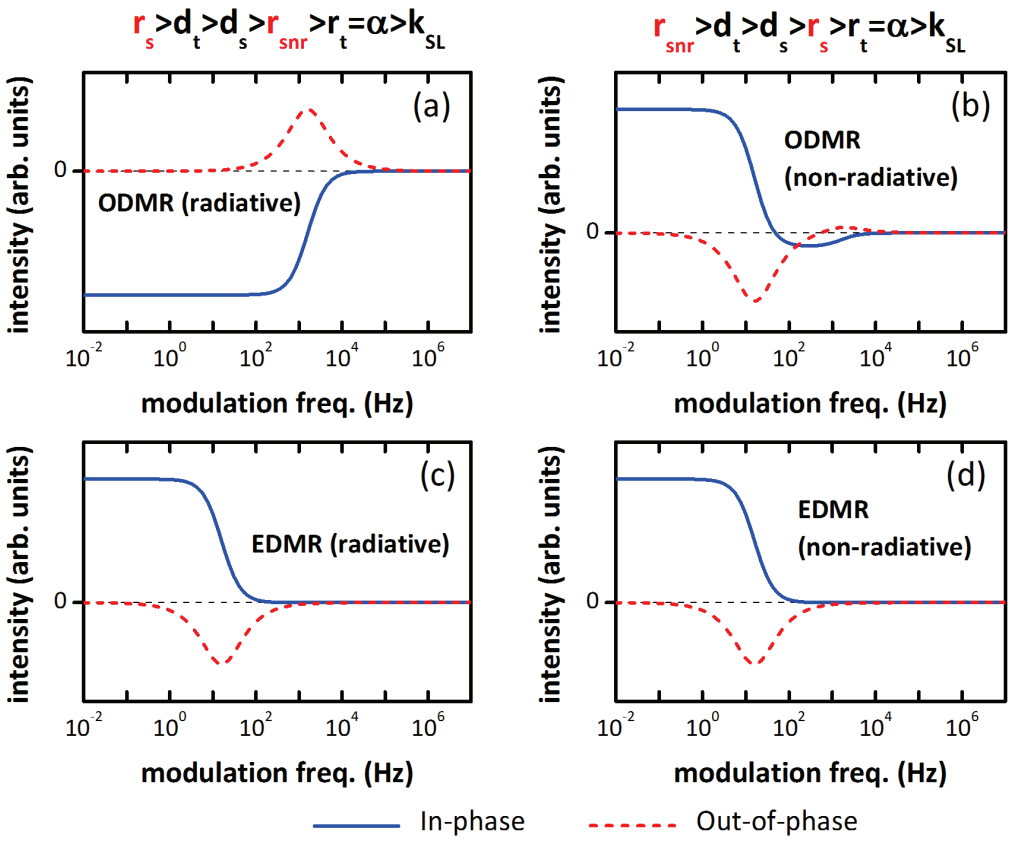

Figure 2.12. The sign of cwODMR signals can be negative when radiative recombination is dominant as in (a), and positive when nonradiative recombination is dominant as in (b). In contrast the signs of cwEDMR are not different, (c) and (d). Used common values for each rate parameters can be found in Table 2.1. (a) and (c) $r_s = 10^4$, $r_{s,nr} = 1$. (b) and (d) $r_s = 1$, $r_{s,nr} = 10^4$.

Table 2.1. Parameters used for calculation of all plotted data in this chapter. All values have a unit of s^{-1} except for ρ which is arbitrary.

		r_s	$r_{s,nr}$	r_t	d_s	d_t	k_{ISC}	α	ρ	G_s	G_t	f
2.3		10^4	0	1	10^2	10^6	10^{-2}	10^5	0.75	10^{23}	10^{20}	-
2.4	(a)	10^2	0	1	10^4	10^6	10^{-2}	10^3	0.75	10^{23}	10^{20}	-
	(b)	10^4	0	10^{-1}	10	10^2	10^{-2}	10^{-1}	0.75	10^{25}	10^{20}	-
	(c)	10^4	0	1	10^2	10^6	10^{-2}	10^3	0.75	$10^{20}/3$	10^{20}	-
2.5	(a)	10^4	0	1	10^2	10^3	10^{-2}	10^{-3}	0.75	10^{24}	10^{20}	-
	(b)	10^6	0	1	10^2	10^4	10^{-2}	10^7	0.75	10^{22}	10^{20}	-
	(c)	10^4	0	1	10^2	10^3	10^{-2}	10^{-3}	0.75	$10^{20}/3$	10^{20}	-
	(d)	10^6	0	1	10^2	10^4	10^{-2}	10^7	0.75	$10^{20}/3$	10^{20}	-
	(e)	10^6	0	10^4	1	10^2	10^4	10^{-3}	0.75	10^{24}	10^{20}	-
	(f)	10^6	0	10^4	1	10^2	10^4	10^{-3}	0.75	$10^{20}/3$	10^{20}	-
	(g)	1	0	10^{-1}	10^2	10^4	10^6	10^{-3}	0.75	$10^{20}/3$	10^{20}	-
2.7	(a)	10^2	0	1	10^4	10^6	10^{-2}	10^{-3}	0.75	10^{22}	10^{20}	-
	(b)	10^7	0	1	10^4	10^6	10^{-2}	10^{-3}	0.75	10^{22}	10^{20}	-
	(c)	10^2	0	1	10^4	10^6	10^{-2}	10^8	0.75	10^{22}	10^{20}	-
	(d)	10^7	0	1	10^4	10^6	10^{-2}	10^8	0.75	10^{22}	10^{20}	-
2.8	(a)	10^2	0	1	10^4	10^6	10^2	10^1	0.75	10^{22}	10^{20}	-
	(b)	10^7	0	1	10^4	10^6	10^{-2}	10^1	0.75	10^{22}	10^{20}	-
	(c)	10^2	0	1	10^4	10^6	10^8	10^1	0.75	10^{22}	10^{20}	-
	(d)	10^7	0	1	10^4	10^6	10^8	10^1	0.75	10^{22}	10^{20}	-
2.9	(a)	10^6	0	1	10^2	10^4	10^{-2}	-	0.75	10^{22}	10^{20}	10^3
	(b)	10^6	0	1	10^2	10^4	10^{-2}	-	0.75	10^{22}	10^{20}	10^4
	(c)	10^6	0	1	10^2	10^4	10^{-2}	-	0.75	10^{22}	10^{20}	10^7
2.10	(a)	10^6	0	1	10^2	10^4	10^{-2}	10^1	0.75	10^{22}	10^{20}	-
	(b)	10^6	0	10^6	10^2	10^4	10^{-2}	10^1	0.75	10^{22}	10^{20}	-
2.11		10^4	0	1	-	-	1	1	0.75	$G_s + G_t = 10^{16}$		-
2.12	(a)	10^4	1	10^{-1}	10	10^2	10^{-2}	10^{-1}	0.75	10^{25}	10^{20}	-
	(b)	10^4	1	10^{-1}	10	10^2	10^{-2}	10^{-1}	0.75	10^{25}	10^{20}	-
	(c)	1	10^4	10^{-1}	10	10^2	10^{-2}	10^{-1}	0.75	10^{25}	10^{20}	-
	(d)	1	10^4	10^{-1}	10	10^2	10^{-2}	10^{-1}	0.75	10^{25}	10^{20}	-

2.8 References

[1] S. Geschwind, R. J. Collins, and A. L. Schawlow. *Physical Review Letters*, 3:545, 1959.

[2] J. Brossel, G. Geschwind, and A. L. Schawlow. *Physical Review Letters*, 3:548–549, 1959.

[3] B. C. Cavenett. *Advances in Physics*, 30:475–538, 1981.

[4] R. A. Street. *Physical Review B*, 26:3588–3604, 1982.

[5] S. Depinna, B. C. Cavenett, I. G. Austin, T. M. Searle, M. J. Thompson, J. Allison, and P. G. L. Comberd. *Philosophical Magazine B*, 46:473 – 500, 1982.

[6] E. Lifshitz, L. Fradkin, A. Glozman, and L. Langof. *Annual Review of Physical Chemistry*, 55:509–557, 2004.

[7] M. Stutzmann, M. S. Brandt, and M. W. Bayerl. *Journal of Non-Crystalline Solids*, 266-269:22, 2000.

[8] W. M. Chen. *Thin Solid Films*, 364:45–52, 2000.

[9] F. Boulitrop. *Physical Review B*, 28:6192, 1983.

[10] D. R. McCamey, H. Huebl, M. S. Brandt, W. D. Hutchison, J. C. McCallum, R. G. Clark, and A. R. Hamilton. *Applied Physics Letters*, 89:182115–3, 2006.

[11] D. J. Dunstan and J. J. Davies. *Journal of Physics C: Solid State Physics*, 12:2927–2944, 1979.

[12] S. Depinna, B. C. Cavenett, I. G. Austin, T. M. Searle, M. J. Thompson, J. Allison, and P. G. L. Comberd. *Philosophical Magazine B*, 46:501 – 513, 1982.

[13] K. Morigaki, D. J. Dunstan, B. C. Cavenett, P. Dawson, J. E. Nicholls, S. Nitta, and K. Shimakawa. *Solid State Communications*, 26:981–985, 1978.

[14] P. M. Lenahan and W. K. Schubert. *Physical Review B*, 30:3, 1984.

[15] H. Dersch, L. Schweitzer, and J. Stuke. *Physical Review B*, 28:4678, 1983.

[16] H. Morishita, L. S. Vlasenko, H. Tanaka, K. Semba, K. Sawano, Y. Shiraki, M. Eto, and K. M. Itoh. *Physical Review B*, 80:205206, 2009.

[17] E. Lifshitz, L. Bykov, M. Yassen, and Z. Chen-Esterlit. *Chemical Physics Letters*, 273:381–388, 1997.

[18] E. Lifshitz, A. Glozman, I. D. Litvin, and H. Porteanu. *The Journal of Physical Chemistry B*, 104:10449–10461, 2000.

[19] L. Langof, E. Ehrenfreund, E. Lifshitz, O. I. Micic, and A. J. Nozik. *Journal of Physical Chemistry B*, 106:1606–1612, 2002.

[20] P. Kanschat, K. Lips, and W. Fuhs. *Journal of Non-Crystalline Solids*, 266-269:5, 2000.

[21] E. R. Glaser, T. A. Kennedy, K. Doverspike, L. B. Rowland, D. K. Gaskill, J. A. Freitas, M. Asif Khan, D. T. Olson, J. N. Kuznia, and D. K. Wickenden. *Physical Review B*, 51:13326, 1995.

[22] E. R. Glaser, J. A. Freitas, B. V. Shanabrook, D. D. Koleske, S. K. Lee, S. S. Park, and J. Y. Han. *Physical Review B*, 68:195201, 2003.

[23] N. T. Son, E. Sörman, W. M. Chen, C. Hallin, O. Kordina, B. Monemar, and E. Janzén. *Physical Review B*, 55:2863, 1997.

[24] E. v. Oort, N. B. Manson, and M. Glasbeek. *Journal of Physics C: Solid State Physics*, 21:4385, 1988.

[25] M. H. Nazare, P. W. Mason, G. D. Watkins, and H. Kanda. *Physical Review B*, 51:16741, 1995.

[26] A. P. Nizovtsev, S. Y. Kilin, C. Tietz, F. Jelezko, and J. Wrachtrup. *Physica B: Condensed Matter*, 308-310:608–611, 2001.

[27] L. S. Swanson, J. Shinar, and K. Yoshino. *Physical Review Letters*, 65:1140, 1990.

[28] L. S. Swanson, P. A. Lane, J. Shinar, and F. Wudl. *Physical Review B*, 44:10617, 1991.

[29] L. S. Swanson, J. Shinar, A. R. Brown, D. D. C. Bradley, R. H. Friend, P. L. Burn, A. Kraft, and A. B. Holmes. *Physical Review B*, 46:15072, 1992.

[30] W. Graupner, J. Partee, J. Shinar, G. Leising, and U. Scherf. *Physical Review Letters*, 77:2033, 1996.

[31] N. C. Greenham, J. Shinar, J. Partee, P. A. Lane, O. Amir, F. Lu, and R. H. Friend. *Physical Review B*, 53:13528, 1996.

[32] P. A. Lane, X. Wei, and Z. V. Vardeny. *Physical Review B*, 56:4626, 1997.

[33] G. B. Silva, L. F. Santos, R. M. Faria, and C. F. O. Graeff. *Physica B: Condensed Matter*, 308-310:1078–1080, 2001.

[34] E. J. W. List, U. Scherf, K. Müllen, W. Graupner, C. H. Kim, and J. Shinar. *Physical Review B*, 66:235203, 2002.

[35] R. Österbacka, M. Wohlgenannt, M. Shkunov, D. Chinn, and Z. V. Vardeny. *The Journal of Chemical Physics*, 118:8905–8916, 2003.

[36] M. K. Lee, M. Segal, Z. G. Soos, J. Shinar, and M. A. Baldo. *Physical Review Letters*, 94:137403, 2005.

[37] M. Segal, M. A. Baldo, M. K. Lee, J. Shinar, and Z. G. Soos. *Physical Review B*, 71:245201, 2005.

[38] C. G. Yang, E. Ehrenfreund, F. Wang, T. Drori, and Z. V. Vardeny. *Physical Review B*, 78:6, 2008.

[39] F. A. Castro, G. B. Silva, F. Nüesch, L. Zuppiroli, and C. F. O. Graeff. *Organic Electronics*, 8:249–255, 2007.

[40] G. Li, C. H. Kim, P. A. Lane, and J. Shinar. *Physical Review B*, 69:165311, 2004.

[41] F. A. Castro, G. B. Silva, L. F. Santos, R. M. Faria, F. Nüesch, L. Zuppiroli, and C. F. O. Graeff. *Journal of Non-Crystalline Solids*, 338-340:622–625, 2004.

[42] I. Hiromitsu, Y. Kaimori, M. Kitano, and T. Ito. *Physical Review B*, 59:2151, 1999.

[43] M. C. Scharber, N. A. Schultz, N. S. Sariciftci, and C. J. Brabec. *Physical Review B*, 67:085202, 2003.

[44] T. D. Nguyen, G. Hukic-Markosian, F. Wang, L. Wojcik, X.-G. Li, E. Ehrenfreund, and Z. V. Vardeny. *Nature Materials*, 9:345–352, 2010.

[45] C. G. Yang, E. Ehrenfreund, and Z. V. Vardeny. *Physical Review Letters*, 99:4, 2007.

[46] V. Dyakonov and E. Frankevich. *Chemical Physics*, 227:203–217, 1998.

[47] E. J. W. List, C. H. Kim, A. K. Naik, U. Scherf, G. Leising, W. Graupner, and J. Shinar. *Physical Review B*, 64:155204, 2001.

[48] V. Dyakonov, G. Rösler, M. Schwoerer, and E. L. Frankevich. *Physical Review B*, 56:3852, 1997.

[49] B. Stich, S. Greulich-Weber, and J. M. Spaeth. *Journal of Applied Physics*, 77:1546–1553, 1995.

[50] D. K. Biegelsen, J. C. Knights, R. A. Street, C. Tsang, and R. M. White. *Philosophical Magazine Part B*, 37:477–488, 1978.

[51] Z. Xiong and D. J. Miller. *Applied Physics Letters*, 63:352–354, 1993.

[52] G. Kawachi, C. F. O. Graeff, M. S. Brandt, and M. Stutzmann. *Japanese Journal of Applied Physics*, 36:5, 1997.

[53] M. A. Baldo, M. Segal, J. Shinar, and Z. G. Soos. *Physical Review B*, 75:3, 2007.

[54] C. G. Yang, E. Ehrenfreund, M. Wohlgenannt, and Z. V. Vardeny. *Physical Review B*, 75:5, 2007.

[55] S. P. Depinna. *Physical Review B*, 28:5327, 1983.

[56] W. E. Carlos and S. Nakamura. *Journal of Crystal Growth*, 189-190:794–797, 1998.

[57] D. Kaplan, I. Solomon, and N. F. Mott. *J. Physique Lett.*, 39:51–54, 1978.

[58] C. Boehme and K. Lips. *Applied Physics Letters*, 79:4363–4365, 2001.

[59] C. Boehme and K. Lips. *Physical Review B*, 68:245105, 2003.

[60] K. Lips, C. Boehme, and T. Ehara. *Journal of Optoelectronics and Advanced Materials*, 7:13, 2005.

[61] A. R. Stegner, C. Boehme, H. Huebl, M. Stutzmann, K. Lips, and M. S. Brandt1. *Nature Physics*, 2:835, 2006.

[62] F. Jelezko and J. Wrachtrup. *Physica Status Solidi (a)*, 203:3207–3225, 2006.

[63] D. R. McCamey, H. A. Seipel, S.-Y. Paik, M. J. Walter, N. J. Borys, J. M. Lupton, and C. Boehme. *Nature Materials*, 7:723, 2008.

[64] T. W. Herring, S.-Y. Lee, D. R. McCamey, P. C. Taylor, K. Lips, J. Hu, F. Zhu, A. Madan, and C. Boehme. *Physical Review B*, 79:195205, 2009.

[65] P. Neumann, R. Kolesov, V. Jacques, J. Beck, J. Tisler, A. Batalov, L. Rogers, N. B. Manson, G. Balasubramanian, F. Jelezko, and J. Wrachtrup. *New Journal of Physics*, 11:013017, 2009.

[66] S.-Y. Lee, S.-Y. Paik, D. R. McCamey, J. Hu, F. Zhu, A. Madan, and C. Boehme. *Applied Physics Letters*, 97:192104–3, 2010.

[67] D. J. Lepine. *Physical Review B*, 6:436, 1972.

[68] M. S. Brandt, M. W. Bayerl, M. Stutzmann, and C. F. O. Graeff. *Journal of Non-Crystalline Solids*, 227-230:343–347, 1998.

[69] M. Stutzmann and M. S. Brandt. *Journal of Non-Crystalline Solids*, 141:97–105, 1992.

[70] A. D. McNaught, A. Wilkinson, International Union of Pure, and Applied Chemistry. *Compendium of chemical terminology : IUPAC recommendations*. Blackwell Science, Oxford England ; Malden, MA, USA, 2nd edition, 1997.

[71] T. Eickelkamp, S. Roth, and M. Mehring. *Molecular Physics: An International Journal at the Interface Between Chemistry and Physics*, 95:967–972, 1998.

[72] T. Aoki. *Journal of Non-Crystalline Solids*, 352:1138–1143, 2006.

[73] V. D. Mihailetchi, H. Xie, B. d. Boer, L. J. A. Koster, and P. W. M. Blom. *Advanced Functional Materials*, 16:699–708, 2006.

[74] Y. V. Romanovskii, A. Gerhard, B. Schweitzer, R. I. Personov, and H. Bässler. *Chemical Physics*, 249:29–39, 1999.

[75] Y. Tachibana, J. E. Moser, M. Gratzel, D. R. Klug, and J. R. Durrant. *The Journal of Physical Chemistry*, 100:20056–20062, 1996.

[76] A. Nollau, M. Hoffmann, T. Fritz, and K. Leo. *Thin Solid Films*, 368:130–137, 2000.

[77] D. R. McCamey, S. Y. Lee, S. Y. Paik, J. M. Lupton, and C. Boehme. *Physical Review B*, 82:125206, 2010.

[78] R. A. Street. *Hydrogenated Amorphous Silicon*. Cambridge University Press, New York, 1991.

[79] J. I. Pankove. *Optical processes in semiconductors*. Dover Publications, New York, 1971.

[80] D. D. C. Bradley and R. H. Friend. *Journal of Physics: Condensed Matter*, 1:3671, 1989.

[81] M. Wohlgenannt, C. Yang, and Z. V. Vardeny. *Physical Review B*, 66:4, 2002.

[82] P. W. Atkins and R. S. Friedman. *Molecular quantum mechanics*. Oxford University Press, Oxford, third edition, 1999.

CHAPTER 3

UNDERSTANDING PULSED EDMR AND ODMR SPECTROSCOPIES

CwODMR and cwEDMR provide information about the Landé g-factor of paramagnetic centers which influence luminescence and conductivity through spin-dependent transitions. Line shape analysis can in principle also provide information about the nature of a spin-dependent process (spin- and electronic relaxation rates, dissociation rates etc.), however, for many experimentally observed cwODMR and cwEDMR spectra, this approach is oftentimes extremely ambiguous due to strong convolution of several resonances which are usually all centered around $g = 2$.

The ambiguity of cwODMR and cwEDMR spectra can be overcome by time domain measurements especially on very short, coherent time scales. Similar as for coherent (so called pulsed, "p") ESR and pNMR experiments, the observation of coherent spin motion allows a much less ambiguous reconstruction of the Hamiltonian and thus, an extraction of spin-spin coupling parameters (e.g., exchange and dipolar coupling), or hyperfine fields caused by surrounding nuclei [1–4]. In addition, similar to the cw methods discussed in the previous chapter, pEDMR and pODMR can also reveal direct information about the dynamics of the spin-dependent electronic processes which are involved in these signals. This will be discussed in the following and an experimental setup for a pODMR and pEDMR experiment is shown in Fig. 3.1.

Some of the following sections are based on a journal article published in Physical Review B in the year 2010 coauthored by Dane R. McCamey, Seoyoung Paik, and Christoph Boehme.[1] The original article is written in the context of polaron pair recombination dynamics. A number of the sections in this chapter are not part of this article and those which have been extended towards a more general description of spin-dependent pair processes in semiconductors.

---

[1]D. R. McCamey, S. Y. Lee, S. Y. Paik, J. M. Lupton and C. Boehme, Physical Review B 82 (12), 125206 (2010).

3.1 History of development of pEDMR and pODMR

After the first ESR experiment was demonstrated by by Zavoisky [5] in 1945, the first NMR experiment was demonstrated by Bloch and Purcell et al. [6, 7] in 1946. Shortly after these demonstrations, the development of pulsed magnetic resonance experiments began: Nuclear spin echoes were observed for the first time by Hahn [8] in 1950 and Fourier transform NMR was developed after 1966 by Ernst and Anderson [9]. Many sophisticated experiments became possible thanks to the development of pulse techniques: for instance, Hahn echo pulse sequence allows very accurate spin relaxation time measurements compared to conventional linewidth analysis. The first electron spin echo was reported by Blume in 1958 [10]. In contrast to NMR, pulse ESR techniques always followed pulsed NMR by one to two decades because the dynamics of coherent spin motion of electrons typically takes place on a several orders of magnitude faster time scale than the nuclear spin dynamics. Electron spin relaxation times are orders of magnitude shorter than nuclear spin relaxation times [11]. Thus, an extremely accurate detection method is required for pESR and, therefore, pulsed ESR had not been widely used until mid 1980s.

While the development of pESR progressed, first pODMR experiments were conducted, too. The first optical detection of coherent electron spin echos as well as transient nutations (Rabi nutations) using pODMR was presented by Breiland et al. [12]. Electron spin echo envelope modulation (ESEEM) by pODMR was reported later by Weis et al. for the first time [13]. While pODMR had been established around the early 1980s and has since been used to investigate the recombination dynamics of many spin-dependent processes [13], the development of pEDMR did not take place until almost three decades later.

The most demanding technical challenge for pEDMR is to prevent the very powerful electromagnetic fields used for the coherent spin excitation (the B_1 fields are usually in the microwave rage) from distorting the measured spin-dependent electric currents. In order to achieve this, a special contact design must be used on pEDMR samples. Another requirement for a pEDMR experiment is the availability of a fast detection setup for very small current changes. First time domain EDMR experiments were reported by Hiromitsu et al. in 1999. These experiments were conducted on organic semiconductors [14], yet with a time resolution which did not allow the electrical detection of coherent spin motion. The first electrical detection of coherent electron spin motion was reported by Boehme and Lips in 2002 [15]: the echo induced by the abrupt phase change during a resonant microwave pulse was detected via detection of a change in the photocurrent in hydrogenated microcrystalline silicon. This first electrically detected coherent electron spin experiment

was followed shortly thereafter by the first demonstration of electrically detected coherent nuclear spin motion as reported by Machida et al. [16].

Since first pEDMR experiments were performed, a variety of theoretical work on pEDMR signals have been reported. Boehme and Lips reported the first theoretical description in 2003 by providing analytical solutions for (i) the photocurrent change on an incoherent time scale induced by a short resonant pulse, (ii) electrically detected coherent Rabi oscillation under consideration of wide a range of spin-spin interactions, and (iii) electrically detected rotary echoes [1]. For the calculation of the Liouville operator, they did not use the Liouville equation but instead, they directly applied rotation operators to an initial state. This approach allowed them to obtain analytical solutions for weakly coupled spin pairs on resonance. These results were applicable to a broad variety of experimental systems [17–21], including systems with relevant effects of inhomogeneous broadening on Rabi oscillation [3, 22], and Rabi frequency doubling due to small Larmor separation [2, 3, 23]. One of the surprising outcomes of these studies is that a doubling of an observed electrically detected Rabi frequency is seen under strong excitation where power broadening exceeds the Larmor separation (= the difference of the Larmor frequencies within a spin pair). This effect is also visible with pODMR experiments, yet it is not visible with pESR detected transient nutation experiments. A further theoretical investigation of this effect was conducted by Rajevac et al. who solved the Liouville equation numerically, again under assumption of weak exchange and dipolar coupling but for both the on-resonant and off-resonant (detuned) case [24]. Gliesche et al. continued this research by considering the presence of strong exchange coupling [4] which revealed that a Rabi frequency doubling effect can also occur due to exchange interaction. This exchange induced electrical detected Rabi frequency doubling has been verified experimentally since then in amorphous silicon-rich silicon nitride [25] (this work is part of this dissertation) after it had been observed previously by pODMR on amorphous silicon [26–28]. Finally, the influence of structural inhomogeneities on electrically and optically detected electron spin nutation was investigated theoretically by Michel et al. [29].

The Observation of pEDMR and pODMR in the incoherent time domain provides information about the spontaneous transition rates to which the spin-pairs are subjected. These include electronic transition rates, intersystem-crossing rates and other spin-relaxation processes. While a first, simple analytical solution for the current change induced by a resonant pulse, based on the intermediate pair recombination model, was reported by Boehme and Lips in 2001 [30], a more detailed solution was reported by McCamey et al.

in 2008 [18]. Both solutions were based on the intermediate pair recombination model in which spins in a pair are assumed to be weakly coupled, and they could explain the double exponential behavior of the transient current detected by pEDMR and pODMR [17–21]. However, there was a limit to the applicability of these solutions for the extraction of exact rates because the spin mixing processes due to any possible intersystem-crossing were assumed to be negligible in both solutions. This limit can be overcome by solving rate equations including intersystem-crossing process analytically, similar as it has been done for cwEDMR and cwODMR transients in the previous chapter. The following sections outline the results of this work.

3.2 Incoherent pEDMR and pODMR

First, the steady state solutions of the rates that determine pEDMR and pODMR signals will be discussed before analytical solutions for different spin-pair scenarios will be presented.

3.2.1 Rate model

We use the same rate model that was discussed in Chapter 2 for the description of cwODMR and cwEDMR experiments. In contrast to the cw experiments, the spin-mixing rate now does not depend on a microwave anymore, as any spin-excitation is pulsed and considered to be infinitely short while the subsequent transition of the spin ensemble takes place in absence of any resonant excitation ($\alpha = 0$). Thus,

$$\frac{dn_s}{dt} = G_s - C_s n_s - k_{ISC}(n_s - \rho n_s) + k_{ISC}(n_t - (1-\rho)n_t), \tag{3.1}$$

$$\frac{dn_t}{dt} = G_t - C_t n_t - k_{ISC}(n_t - (1-\rho)n_t) + k_{ISC}(n_s - \rho n_s), \tag{3.2}$$

and similarly to Chapter 2, the solutions for these rate equations

$$n_{sp}(t) = A_{1p}e^{-m_{12}t} + A_{2p}e^{-m_{22}t} + n^0_{s2}, \tag{3.3}$$

$$n_{tp}(t) = B_{1p}e^{-m_{12}t} + B_{2p}e^{-m_{22}t} + n^0_{t2}, \tag{3.4}$$

are biexponential decay functions which correspond to eqs. 2.10 and 2.11 except that the coefficients, A_{1p}, A_{2p}, B_{1p}, B_{2p}, in front of exponential terms are different due to different boundary conditions.

3.2.1.1 Steady-state solutions

In the following we will briefly discuss the properties of the steady-state solutions, n^0_{s2} and n^0_{t2} (eqs. 2.14 and 2.15), as a function of the intersystem-crossing rate, k_{ISC}, and the

Fermi-Dirac distribution ρ. The steady-state values for the two limiting cases, $k_{ISC} \to 0$ and $k_{ISC} \to \infty$, are shown in Table 3.1. When k_{ISC} is small, we obtain the simple steady-state values, G_s/C_s and G_t/C_t for singlet and triplet pair densities, respectively.

These terms reflect that the relaxation of each of the two permutation symmetry densities are determined only by the spin pair annihilation process, C_s and C_t, and their behavior becomes independent on ρ. When k_{ISC} becomes fast, the steady state terms become more complex. When $\rho \to 1/2$, the two steady-state values become indistinguishable because fast k_{ISC} minimizes the different permutation symmetry densities. However when $\rho \to 1$, for example at very low temperatures, the two steady state densities remain distinguishable even when k_{ISC} is fast: The triplet density becomes very low while the singlet density becomes very high. Note that this behavior comes from an assumed energetically lower singlet pair state. If the triplet pair state is lower, the densities will behave in an opposite way. The behaviors of the permutation symmetry densities are plotted in Fig. 3.2. In Fig. 3.2 (a), $n_s^0 < n_t^0$ at slow k_{ISC}, because steady-state values are determined only by G_s/C_s and G_t/C_t, respectively, and $C_s/C_t \simeq 4$ while $G_t/G_s = 3$.

Thus when both triplet and singlet generation rates are comparable, the steady-state values are mostly determined by the pair annihilation rates, so the steady-state value of the singlet pair density is lower when the singlet annihilation rate is faster. This behavior becomes opposite when the triplet generation rate is low, as it is the case for the examples treated in Fig. 3.2 (c). These differences between the two pair densities disappear when k_{ISC} becomes larger as for the examples presented in Fig. 3.2 (a) and (c), because k_{ISC} tends to equalize both densities. Note that the steady state behavior is quite similar with the cw case discussed in the previous chapter. However, when the thermal distribution of singlet and triplet densities are not symmetric, k_{ISC} increases the differences between the two pair densities because intersystem-crossing does not simply equalize densities of states but it drives the system towards the thermal equilibrium as one can see from a comparison of Fig. 3.2 (a) and (c) with Fig. 3.2 (b) and (d).

It must be noted that the steady-state values for spin-dependent recombination discussed above may only be of limited use for the interpretation of experimental data since spin-dependent currents in most materials are superimposed by spin-independent offset currents, which become indistinguishable from the spin-dependent currents when the latter remain in the steady state. This problem actually is the reason why pEDMR and pODMR experiments are performed. By selectively bringing the spin-dependent processes into a nonsteady state, spin-dependent and spin-independent processes become distinguishable. Note however, that

while the steady state solutions given above are of limited use for the interpretation of experimental data, they are necessary for finding general solutions for the transient behavior.

3.2.1.2 Boundary conditions and solutions

In order to find the transient solutions for the permutation symmetry densities, we need to consider next the boundary conditions of the given system of differential equations: First, at t=0, $n_{sp}(0) = A_{1p} + A_{2p} + n^0_{s2}$ and $n_{tp}(0) = B_{1p} + B_{2p} + n^0_{t2}$. If we define Δn as the change in the singlet density induced by the resonant pulse, then we obtain $\Delta n \equiv n_s(0) - n^0_s = -(n_t(0) - n^0_t)$. Thus $A_{2p} = \Delta n - A_{1p}$ and $B_{2p} = -(\Delta n + B_{1p})$. This boundary condition is still not enough to find the solutions for the four unknown coefficients, A_{1p}, A_{2p}, B_{1p}, B_{2p}.

Similarly as in Chapter 2.1.2, singlet and triplet pair densities experience pair generation, annihilation through recombination and dissociation, and spin mixing due to intersystem-crossing and the external magnetic resonance field. As mentioned above, for the pulsed experiment, we are interested only in the propagation after a short resonant resonance pulse. Thus both densities don't experience spin mixing due to external excitation, and both densities relax back to the steady state value as long as the repetition time is sufficiently long. Changes of the pair densities introduced by the pulse can be obtained by integration of the rate equations 3.1 and 3.2 which yields

$$n_{sp}(\infty) - n_{sp}(0) = \int_0^\infty (G_s - C_s n_s - k_{ISC}(n_s - \rho n_s) + k_{ISC}(n_t - (1-\rho)n_t))dt, \quad (3.5)$$

$$n_{tp}(\infty) - n_{tp}(0) = \int_0^\infty (G_t - C_t n_t - k_{ISC}(n_t - (1-\rho)n_t) + k_{ISC}(n_s - \rho n_s))dt. \quad (3.6)$$

In these expressions, "0" denotes the time right after the pulse. Before solving these terms, we can simplify by plugging eqs. 3.3 and 3.4 into the integrals, which leads to

$$\begin{aligned} n^0_{sp} - n_{sp}(0) = \int_0^\infty ((-(C_s + w_{12})A_{1p} + w_{22}B_{1p})e^{(-m_{12}t)} \\ +(-(C_s + w_{12})(\Delta n - A_{1p}) - w_{22}(\Delta n + B_{1p})e^{(-m_{22}t)})dt, \end{aligned} \quad (3.7)$$

$$\begin{aligned} n^0_{tp} - n_{tp}(0) = \int_0^\infty ((-(C_t + w_{22})B_{1p} + w_{12}A_{1p})e^{(-m_{12}t)} \\ +((C_t + w_{22})(\Delta n + B_{1p}) + w_{12}(\Delta n - A_{1p})e^{(-m_{22}t)})dt. \end{aligned} \quad (3.8)$$

Note that we use here that $G_s = (C_s + w_{12})n^0_s - w_{22}n^0_t$ and $G_t = (C_t + w_{22})n^0_s - w_{12}n^0_s$. Again, solving the resulting two equations reveals

$$-\Delta n = -\frac{C_s + w_{12}}{m_{11}}A_{1p} + \frac{w_{22}}{m_{11}}B_{1p} - \frac{C_s + w_{12}}{m_{21}}(\Delta n - A_{1p}) - \frac{w_{22}}{m_{21}}(\Delta n + B_{1p}), \quad (3.9)$$

$$\Delta n = -\frac{C_t + w_{22}}{m_{11}} B_{1p} + \frac{w_{12}}{m_{11}} A_{1p} + \frac{C_t + w_{22}}{m_{21}} (\Delta n + B_{1p}) + \frac{w_{12}}{m_{21}} (\Delta n - A_{1p}). \tag{3.10}$$

Finally by resolving these equations for the wanted prefactors of our exponential transients, we obtain

$$\begin{aligned} A_{1p} &= -\frac{(C_s + w_{12})(C_t + w_{22}) - w_{12}w_{22} - C_t m_{22}}{(C_s + w_{12})(C_t + w_{22}) - w_{12}w_{22}} \cdot \frac{m_{12}}{m_{22} - m_{12}} \cdot \Delta n \\ &= -\frac{m_{12} - C_t}{m_{22} - m_{12}} \Delta n, \end{aligned} \tag{3.11}$$

$$\begin{aligned} B_{1p} &= \frac{(C_s + w_{12})(C_t + w_{22}) - w_{12}w_{22} - C_s m_{22}}{(C_s + w_{12})(C_t + w_{22}) - w_{12}w_{22}} \cdot \frac{m_{12}}{m_{22} - m_{12}} \cdot \Delta n \\ &= \frac{m_{12} - C_s}{m_{22} - m_{12}} \Delta n. \end{aligned} \tag{3.12}$$

Note that the parameter Δn in these equations represents the amount of singlet density that is transformed into the triplet density during the pulsed excitation. It is therefore determined by the coherent spin motion during the brief coherent excitation pulse. Note that Δn does not affect the time dependence itself because is a common scaling factor in all coefficients that determine the exponential decay transients.

3.2.2 The transient behavior of the pEDMR and pODMR observables

In this section, the time-dependent behavior of observables after perturbation of the singlet and triplet pair densities induced by a resonant pulse will be explored by using the solutions obtained in previous section. The transients of pEDMR and pODMR signals are determined decided by two sets of important parameters: Two decay rates, m_{12} and m_{22} (the inverse of the decay constants), and the two coefficients, A_{1p} and B_{1p}. We consider the nature of the two decay constants first.

3.2.2.1 Characteristics of the biexponential decay

The two biexponential decay constants, m_{12} and m_{22}, are determined by the recombination, dissociation, and intersystem-crossing rate coefficients, which all compete with each other. According to eqs. 3.1 and 3.2, it is clear that these constants depend only on their respective spin-pair annihilation process as long as intersystem-crossing is weak. Thus, singlet and triplet rates become mutually independent and they will decay with $C_s = d_s + r_s$ and $C_t = d_t + r_t$, respectively. When intersystem-crossing becomes significant ($k_{ISC} \neq 0$), a more complicated scenario evolves. For large k_{ISC}, one of the decay constants will asymptotically approach k_{ISC}, while the other decay constant will approach $(1-\rho)C_s + \rho C_t$. These behaviors are summarized in Table 3.2.

Fig. 3.3 shows plots of the two exponential decay rates as a function of k_{ISC} for two different values of ρ. Note that the displayed functions are independent of the generation rates. When $k_{ISC} \to \infty$, m_{22} approaches k_{ISC}. This means that $m_{22} > k_{ISC}$ always holds true for any value of k_{ISC}. Thus, $T_{ISC} > 1/m_{22}$. This is an important insight because it implies that as long as a biexponential decay is detectable in a pEDMR or pODMR experiment and both exponential functions belong to the same spin-dependent process (this can be verified by lineshape comparison), a lower limit for intersystem-crossing times is given by the decay constant of the the faster decaying exponential function. It should be noted that $m_{22} > k_{ISC}$ is also true for the cw case (eqs. 2.13 and 2.16). And because the lower limit of T_{ISC} is decided by only m_{22}, which is also the faster time constant of a double exponential response of cwODMR and EDMR in the cycle where the pulse is off, the same interpretation is possible for the cwODMR and EDMR data measured in time-domain.

3.2.2.2 Modeling observable

There are various qualitatively different classes of spin-dependent mechanism which influence conductivity. Examples are spin-dependent trapping [31], spin-dependent scattering [32], spin-dependent transport through localized states [33] and spin-dependent recombination [34, 35]. The most widely studied class of spin-dependent mechanisms are transport and recombination processes through weakly coupled intermediate pair systems. Spin-dependent recombination can be found in many semiconductors including silicon [15, 21, 34] and some organic materials [2, 3, 18, 36, 37]. Similar as for the discussion of cwEDMR and cwODMR in the last chapter, we can describe conductivity as a superposition

$$\sigma = \sigma_0 + \sigma_s + \sigma_t, \tag{3.13}$$

of spin-independent conductivity σ_0 and spin-dependent conductivity from the singlet pairs σ_s and triplet pairs σ_t, respectively. The singlet and triplet conductivities are given by

$$\sigma_s(t) = (\mu_e + \mu_h) e \tau d_s n_{sp}(t), \tag{3.14}$$

$$\sigma_t(t) = (\mu_e + \mu_h) e \tau d_t n_{tp}(t), \tag{3.15}$$

where μ_e and μ_h are the mobilities of electrons and holes respectively, e is the elementary charge, and τ is the free charge carrier life time. The above equations illustrate that the spin-dependent conductivity is dependent on the spin-pair dissociation rate. The conductivity change due to spin-dependent recombination depends solely on $\sigma_s(t) + \sigma_t(t)$ and thus, the transient change of conductivity is

$$\begin{aligned}
\Delta\sigma(t) &= \sigma - \sigma_0 \\
&= \mu e\tau(d_s n_{sp}(t) + d_t n_{tp}(t)) \\
&= \mu e\tau(d_s(A_{1p}e^{-m_{12}t} + (\Delta n - A_{1p})e^{-m_{22}t}) + d_t(B_{1p}e^{-m_{12}t} - (\Delta n + B_{1p})e^{-m_{22}t})) \\
&= \mu e\tau\{(d_s A_{1p} + d_t B_{1p})e^{-m_{12}t} + [d_s(\Delta n - A_{1p}) - d_t(\Delta n + B_{1p})]e^{-m_{22}t}\} \\
&= \mu e\tau\{\sigma_1 e^{-m_{12}t} + \sigma_2 e^{-m_{22}t}\}. \qquad (3.16)
\end{aligned}$$

For simplicity, $\mu_e + \mu_h$ is replaced here by $\mu = \mu_e + \mu_h$, while $\sigma_1 = d_s A_{1p} + d_t B_{1p}$ and $\sigma_2 = d_s(\Delta n - A_{1p}) + d_t(\Delta n + B_{1p})$. Similar as to cwODMR transients discussed in the last chapter, it is clear that pEDMR transients follow a double exponential behavior. Note again that the above expression for the transient conductivity change is pair-generation rate independent as long as the induced conductivity changes are small. Whether the transient in eq. 3.16 causes an initial enhancement or quenching can be inferred from

$$\Delta\sigma(0) = \mu e\tau\Delta n(d_s - d_t) \qquad (3.17)$$

whose sign is determined only by Δn and $d_s - d_t$.

The magnitudes and the time constants of the two exponential decay functions provide further insights into the nature of the observed spin pair system. The constants σ_1 and σ_2 depend on all rate coefficients but not the generation rate. If the signs of σ_1 and σ_2 are opposite, the observed biexponential decay transient shows quenching-enhancement or enhancement-quenching behavior. We consider two limits of k_{ISC} based on the asymptotic values of the two coefficients, A_{1p} and B_{1p}, which are summarized in Table 3.3.

Using these limiting values we obtain a conductivity transient

$$\Delta\sigma(t) = \mu e\tau\Delta n(d_s e^{-C_t t} - d_t e^{-C_s t}) \qquad (3.18)$$

for $k_{ISC} \to 0$ and

$$\Delta\sigma(t) = \mu e\tau\Delta n(d_s e^{-k_{ISC}t} - d_t e^{-((1-\rho)C_s + \rho C_t)t}) \qquad (3.19)$$

for $k_{ISC} \to \infty$. The transients for both extremal cases show enhancement-quenching or quenching-enhancement because of the negative sign before the second term. Whether for any transient the enhancement or the quenching comes first depends on the sign of Δn and while for both cases, the signal intensities are equal, the first term decays very quickly for $k_{ISC} \to \infty$.

Similarly as for pEDMR, we obtain for pODMR, an expression

$$I = I_0 + I_s + I_t \tag{3.20}$$

for the transient of the total luminescence intensity. Here I_0 is the intensity of spin-independent luminescence, while

$$I_s(t) = r_s n_{sp}(t), \tag{3.21}$$

$$I_t(t) = r_t n_{tp}(t), \tag{3.22}$$

are the intensities of singlet and triplet pair recombination respectively. The transient of the luminescence change therefore becomes

$$\begin{aligned}
\Delta I(t) &= I(t) - I_0 \\
&= (r_s n_{sp}(t) + r_t n_{tp}(t)) \\
&= (r_s(A_{1p}e^{-m_{12}t} + (\Delta n - A_{1p})e^{-m_{22}t}) + r_t(B_{1p}e^{-m_{12}t} - (\Delta n + B_{1p})e^{-m_{22}t})) \\
&= (r_s A_{1p} + r_t B_{1p})e^{-m_{12}t} + [r_s(\Delta n - A_{1p}) - r_t(\Delta n + B_{1p})]e^{-m_{22}t} \\
&= I_1 e^{-m_{12}t} + I_2 e^{-m_{22}t}
\end{aligned} \tag{3.23}$$

Again, we can find the transient solutions of pODMR

$$\Delta I(t) = \Delta n(r_s e^{-C_t t} - r_t e^{-C_s t}) \tag{3.24}$$

for $k_{ISC} \to 0$ and

$$\Delta I(t) = \Delta n(r_s e^{-k_{ISC}t} - r_t e^{-((1-\rho)C_s + \rho C_t)t}) \tag{3.25}$$

for $k_{ISC} \to \infty$. And at t=0,

$$\Delta I(0) = \Delta n(r_s - r_t). \tag{3.26}$$

The considerations made above illustrate that the same arguments apply to pODMR and pEDMR rate transients except that the recombination rate coefficients, r_s and r_t, replace the dissociation rate coefficients in pODMR description made above. Fig. 3.4 shows plots of the coefficients, A_{1p} and B_{1p}, as well as the magnitudes I_1 and I_2 (see Table 3.4) of the two exponential decays as functions of k_{ISC}. A_{1p} shows an extremum at

$$k_{ISC} = C_s - C_t. \tag{3.27}$$

Similarly both I_1 and I_2 show extrema at

$$k_{ISC} = -\frac{r_t(1-\rho) - r_s\rho}{r_t(1-\rho) + r_s\rho}(C_s - C_t). \tag{3.28}$$

While A_{1p} and B_{1p} can not be measured with real pODMR experiments, I_1 and I_2 can be measured even though this is difficult since both dependent on Δn. However, the ratio

between I_1 and I_2 can be determined exactly from experimental data. Fig. 3.4 (c) shows $-I_2/I_1$ as a function of k_{ISC}. This curve converges to r_s/r_t for small k_{ISC} and diverges to $k_{ISC}\frac{r_s-r_t}{((1-\rho)r_s+\rho r_t)(C_s-C_t)}$ for large k_{ISC}. Again, these insights into the nature of pODMR transients are equally applicable to pEDMR transients as long as r_s and r_t are replaced by d_s and d_t.

In conclusion, the transient behavior of pODMR and pEDMR signals caused by spin-dependent intermediate pair processes has been explained. It was found that these transients always follow a biexponential decay behavior where both exponential functions exhibit opposite signs. Limits for large and small intersystem-crossing rates k_{ISC} have been discussed. For slow intersystem-crossing, the slower exponential decay component is small while the faster component is determined by electronic transition rate coefficients. When the intersystem-crossing process is very fast, only the fast exponential decay will be determined by the intersystem-crossing-rate, so that the slower component remains slow. For the illustration of this behavior, a plot of pODMR transients (the relative PL change as a function of time after a pulsed resonant spin excitation) as a function of the intersystem-crossing rate k_{ISC} is shown in Fig. 3.5.

Even though the dynamics of pEDMR and ODMR is rather simple compared with cwEDMR and ODMR (compare eqs. 2.31 and 2.30 with eqs. 3.11 and 3.12), interpretation of pEDMR and ODMR still has an ambiguity: equations 3.17 and 3.26 explain that it is difficult to figure out what spin-dependent transition is dominant only from a single time transient measurement of pEDMR and ODMR. This is because the sign of the transient signal is determined by not only two transition rate coefficients but also Δn which cannot be determined from a transient measurement. This means than even if $r_s > r_t$ is true for example, a transient of pODMR can show quenching-enhancement behavior if Δn is negative. Thus it is still difficult to obtain the exact information about the spin-dependent transition processes in a tested sample by only doing a single transient experiment of either pEDMR and ODMR. If one can conduct both pEDMR and ODMR at the same condition and only if both electrically and optically detected dynamics are identical, four equations for m_{12}, m_{22}, I_1/I_2, and σ_1/σ_2 can be obtained. Then, because the lower limit of T_{ISC} can be obtained from m_{22}, estimation for all rate parameters including r_s, r_t, d_s, and d_t is possible. This estimation can become more accurate if T_{ISC} is determined by a coherent experiment such as spin Hahn-echo experiment.

3.3 Coherent pEDMR and pODMR

After more than three decades of pODMR spectroscopy and more than one decade of pEDMR spectroscopy, a broad range of pEDMR and pODMR pulse sequences is available today allowing the measurement of a broad range of information such as electronic and spin relaxation times, coupling strengths and hyperfine parameters. The most simple pEDMR and pODMR experiment is the electrical and optical detection of spin-Rabi nutation which is conducted by application of a single ESR pulse [2–4, 18, 22, 24, 25, 28, 29, 38, 39]. Rabi nutation of electron spins can also be detected via electron-electron double resonance (ELDOR) [40] and electron nuclear double resonance(ENDOR) [41, 42]. Electrical detection of nuclear spin oscillations has been achieved recently, an important breakthrough for the development of electrical nuclear spin-quantum readout devices [43, 44]. Furthermore, electrically detected spin Hahn-echoes [21], inversion recovery [31], Carr-Purcell [45] and Carr-Purcell-Meiboom-Gill [46] pulse sequences have been demonstrated. Electrical detection of electron-spin-echo envelope modulation (ESEEM) has been done to sensitively study the $Si\backslash SiO_2$ interface defect states in phosphorus-doped crystalline silicon [43]. Rotary echoes also have been detected both electrically [47] and optically [27].

Electron spin resonance occurs when a spin-induced magnetic moment $\mu_B g\vec{S}$ is exposed to a circularly polarized electromagnetic radiation with field strength B_1 while this field has a frequency ω that is equal to the Larmor frequency ω_L at which the spin precesses due to the presence of an additional constant magnetic field B_0. Note that for magnetic resonance to occur, the circularly polarized microwave field must be perpendicular to the direction of the B_0 field. From the viewpoint of a reference frame which rotates with frequency ω around the direction of B_0 (the so called rotating frame), the electromagnetic field appears like a constant magnetic field. Under spin resonance, the spin is at rest in the rotating frame, too and thus, the B_0 field is not present. Consequently, magnetic resonance can be described as a spin-precession around the B_1 field. In the laboratory frame, this propagation is perceived as a flip of the spin from one direction parallel to B_0 (down) into the opposite direction (up). Spin-flips between up- and down and vice versa will repeatedly occur for as long as a spin is in magnetic resonance. This periodic flipping is called a Rabi-oscillation. When the resonance condition is not perfectly satisfied, $\omega \neq \omega_L$ an additional magnetic field ΔB_0 appears perpendicular to B_1 in the rotating frame. Due to this additional field, the rotation axis for the spin precession becomes slightly tilted and thus, the spin flip does not encompass a full 180 range. Hence, off- magnetic resonance, spins can not be flipped as efficiently, and when $\omega - \omega_L$ becomes large, not at all. Rabi oscillation does not happen

anymore under such conditions. This principle of magnetic resonance is explained in great detail in book by Atherton for electron spins [48] or Slichter for nuclear spins [49].

For the description of EDMR and ODMR experiments, the description of magnetic resonance must be combined with the spin-pair model which has been discussed in detail above. As permutation symmetry governs the observables, the mutual orientation between two spins becomes important. For example, when two weakly coupled spins with $s = 1/2$ are aligned parallel, they occupy a triplet-state and the probability for the transition to a singlet state is zero (when spin-orbit coupling is weak), but it becomes $1/2$ when they are antiparallel. Thus, exposing one of the two spins to magnetic resonance varies the transition probability and observables like recombination current, photoluminescence, etc. reflect this change of the spin-pair state. When a continuous Rabi oscillation is induced on a short time scale, one can observe a harmonically oscillating current or luminescence rate. The frequencies of these oscillations depend on the microscopic magnetic environment the neighboring electron spins. For example, exchange interaction or nuclear spins in proximity of the electron spin pair can drastically affect how spin-Rabi oscillation (or any other coherent spin propagation) takes place and the measurement of this effect will therefore reveal information about the microscopic nature of the given pair system. In the following, it is discussed how electrical and optical detection of spin Rabi nutation differs from the observation of spin-Rabi oscillation with conventional ESR (an experiment which is called transient nutation) and it is discussed what information can be obtained from the electrical or optical detection of these effects.

3.3.1 Hamiltonian of spin pairs

The most straightforward approach for the description of coherent spin-motion during pEDMR or pODMR experiments is to consider the Hamiltonian of those systems which are involved in spin-dependent processes. Similar as for the previous chapters, we consider intermediate pairs of two electron spin. In the presence of a static magnetic field, B_0, the Hamiltonian $\hat{H}_0$ is given by

$$\hat{H}_0 = g_a \mu_B \hat{\mathbf{S}}_\mathbf{a} + g_b \mu_B \hat{\mathbf{S}}_\mathbf{b} + J \hat{\mathbf{S}}_a \cdot \hat{\mathbf{S}}_b + \hat{\mathbf{S}}_a \cdot \mathbf{D} \cdot \hat{\mathbf{S}}_b. \tag{3.29}$$

The first two terms explain the Zeeman interaction of each spin pair partners, with g_a and g_a being the Landé g-factors of the pair partners a and b and μ_B being the Bohr magneton. The third and forth terms explain exchange interaction with coupling constant J and dipolar interaction with the dipolar spin-spin coupling tensor, $\mathbf{D}$, respectively. When the magnetic resonant radiation is turned on, a time-dependent Hamiltonian

$$\hat{H}_1 = g_a \mu_B \hat{\mathbf{S}}_a \cdot \hat{\mathbf{B}}_1 + g_b \mu_B \hat{\mathbf{S}}_b \cdot \hat{\mathbf{B}}_1 \tag{3.30}$$

has to be added to $\hat{H}_0$ in which $B_1 = \hat{\mathbf{x}} B_1 e^{-i\omega t}$. If ensembles of identical spin pairs are present, the time-dependent Liouville $\hat{\rho}(t)$ operator must be used to described the ensemble propagation. Solutions for $\hat{\rho}(t)$ can be found by solving the Louville equation. In the following, the work that has been conducted in the past decade in order to finding adequate descriptions of pEDMR experiments is summarized in the following.

3.3.2 Electrically and optically detected spin Rabi osciallltion

In this section, we will consider spin-dependent rates, $R(t)$, based on spin $s = 1/2$ pairs, which have been discussed extensively in the pEDMR and pODMR literature [18, 20, 21]. As pointed out by Boehme and Lips [1], $R(t)$ should be the summation of both singlet and triplet recombination as below,

$$R(t) = r_s \mathrm{Tr}[|S\rangle\langle S|\hat{\rho}(t)] + r_t \sum_{i=-1}^{1} \mathrm{Tr}[|T_i\rangle\langle T_i|\hat{\rho}(t)] \tag{3.31}$$

where r_s and r_t are singlet and triplet recombination probabilities respectively. The time-dependent solutions for the density operator $\rho(t)$ can be found by solving a stochastic Louville equation given by

$$\frac{\partial \hat{\rho}}{\partial t} = \frac{i}{\hbar}[\hat{\rho}, \hat{H}] + \mathfrak{S}[\hat{\rho}] + \mathcal{R}\{\hat{\rho} - \hat{\rho}_0\}. \tag{3.32}$$

The commutator in the first term of this equation describes the ensemble dynamics that is determined by $\hat{H}_0 + \hat{H}_1$. The second and third terms describe spontaneous changes of the ensemble due to random spin-pair annihilation (e.g., recombination) and generation as well as spin-relaxation. If we consider the spin-pair dynamics on time scales faster than any spontaneous transitions when the resonance microwave pulse is being applied, only the first term needs to be solved. For weak coupling, when J and $\mathbf{D}$ are small, the can described by the unitary rotation transformations. Boehme and Lips have used this method and found the relative density changes of weakly coupled spin pairs for a variety of situations determined by Larmor separation and electromagnetic radiation strength [1]. First, when the Larmor separation is larger than the given radiation field strength, the relative density change $\Delta(\tau)$ of weakly coupled spins becomes

$$\Delta(\tau) = \frac{\gamma_i^2 B_1^2}{2\Omega_i^2}[1 - cos(\Omega_i \tau)] \qquad (\text{for } |\omega_a - \omega_b| \gg \gamma B_1) \tag{3.33}$$

where ω_a and ω_b are the Larmor frequencies of each pair partners, γ is the electron gyromagnetic ratio, and Ω_i is the Rabi oscillation frequency of one of pair partners given by

$\sqrt{\gamma_i^2 B_1^2 + (\omega - \omega_i^2)}$. When the resonant condition is exactly satisfied, $\Omega_i = \gamma_i B_1$. When the Larmor separation is smaller, ω_a and ω_b can be considered to be the same, $\omega_a \simeq \omega_b \equiv \omega_L$, so that $\Omega_a = \Omega_b = \Omega = \sqrt{\gamma^2 B_1^2 + (\omega - \omega_L^2)}$. In addition, if the measurement is done around the resonant frequency ($\omega - \omega_L \ll \gamma B_1$), the relative density change becomes

$$\Delta(\tau) = \frac{\gamma^2 B_1^2}{2\Omega^2}[1 - cos(2\Omega\tau)] \qquad (\text{for } |\omega_a - \omega_b| \ll \gamma B_1). \tag{3.34}$$

This result shows that the oscillating frequency is doubled when a weakly coupled spin pair is excited by very strong resonant radiation. The doubling of the measured precessiong frequency is due to a beating effect of the two spin Rabi oscillations. The above results are only valid for weakly coupled spins where $D + J \ll \omega_{a,b}$. If g-factor inhomogeneities are taken into account, the effective relative density change becomes

$$\Delta^{\text{eff}}(\tau) = \int_{-\infty}^{\infty} \Phi(\omega_L) \frac{\gamma^2 B_1^2}{\gamma^2 B_1^2 + (\omega - \omega_L)^2} \sin^2(\kappa\tau\sqrt{\gamma^2 B_1^2 + (\omega - \omega_L)^2}) d\omega_L \tag{3.35}$$

where τ is the length of the resonant pulse radiation, κ becomes 1/2 for large Larmor separation and 1 for small larmor separation, and $\Phi(\omega_L)$ represents the Landé g-factor distribution. Aside from the distribution function and sinusoidal function, there is another term, $\gamma^2 B_1^2/(\gamma^2 B_1^2 + (\omega - \omega_L)^2)$ in this expression, which described the Lorentzian line-shape of the pEDMR or pODMR signal due to power broadening. According to Levitt [50], this line-shape can also be derived from the off resonance-pulse propagator for a single spin when a π-pulse is applied along the +x-axis, which then becomes

$$\hat{R}_{off} = \hat{R}_z(0)\hat{R}_y(\theta)\hat{R}_z(\pi)\hat{R}_y(-\theta)\hat{R}_z(0) \tag{3.36}$$

where $\hat{R}$ represents a rotation operator, and $\theta = arctan(\frac{\gamma B_1}{\omega - \omega_L})$. Then, the transition probability for a spin from spin-up state to spin-down state can be obtained by

$$P_{\uparrow\to\downarrow} \quad = \quad |\langle\downarrow|\hat{R}_{off}(\omega - \omega_L)|\uparrow\rangle|^2 \tag{3.37}$$

which becomes exactly the Lorentzian function, $\gamma^2 B_1^2/(\gamma^2 B_1^2 + (\omega - \omega_L)^2)$.

3.3.3 Effects of inhomogeneous broadening

Equation 3.35 explains the spin-Rabi nutation transient in presence of inhomogeneous broadening. Fig. 3.6 (a) and (b) show the Fourier transformation of simulated $\Delta(\tau)$ as a function of the excitation frequency as obtained from eq. 3.35. Note that the pulse length dependencies are obtained first from eq. 3.35 then converted into the frequency domain by fast Fourier transformation. When the spin ensemble is not significantly influenced by inhomogeneity, one can easily find that the dominant frequency components are described by the

hyperbola $\sqrt{\gamma^2 B_1^2 + (\omega - \omega_L^2)}$ as shown Fig. 3.6(a). However when strong inhomogeneous broadening is assumed (that means the width of the distribution is larger than γB_1), the signals around $\Omega = \gamma B_1$ smear out and the hyperbolic patterns cannot be found anymore. Instead off-resonant components appear around $\Omega = \gamma B_1$ and signals at the distribution tails also can be found. Note that the data in Fig. 3.6 were obtained using eq. 3.35. It is in excellent agreement with data obtained from numerical solutions [29] using the Liouville equation. In contrast to numerical data, analytical expression (as given in eq. 3.35) can be utilized for the analysis of the experimental data. This will be used in Chapter 5. In the following it is discussed how this function is used to for the analysis of experimental data.

3.3.4 Method to analyze band-limited spin-Rabi nutations

When the expression in eq. 3.35 is used to fit experimental data, coherence decay as well as the Nyquist effect must be taken into acocunt: Experimental data are always recorded at a finite sampling rate. Fig. 3.7 (a) displays plots of three calculated Rabi nutations in time domain. The Black curve is obtained from a sinusoidal function (see eq. 3.33) with a finite sampling rate of 0.1ns and a maximum excitation pulse length of 511.9 ns. The Fourier transformation of this data has a finite frequency resolution of 1.953 MHz determined by the longest pulse length, and a finite spectral width as determined by the sampling rate. The Fourier transformed curve appears as a black curve in Fig. 3.7 (b). Note that this data represents spins which are not influenced by any kind of inhomogeneous broadening. From the black curve in Fig. 3.7 (b), one can easily pick up the peak intensity and the Rabi frequency. For realistic experimental situations, spin ensembles are usually under the influence of large inhomogeneous broadening and sometimes, exposed to the influence of short coherence times. Both of these effects lead to a fast decay of the observed Rabi oscillation, and when the maximum pulse length of detectable Rabi oscillation is shortened, the frequency resolution of the Fourier transform increases. A simulation of this situation is represented by the red curves in Fig. 3.7 (a) and (b). These data have been obtained from eq. 3.35 combined with the same sampling rate as the black curve. The effect of this shortening of the Rabi oscillation measurement leads to a broadening of the frequency resolution to 3.906 MHz. Note that Fig. 3.7 (b) shows that one can still find the experimentally obtained spin Rabi nutation peak, which, due to the introduced changes shows longer tails in both the high- and the-low frequency range. The broadening of the frequency distribution can be quite substantial since the Fourier transformed functions are not of Gaussian or Lorentzian nature but Fourier transforms of modified Bessel functions.

This effect can lead to significant overlap between two nutation signals and because of this, fits of experimental Rabi oscillation data with frequencies, intensities, width etc. is best done by the exact function given by eq. 3.35 [38]. For this procedure one needs to first determine the g-factor distribution from the B_0-dependence of the observed Rabi oscillation data and then fit the Rabi oscillation peaks with analytical functions given by eq. 3.33. Another problem associated with the fit of Rabi-nutation data is the oftentimes limited-sampling rate of experiments. The blue curves in Fig. 3.7 illustrate this problem: Using from eq. 3.35, the same data as discussed above were calculated, yet only at 4 ns sampling rate. One can quickly notice that in the Fourier transformation of these data, offsets appear over a very broad frequency range which even make it more difficult to fit when more than one nutation signal is present. Furthermore, due to the reduced sampling rate, a decrease of detection bandwidth can be noticed, too. According the sampling theorem (or Nyquist theorem) [51], the sampling rate should be faster than the Nyquist rate which is double the highest frequency of a nonzero signal or the original signal cannot be reconstructed perfectly. It means that if the sampling rate is not fast enough, then the main frequency component of the Rabi nutation cannot be detected.

Both the influences of the finite sampling rate as well as the finite detection length of Rabi oscillastion must be taken into account when experimental data is analyzed. To do this, one should carry out fits with calculated numerical obtained from a convolution of eq. 3.35 with the sampling functions as well as the available frequency resolution. The technical aspects of this procedure will be discussed more in detail in Chapter 5.

3.4 Summary

A rate model has been developed to describe the transient responses of spin-dependent charge carrier pair transition rates on long (incoherent) time scales after a magnetic resonant excitation. The calculations show that independent of the rate of intersystem-crossing between the singlet and triplet pairs, the transient response exhibits a double exponential decay behavior that had already been known from systems without intersystem-crossing [18, 30]. It has also been found that the faster of two time constants of the biexponential decay is always faster than the intersystem-crossing rate. This realization provides a very simple and straightforward method to find a lower limit on the intersystem-crossing time which has been applied to the interpretation of experimental results as shown in the following chapters.

For the description of spin-dependent recombination rates on coherent time scales, the

existing literature has been discussed and an analytical function which can explain Rabi nutation of spin ensembles under the influence of strong inhomogeneous broadening was given. Furthermore, a data analysis procedure for electrically and optically detected Rabi oscillation was outlined which addresses the proper handling of coherence decay effects and Nyquist effects on the experimental data during the fit procedures. For the fit of Rabi oscillation data, eq. 3.35 should be used under consideration of experimental band-width limitations and the given experimental sampling rate.

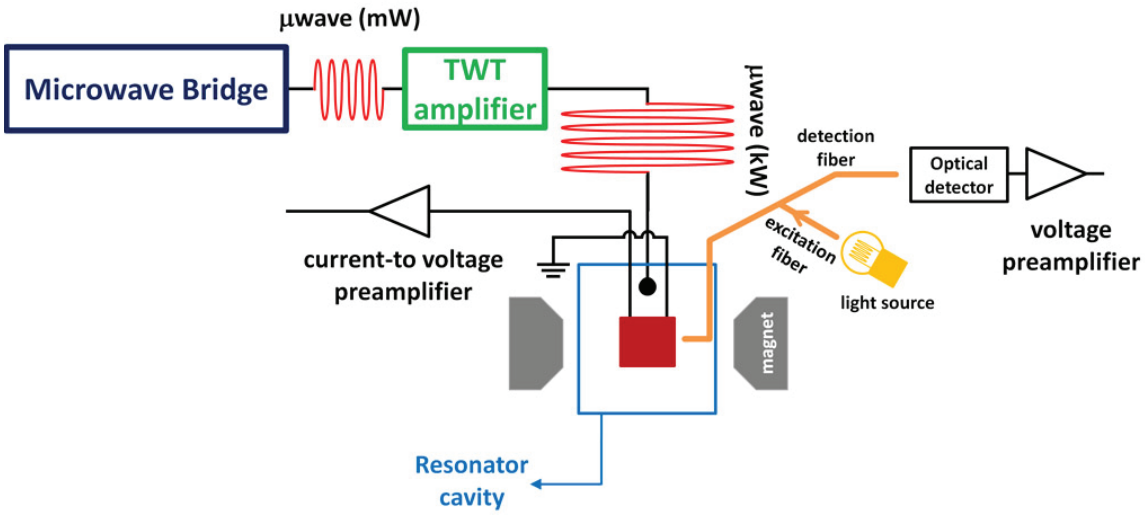

Figure 3.1. Experimental setup for the pEDMR and ODMR. An optics setup for the PL detection and an electrical setup for the photocurrent detection are shown as examples.

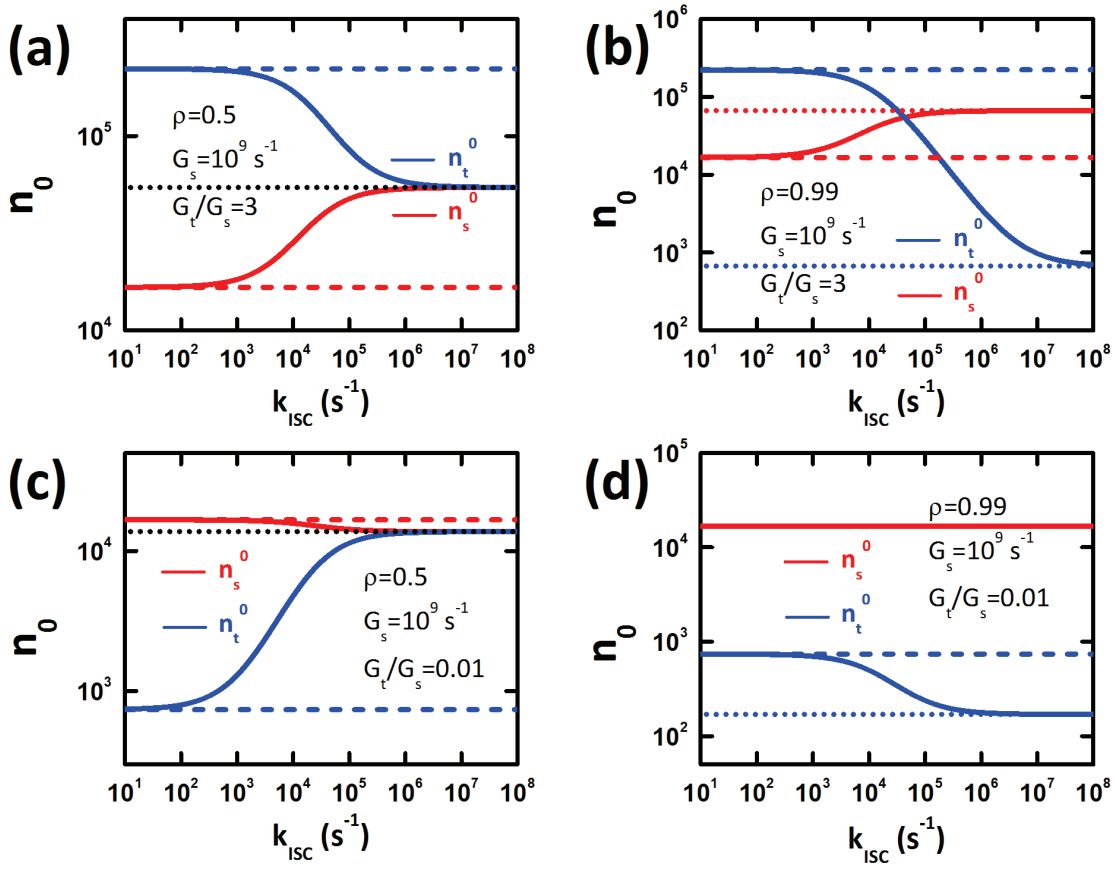

Figure 3.2. Plots of the steady-state pair densities, n_s^0 and n_s^0 as a function of k_{ISC}. Each pot shows different quantitative models: (a) $\rho = 0.5$, $G_s = 10^9 s^{-1}$, $G_t = 3 \times G_s$, (b) $\rho = 0.99$, $G_s = 10^9 s^{-1}$, $G_t = 3 \times G_s$, (c) $\rho = 0.5$, $G_s = 10^9 s^{-1}$, $G_t = G_s/100$, (d) $\rho = 0.99$, $G_s = 10^9 s^{-1}$, $G_t = G_s/100$. Parameters used identically for all simulations are $r_s = 2 \times 10^4$, $r_t = 2 \times 10^2$, $d_s = 4 \times 10^4$, $d_t = 4/3 \times 10^4$. For details see text.

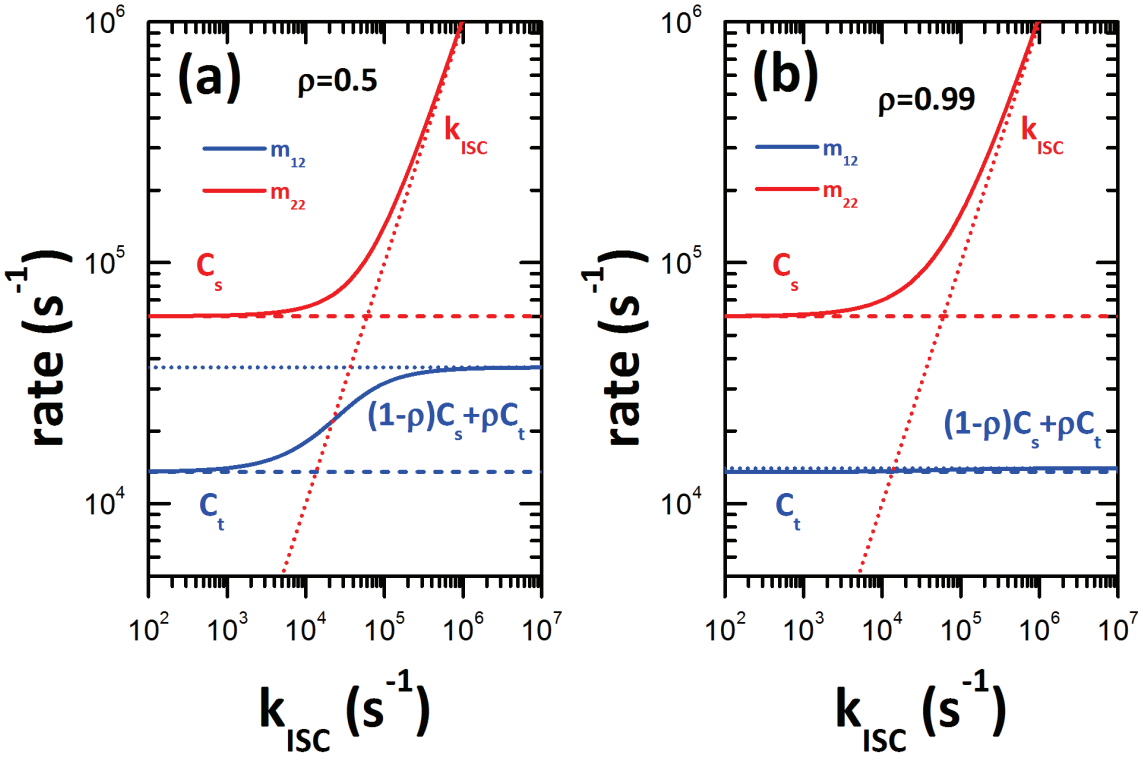

Figure 3.3. Plot of two cwEDMR and ce ODMR decay rates, m_{12} and m_{22}, as a function of intersystem-crossing rate for two different temperatures (a) $\rho = 0.5$ and (b) $\rho = 0.99$. The parameters used identically for both simulations are $r_s = 2 \times 10^4$, $r_t = 2 \times 10^2$, $d_s = 4 \times 10^4$, $d_t = 4/3 \times 10^4$, $G_s = 10^9$, $G_t = G_s/100$.

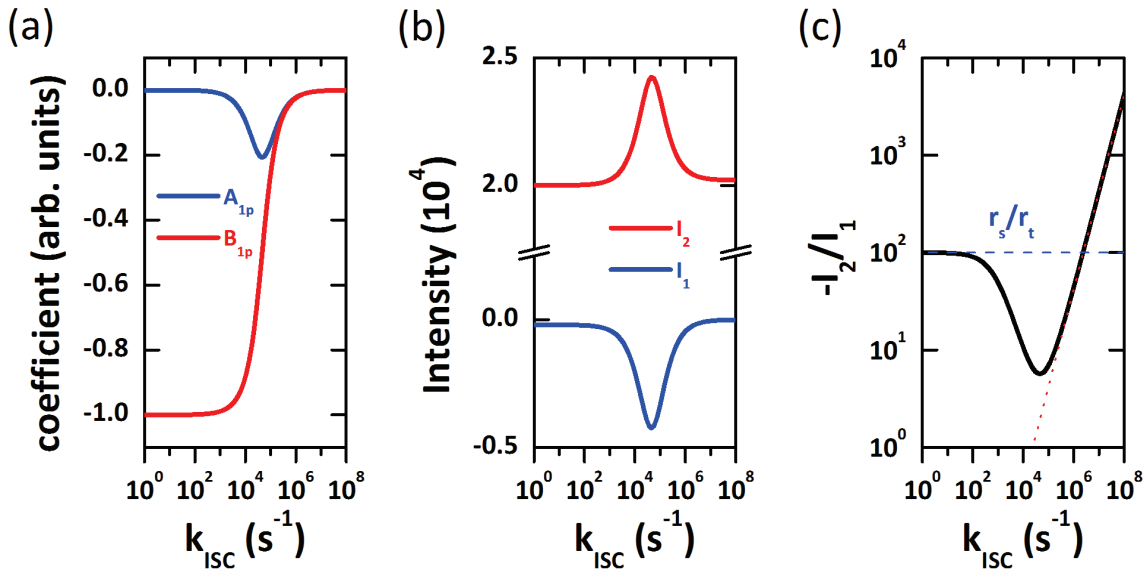

Figure 3.4. k_{ISC} dependencies of the coefficients of the double exponential transient functions. (a) Plots of the coefficients A_{1p} and B_{1p} as defined by eqs. 3.11 and 3.12 as a function of k_{ISC}. (b) Plots of the coefficients I_1 and I_2 as defined by eq. 3.23 as a function of k_{ISC}. (c) Plot of the ratio of $-I_2/I_1$. Note that $\Delta n > 0$ is assumed for (a) and (b), but no assumption for Δn is necessary for (c). For a plots, the same parameters were used as for the data in Fig. 3.2 and $\rho = 0.5$.

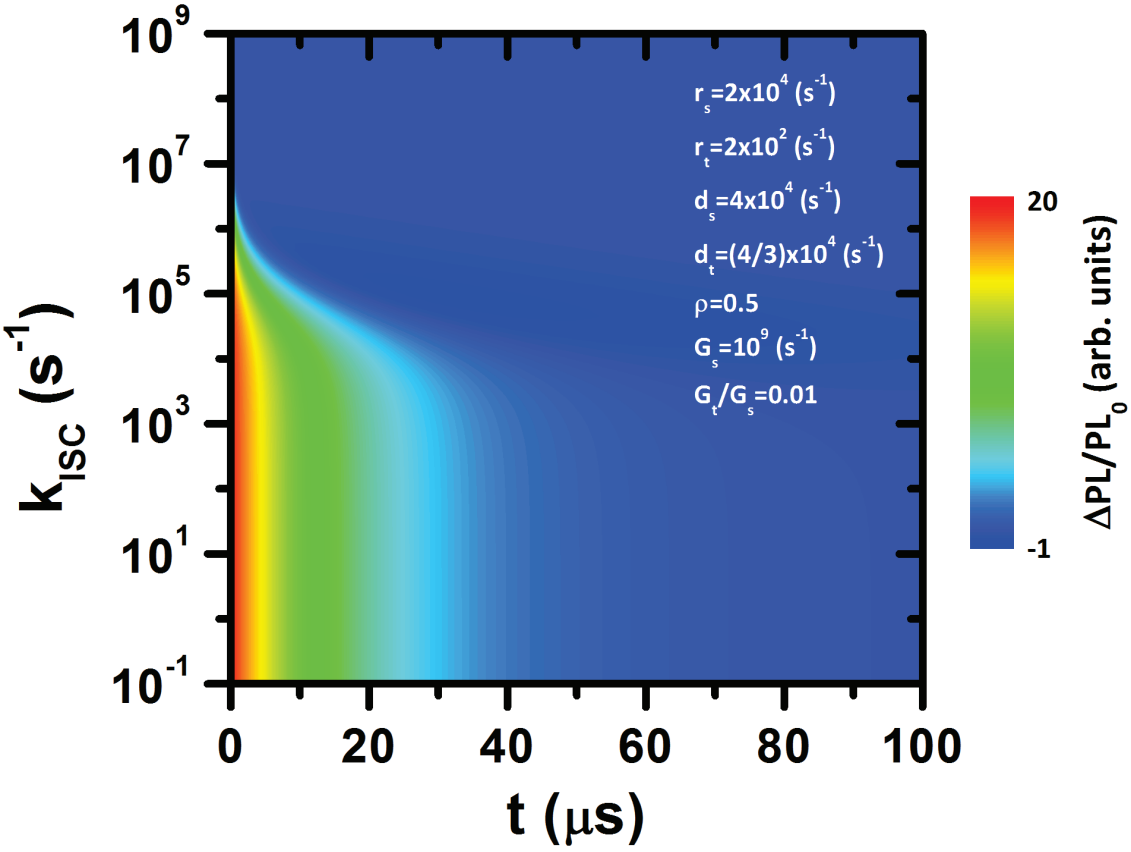

Figure 3.5. Simulated pODMR transients based on the same parameters as in Fig. 3.4 as a function of the intersystem-crossing-rate k_{ISC}. As k_{ISC} becomes large, the transient becomes essentially single exponential because the fast relaxation component is not visible on this time scale.

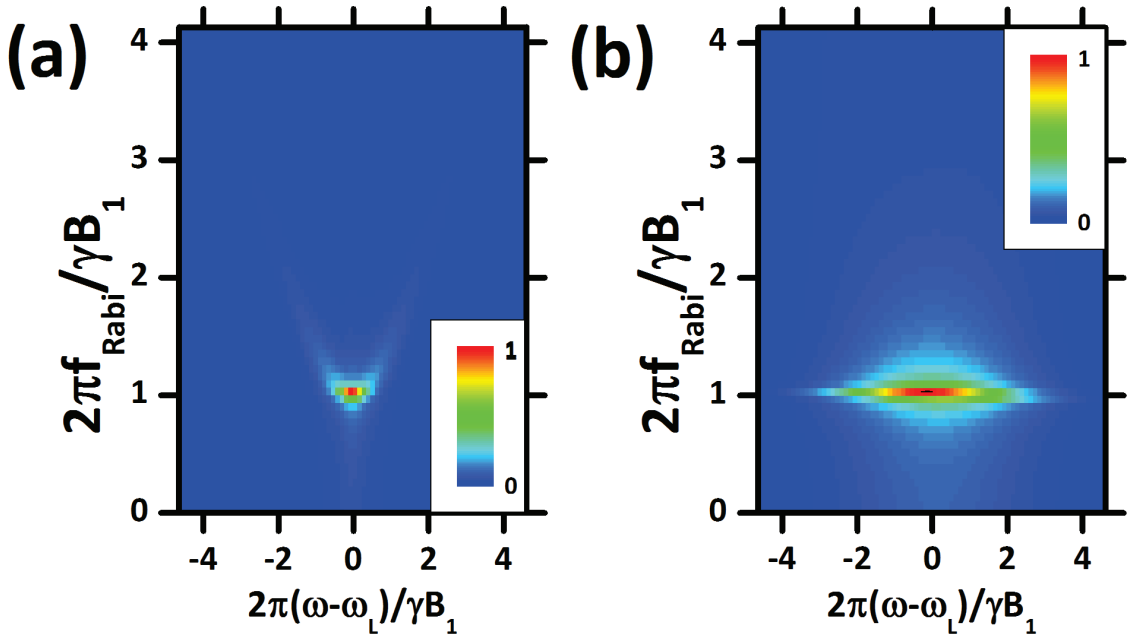

Figure 3.6. Calculation of a pEDMR or pODMR rate changes due to a single excitation pulse. The plot shows the Fast Fourier transform of the calculated data as a function of the excitation frequency in presence of inhomogeneous broadening. The data represent a plot of eq. 3.35 with B_1=1.08 mT and FWHM of (a) 0.94 mT and (b) 1.93 mT. The oscillation components represent Rabi's frequency formula $\sqrt{\gamma^2 B_1^2 + (\omega - \omega_L)^2}$ for the case of small inhomogeneity (a). For inhomogeneities large than γB_1, the hyperbolic feature vanishes and it is replaced by a broad peak (b).

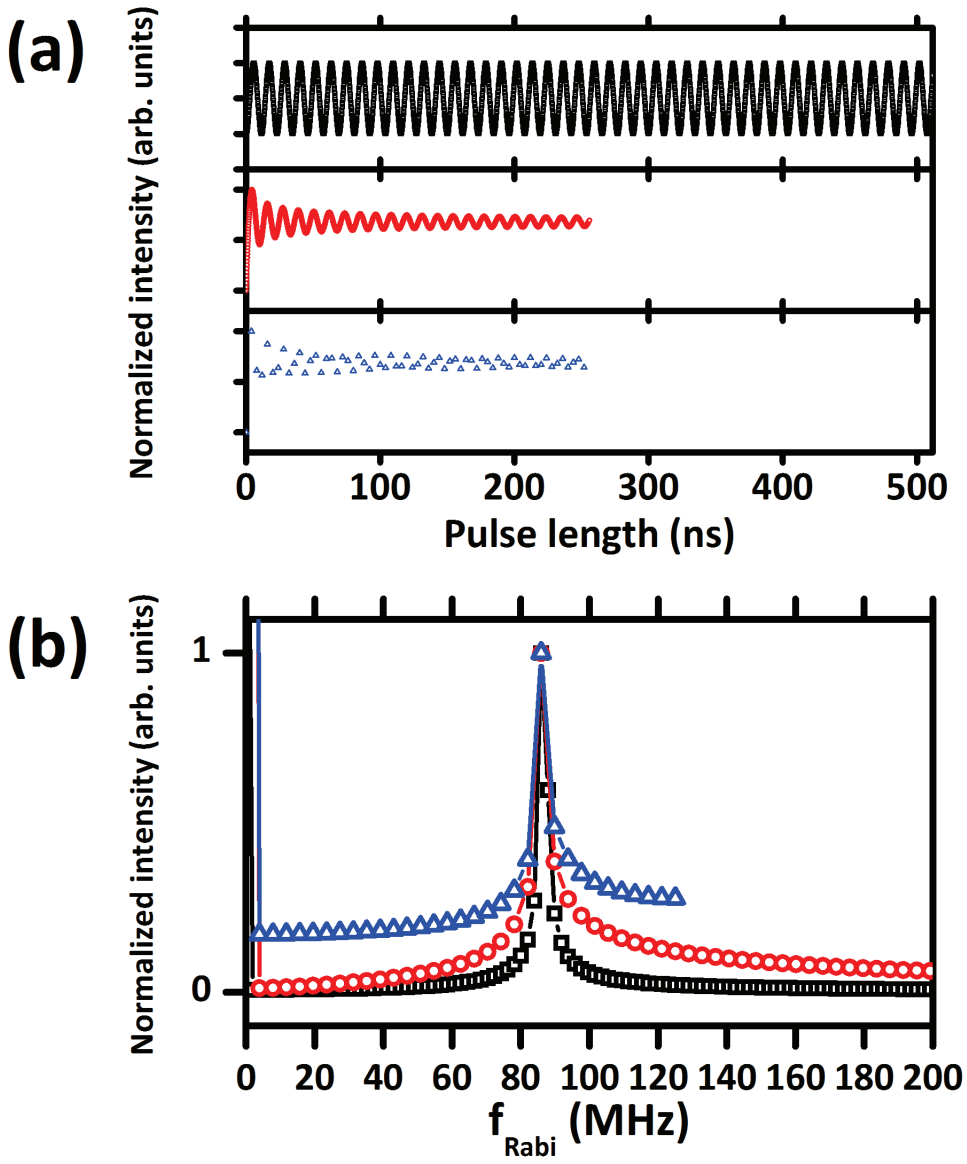

Figure 3.7. Plots of calculated Rabi oscillation data with (black) no inhomogeneous broadening, a short sampling time, and an infinite decay time, (red) a short sampling time but a shorter maximum pulse length, and (blue) a long sampling time (small sampling rate) and the same pulse length as red. (a) Plot of the time domain, (b) Plot of the data in (a) in the frequency domain (Fourier transformed). All data sets are calculated with the same Rabi frequency, but the different sampling rates and frequency resolutions. Black: Sinusoidal with 0.1 ns sampling time and 1.953 MHz frequency resolution. Red: Calculated according to eq. 3.35 with the same sampling rate as black curve but 3.906 MHz frequency resolution. Blue: Calculated according to eq. 3.35 with the same frequency resolution as the blue curve but a sampling rate of 4 ns. The highest frequency of the Fourier transforms of the black and red curves is 9 GHz but only data up to 200 MHz are plotted. All curves are normalized by their respective maximum intensities.

Table 3.1. Steady state pair densities at two limiting cases

	$k_{ISC} \to 0$	$k_{ISC} \to \infty$
n^0_{sp}	$\frac{G_s}{C_s}$	$\frac{\rho\cdot(G_s+G_t)}{\rho\cdot C_s+(1-\rho)\cdot C_t}$
n^0_{tp}	$\frac{G_t}{C_t}$	$\frac{(1-\rho)\cdot(G_s+G_t)}{\rho\cdot C_s+(1-\rho)\cdot C_t}$

Table 3.2. Rates at two limiting cases

	$k_{ISC} \to 0$	$k_{ISC} \to \infty$
m_{12}	C_t	$(1-\rho)C_s + \rho C_t$
m_{22}	C_s	k_{ISC}

Table 3.3. Coefficients at two limiting cases

	$k_{ISC} \to 0$	$k_{ISC} \to \infty$
A_{1p}	0	0
B_{1p}	$-\Delta n$	0

Table 3.4. Intensities of pODMR at two limiting cases

	$k_{ISC} \to 0$	$k_{ISC} \to \infty$
I_1	$-r_t$	0
I_2	r_s	$r_s - r_t$

3.5 References

[1] C. Boehme and K. Lips. *Physical Review B*, 68:245105, 2003.

[2] D. R. McCamey, K. J. v. Schooten, W. J. Baker, S.-Y. Lee, S.-Y. Paik, J. M. Lupton, and C. Boehme. *Physical Review Letters*, 104:017601, 2010.

[3] S.-Y. Lee, S.-Y. Paik, D. R. McCamey, J. Yu, P. L. Burn, J. M. Lupton, and C. Boehme. *Journal of the American Chemical Society*, 133:2019–2021, 2011.

[4] A. Gliesche, C. Michel, V. Rajevac, K. Lips, S. D. Baranovskii, F. Gebhard, and C. Boehme. *Physical Review B*, 77:245206, 2008.

[5] E. Zavoiski. *Journal of Physics USSR*, 9:211, 1945.

[6] F. Bloch, W. W. Hansen, and M. Packard. *Physical Review*, 70:474, 1946.

[7] E. M. Purcell, H. C. Torrey, and R. V. Pound. *Physical Review*, 69:37, 1946.

[8] E. L. Hahn. *Physical Review*, 80:580, 1950.

[9] R. R. Ernst and W. A. Anderson. *Review of Scientific Instruments*, 37:93–102, 1966.

[10] R. J. Blume. *Physical Review*, 109:1867, 1958.

[11] E. J. R. C. P. Keijzers and J. Schmidt. *Pulsed EPR: A new field of applications*. North Holland, Amsterdam, 1989.

[12] W. G. Breiland, H. C. Brenner, and C. B. Harris. *The Journal of Chemical Physics*, 62:3458–3475, 1975.

[13] V. Weis, K. Möbius, and T. Prisner. *Journal of Magnetic Resonance*, 131:17–24, 1998.

[14] I. Hiromitsu, Y. Kaimori, M. Kitano, and T. Ito. *Physical Review B*, 59:2151, 1999.

[15] C. Boehme and K. Lips. *Physica Status Solidi (b)*, 233:427–435, 2002.

[16] T. Machida, T. Yamazaki, K. Ikushima, and S. Komiyama. *Applied Physics Letters*, 82:409–411, 2003.

[17] C. Boehme and K. Lips. *Physica Status Solidi (c)*, 1:1255 – 1274, 2004.

[18] D. R. McCamey, H. A. Seipel, S.-Y. Paik, M. J. Walter, N. J. Borys, J. M. Lupton, and C. Boehme. *Nature Materials*, 7:723, 2008.

[19] J. Behrends, K. Lips, and C. Boehme. *Physical Review B*, 80:045207, 2009.

[20] D. R. McCamey, S. Y. Lee, S. Y. Paik, J. M. Lupton, and C. Boehme. *Physical Review B*, 82:125206, 2010.

[21] S. Y. Paik, S. Y. Lee, W. J. Baker, D. R. McCamey, and C. Boehme. *Physical Review B*, 81:075214, 2010.

[22] A. R. Stegner, C. Boehme, H. Huebl, M. Stutzmann, K. Lips, and M. S. Brandt1. *Nature Physics*, 2:835, 2006.

[23] S. Y. Paik, S. Y. Lee, D. R. McCamey, and C. Boehme. *to be published*, 2011.

[24] V. Rajevac, C. Boehme, C. Michel, A. Gliesche, K. Lips, S. D. Baranovskii, and P. Thomas. *Physical Review B*, 74:245206, 2006.

[25] S.-Y. Lee, S.-Y. Paik, D. R. McCamey, J. Hu, F. Zhu, A. Madan, and C. Boehme. *Applied Physics Letters*, 97:192104–3, 2010.

[26] C. Boehme, F. Friedrich, T. Ehara, and K. Lips. *Thin Solid Films*, 487:132, 2005.

[27] K. Lips, C. Boehme, and T. Ehara. *Journal of Optoelectronics and Advanced Materials*, 7:13, 2005.

[28] T. W. Herring, S.-Y. Lee, D. R. McCamey, P. C. Taylor, K. Lips, J. Hu, F. Zhu, A. Madan, and C. Boehme. *Physical Review B*, 79:195205, 2009.

[29] C. Michel, A. Gliesche, S. D. Baranovskii, K. Lips, F. Gebhard, and C. Boehme. *Physical Review B*, 79:052201, 2009.

[30] C. Boehme and K. Lips. *Applied Physics Letters*, 79:4363–4365, 2001.

[31] G. W. Morley, D. R. McCamey, H. A. Seipel, L. C. Brunel, J. van Tol, and C. Boehme. *Physical Review Letters*, 101:207602, 2008.

[32] R. N. Ghosh and R. H. Silsbee. *Physical Review B*, 46:12508, 1992.

[33] S. Baranovski. *Charge transport in disordered solids with applications in electronics*. Wiley, Chichester, England ; Hoboken, NJ, 2006.

[34] D. J. Lepine. *Physical Review B*, 6:436, 1972.

[35] D. Kaplan, I. Solomon, and N. F. Mott. *J. Physique Lett.*, 39:51–54, 1978.

[36] T. D. Nguyen, G. Hukic-Markosian, F. Wang, L. Wojcik, X.-G. Li, E. Ehrenfreund, and Z. V. Vardeny. *Nature Materials*, 9:345–352, 2010.

[37] C. G. Yang, E. Ehrenfreund, F. Wang, T. Drori, and Z. V. Vardeny. *Physical Review B*, 78:6, 2008.

[38] W. Harneit, C. Boehme, S. Schaefer, K. Huebener, K. Fostiropoulos, and K. Lips. *Physical Review Letters*, 98:216601, 2007.

[39] J. Behrends, A. Schnegg, K. Lips, E. A. Thomsen, A. K. Pandey, I. D. W. Samuel, and D. J. Keeble. *Physical Review Letters*, 105:176601, 2010.

[40] F. Hoehne, L. Dreher, H. Huebl, M. Stutzmann, and M. S. Brandt. *Physical Review Letters*, 106:187601, 2011.

[41] R. M. Brown, A. M. Tyryshkin, K. Porfyrakis, E. M. Gauger, B. W. Lovett, A. Ardavan, S. A. Lyon, G. A. D. Briggs, and J. J. L. Morton. *Physical Review Letters*, 106:110504, 2011.

[42] S. Simmons, R. M. Brown, H. Riemann, N. V. Abrosimov, P. Becker, H.-J. Pohl, M. L. W. Thewalt, K. M. Itoh, and J. J. L. Morton. *Nature*, 470:69–72, 2011.

[43] F. Hoehne, J. Lu, A. R. Stegner, M. Stutzmann, M. S. Brandt, Rohrm, uuml, M. ller, W. G. Schmidt, and U. Gerstmann. *Physical Review Letters*, 106:196101, 2011.

[44] D. R. McCamey, J. Van Tol, G. W. Morley, and C. Boehme. *Science*, 330:1652–1656, 2010.

[45] H. Huebl, F. Hoehne, B. Grolik, A. R. Stegner, M. Stutzmann, and M. S. Brandt. *Physical Review Letters*, 100:177602, 2008.

[46] B. Naydenov, F. Dolde, L. T. Hall, C. Shin, H. Fedder, L. C. L. Hollenberg, F. Jelezko, and J. Wrachtrup. *Physical Review B*, 83:081201, 2011.

[47] C. Boehme and K. Lips. *Physical Review Letters*, 91:246603, 2003.

[48] N. M. Atherton. *Principles of electron spin resonance*. Ellis Horwood series in physical chemistry. Ellis Horwood, Chichester, 1993.

[49] C. P. Slichter. *Principles of magnetic resonance*. Springer series in solid-state sciences 1. Springer-Verlag, Berlin ; New York, 3rd enl. and updated edition, 1992.

[50] M. H. Levitt. *Spin dynamics : basics of nuclear magnetic resonance*. John Wiley & Sons, Chichester, England ; Hoboken, NJ, 2nd edition, 2008.

[51] R. J. Marks. *Introduction to Shannon sampling and interpolation theory*. Springer texts in electrical engineering. Springer-Verlag, New York, 1991.

CHAPTER 4

SPIN-DEPENDENT PROCESSES IN A SILICON-RICH AMORPHOUS SILICON-NITRIDE SOLAR CELL

Hydrogenated amorphous silicon nitride (a-SiN_x:H) has been used widely as dielectric for thin-film transistors [1], solar cell antireflection- and passivation-layers [2] or as trapping matrix in memory applications [3]. In recent years, nonstoichiometric silicon-rich a-SiN_x:H ($x \ll 1.33$) has also attracted attention as material for tunable light emitting diodes [4] and photoelectrochemical (PEC) hydrogen production [5]. For these applications, charge transport and recombination are of great significance [5, 6]. Transport and recombination in disordered silicon materials involve many kinds of localized, paramagnetic defect states. Because of this, electron paramagnetic resonance has been used extensively for their investigation [7, 8]. With regard to silicon nitride, most of these studies are focused on stoichiometric or nearstoichiometric a-SiN_x:H. Here, we report on a pulsed electrically detected magnetic resonance (pEDMR) study of silicon rich a-SiN_x:H that aimed to answer the question of whether spin-dependent transitions are similar to the stoichiometrically and morphologically very similar hydrogenated amorphous silicon (a-Si:H) or whether small amounts of nitrogen lead to differences in transport and recombination.

This chapter is based on a journal article published in Applied Physics Letters in 2010[1] coauthored by Seoyoung Paik, Dane R. McCamey, and Christoph Boehme from the University of Utah, and Jian Hu, Feng Zhu, and Arun Madan from the MVsystems, in Golden, Colorado. PIN stacks of a-SiN_x:H sample are kindly provided by MVsystems at Colorado, U.S.A.

---

[1]Reprinted with permission from [S.-Y. Lee, S.-Y. Paik, D. R. McCamey, J. Hu, F. Zhu, A. Madan, and C. Boehme, Applied Physics Letters 97 (19), 192104 (2010)]. Copyright 2010, American Institute of Physics.

4.1 Experimental

The pEDMR experiments were carried out in a photovoltaic mode, similar to experiments previously reported on organic light emitting diodes [9] and a-Si:H solar cells [10]. Following coherent manipulation of paramagnetic centers, transient changes to the steady-state short-circuit photocurrent, due to the perturbation of spin-dependent conductivity channels, were recorded. For the experiments, a 300 nm thick a-$SiN_{0.3}$:H film was prepared by plasma enhanced chemical vapor deposition on top of a ZnO coated glass substrate. The top and bottom of the a-$SiN_{0.3}$:H layer were n-doped (10nm) and p-doped (7nm), respectively. Fig. 4.1 (d) illustrates a qualitative band diagram for the device. The bandgap of a-$SiN_{0.3}$:H is about 2 eV, deduced from Tauc's plots [11] from measured transmission data since the optically induced transition in a-SiNx:H is direct. The density of states of a-$SiN_{0:3}$:H has been calculated to be similar to that of a-Si:H [12], however, based on the observation of significantly different Urbach tails (with photothermal deflection spectroscopy, not shown here) we conclude that the density of states of our material differs significantly from a-Si:H. The p-i-n device was capped with a thin Al layer. Details of this 2mm×2mm pEDMR compatible sample are given elsewhere [10]. Optical excess charge carrier injection took place by shining IR and UV filtered spectral light ($T_{\mathrm{LAMP}} = 3000K$), with integrated intensity of 5 W/cm^2. The excitation frequency was 9.742GHz (X-Band), $T_{\mathrm{SAMPLE}} = 15K$. Dark and illuminated IV curves of the p-i-n devices were measured at room temperature and $T = 15$K (Fig. 4.1 (h) and (i), respectively). Note the low current densities of a-$SiN_{0.3}$:H due to the large Pool-Frenkel transport barrier height for the given stoichiometry [13]. While this makes a-$SiN_{0.3}$:H an inferior material for pure photovoltaic applications, it is not a fundamental drawback for PEC applications [5].

4.2 pEDMR transients and I-Vs

Fig. 4.1 (b) displays the change of the photocurrent $\Delta I_{ph}(t)$ as function of time t and the applied magnetic field (expressed as Landé-factor g). The data show that for $g \approx 2$, a temporary photocurrent change occurs after the pulse at $t = 0$. Fig. 4.1 (a),(c), and (e),(f),(g) are plots of time and magnetic field slices taken from Fig. 4.1 (b), respectively. They reveal that $\Delta I_{ph}(t)$ exhibits enhancement ($t \leq 50\mu$s) and quenching ($t > 50\mu$s) contributions as expected from signals caused by spin-selection rules [9, 14]. Due to weak spin-orbit coupling, all spin-dependent processes produce photocurrent changes at $g \approx 2$. Deconvolution of the magnetic field spectra by resonance line fits is therefore ambiguous. Thus, whilst it is clear that there are spin dependent processes in this material, little

information regarding their physical nature can be obtained from the data in Fig. 4.1.

4.3 Electrically detected spin Rabi nutation

In order to separate the different contributions contained in the spectrum of Fig. 4.1, we measured electrically detected spin-Rabi nutations as a function of the applied magnetic field B_0. We followed the measurement approach of previous pEDMR [10, 15] and pODMR [10, 14] studies - we integrated the current transient $\Delta I_{ph}(t)$ into a charge ΔQ after pulsed excitation, repeatedly to measure $\Delta Q(\tau)$ as a function of the pulse length τ. PEDMR detected spin-Rabi nutation allows us to distinguish pair correlation effects (spin-beating) [15, 16] and spin coupling effects [14, 17] from the various nutation frequency components. The two-dimensional map of g-factors versus nutation components enables significantly better discrimination of the various signal components contained in the observed transition rates.

Fig. 4.2 (a) to (c) displays $\Delta Q(B_0, \tau)$ revealing oscillatory behavior. (a) and (c) are nutation slices that show different nutation frequencies and dephasing times at different g-factors. This indicates the presence of different electronic transitions. Fig. 4.2 (d) to (f) displays the Fast Fourier Transform of the data sets displayed in (a) to (c). Fig. 4.2 (e) shows nutation frequencies (in units of the spin $s = \frac{1}{2}$ nutation frequency γB_1, with γ the gyromagnetic ratio and B_1 the radiation field strength) as a function of g. It reveals a number of recognizable frequency components ($2\pi f_{Rabi} \approx \gamma B_1$, $\sqrt{2}\gamma B_1$, $2\gamma B_1$ and others) whose g-dependence is plotted in Fig. 4.3 (a) to (c). Detailed discussions about the origins of different frequency components will be discussed in the following sections.

4.3.1 Weakly coupled spin pairs

The γB_1-signal plotted in Fig. 4.3 (a) can be attributed to pairs of weakly coupled spins consisting of one broad and one narrow Gaussian resonance at $g = 2.0111(2)$ and $g = 2.0047(1)$, respectively. We assign the $g \approx 2.01$-signal to valence band tail states, as known from a-Si:H [10, 14]. However, it is difficult to exactly determine the origin of the narrow peak. Silicon dangling bond and conduction band tail states in a-Si:H, are at $g \approx 2.0055$ and $g \approx 2.004$, respectively [10, 14]. In a-SiN_x:H, the Si dangling bond surrounded by three N atoms (K-center) has $g \approx 2.003$ [7]. Using these literature values, all three electronic centers could be the origin of the narrow peak.

4.3.2 Dipolar coupled spin pairs

The very broad signal plotted in Fig. 4.3 (b) is associated with the frequency of $\sqrt{2}\gamma B_1$. This frequency has been assigned to the Rabi frequency of dipolar coupled spins in a-Si:H [10, 14]. However this assignment has been based on the theoretical prediction for the transient nutation of magnetic polarization, and there has been no theoretical prediction for $\sqrt{2}\gamma B_1$ Rabi frequency detected by pEDMR and pODMR. Recently, Wang et al. have solved the Louville equation for spin pairs mediated via dipolar coupling, and found that the Rabi nutation of the total recombination rate is associated with a distinctive frequency [18]. This frequency is larger than γB_1 as long as the dipolar coupling strength is larger than the Larmor separation and never exceeds $\sqrt{2}\gamma B_1$ no matter how strong the dipolar coupling strength is. This means that the Rabi nutation frequency detected by pODMR and pEDMR converges to $\sqrt{2}\gamma B_1$ as the dipolar coupling strength increases. It also has been found that there is another frequency component whose frequency is always lower than the first component. In Fig. 4.2 (e), one can find frequency components whose frequencies are lower than γB_1. However, these signals should not be confused with the signals of the dipolar coupled spin pairs because these signals do not have imprints of Pake doublet which should always appear if spin pair partners are dipolar coupled [19]. These lower frequency components of dipolar coupled spin signals may not be visible because they appear outside the detected g-factor range. This explanation is valid if strong exchange interaction exists because these low frequency dipolar signals are from singlet to triplet state transitions. As will be explained later, the separation of the Pake doublet from the lower frequency component is determined by the exchange coupling constant.

According to Atherton [20], the Hamiltonian of dipolar coupled spin pairs is

$$H_d = \mathbf{S} \cdot \mathbf{D} \cdot \mathbf{S}, \tag{4.1}$$

where $\mathbf{D}$, the dipolar spin-spin coupling tensor. which becomes for S=1 and uniaxial symmetry system

$$H_d = D\{S_z^2 - \frac{1}{3}S(S+1)\}. \tag{4.2}$$

When an external B_0 field along +z direction is present, the eigenvalues can be obtained as summarized in Table 4.1 where $D = D_0(1 - 3cos^2\theta)$ with θ showing the angle between the +z direction and the line connecting two spins in the pair. Note that the exchange coupling constant J is added to consider the singlet-triplet splitting due to exchange interaction. The transition energies required for each transitions shown in Fig. 4.4 are summarized in Table 4.2. One can find that triplet-to-triplet transitions are not affected by the nonzero

exchange coupling but triplet-to-singlet transitions are affected. The latter corresponds to the lower Rabi frequency signals of dipolar coupled spins in pEDMR and pODMR experiments. In addition, the resonance frequency shifts are $\Delta\nu = \pm\nu_0(1 - 3cos^2\theta)$ for triplet to triplet transitions and $\Delta\nu = \pm\frac{\nu_0}{3}(1 - 3cos^2\theta)$ for triplet-to-singlet transitions. They are plotted in Fig. 4.5. It should be noted that the width of the Pake peak of triplet-to-singlet transition is one third of the width of triplet-to-triplet transition. Thus, the lower frequency signals of dipolar coupled spin pairs have narrower linewidth and their separation is determined by the exchange coupling strength while the separation of the higher frequency signals is not affected by the exchange coupling.

Thus we can attribute the broad $\sqrt{2}\gamma B_1$-signal plotted in Fig. 4.3 (b) to spin-dependent transitions between spin-dipolar coupled charge carrier pairs. The Pake-spectrum expected for dipolar coupling [14] is buried under the high frequency tails of the strong signals of weakly coupled pairs (see Fig. 4.2 (f) which shows the asymmetric frequency distribution). A fit of the Pake spectrum should be combined with an additional broad Gaussian peak to consider contributions of the high frequency tails of the weakly coupled spin pairs. The Pake doublet of the fit is obtained by consideration of line broadening due to the power broadening, inhomogeneous distribution of g-factors, and distribution of the distance between pair partners of dipolar coupled pairs. Because $D_0 = \frac{\mu_0 g_a g_b \mu_B^2}{4\pi h}\frac{1}{r^3}$, the average distance between pair partners can be obtained from the fit result. Good fit results were achieved for distance distributions between 6.0 and 6.7 Å. The solid line in Fig. 4.3 (b) displays the best result for $r_{av} = 6.2 \pm 0.2\mathring{A}$.

4.3.3 Strongly exchange coupled spin pairs

Fig. 4.3 (c) shows the spectrum of the $2\gamma B_1$ contribution which is fit by a single Gaussian line centered at $g = 2.0094(3)$. It is known that the pEDMR detected doubling of the spin $s = \frac{1}{2}$ nutation frequency can be explained by quantum beats of the spin pairs. There are two known origins for these beats: (i) Double excitation of the pair partners by the magnetic resonant pulse [16], and (ii) beating due to strong exchange coupling within the spin pair [17]. The two cases differ in that the double excitation requires a radiation field strength (B_1) in excess of the pair partners Larmor frequency difference, while the exchanged coupled pairs display beating at any excitation strength. Thus, measuring the beat signals intensity as function of B_1 allows the beatings origin to be determined. Fig. 4.6 displays the B_1-dependence of the spin-Rabi nutation frequencies as well as the ratio of the beat signal intensity over the nutation signal intensity [15]. The data do not exhibit a significant dependence on B_1 and we thus attribute the observed beat signal to exchange coupled

pairs. Note that the beat signal Landé-factor $g = 2.0094$ is close to the average of the weakly coupled resonance peaks. We conclude from this that the valence band states are not only involved in weakly coupled pairs but also strongly exchange coupled pairs. The inter pair distance, and thus coupling strength, between the pair partners appears to be broadly distributed in the disordered network.

The measurements presented above show that spin-dependent charge carrier transitions of a-$SiN_{0.3}$:H and a-Si:H are very similar as both involve valence and conduction band tail states as well as silicon dangling bonds. In spite of this similarity, the measurements also show that, in contrast to a-Si:H, the photocurrent of a-$SiN_{0.3}$:H is significantly influenced by charge carrier pairs with strong exchange and dipolar coupling. The detection of charge carrier transitions between predominantly dipolar coupled states with separation of only $6\mathring{A}$ (about a third of what is seen in a-Si:H using optical measurements [14]) implies that these states are highly localized and therefore likely deep in the band gap. Previous experiments on a-Si:H showed that strongly spin-coupled charge carriers are predominantly correlated (geminate) pairs that can be observed only through optical detection while spin-dependent effects on photoconductivity in a-Si:H have been observed only with weakly spin-coupled pairs [10]. In contrast, for a-$SiN_{0.3}$:H, uncorrelated (nongeminate) charge carriers are likely to form strongly spin-coupled pairs. Since illumination always produces geminate excess charge carrier pairs, the nongeminate pairs must form from previously dissociated geminate pairs. We therefore conclude that a-$SiN_{0.3}$:H allows a greater fraction of optically induced excess charge carrier pairs to dissociate than a-Si:H. This enhanced charge carrier separability may be of significance for increased internal quantum efficiencies of a-SiN_x:H in PEC applications.

4.4 Summary

In summary, we have used pEDMR in order to map spin-dependent transition rates in a-$SiN_{0.3}$:H p-i-n devices according to g-factors and spin coupling-types and -strengths. The results confirm the hypothesis that Si rich a-SiN_x:H exhibits qualitatively similar processes to a-Si:H. However, in contrast to a-Si:H, highly localized, strongly spin-coupled electronic states are involved in transitions affecting photoconductivity. This is indicative that the material enhances the conversion of geminate to nongeminate charge carrier pairs. We note the potential significance of this for the suitability of Si rich a-SiN_x:H for PEC electrode applications.

4.5 Acknowledgement

Acknowledgment is made to the donors of the American Chemical Society Petroleum Research Fund under Grant No. PRF 48916-DNI10 for support of this research.

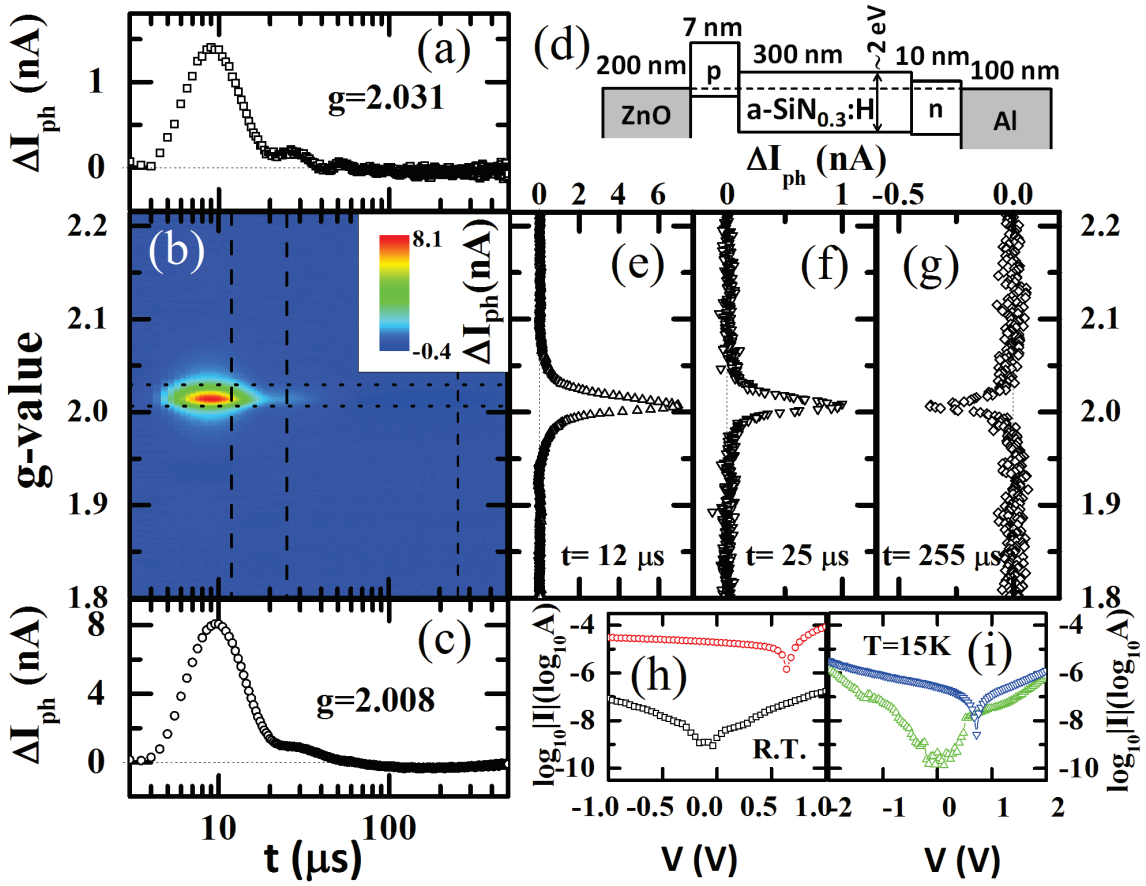

Figure 4.1. Transient measurements of spin-controlled currents following a $\tau = 172$ns long excitation pulse applied at $t = 0$. (b) Current change $\Delta I_{ph}(t)$ as a function of time t and the excited g-value (corresponding to the static magnetic field applied to the sample). (a) and (c) are two time slices from panel (b) for $g = 2.031$ and $g = 2.008$, respectively. Panels (e),(f) and (g) are g-factor (magnetic field) slices from panel (b) for different times after the pulse. (d) Sketch of the p-i-n structure with a-$SiN_{0.3}$:H bandgap of ~ 2 eV [12] (not to scale geometrically). (h,i) I-V curves with (top) and without (bottom) illumination measured at room temperature and $T = 15$K.

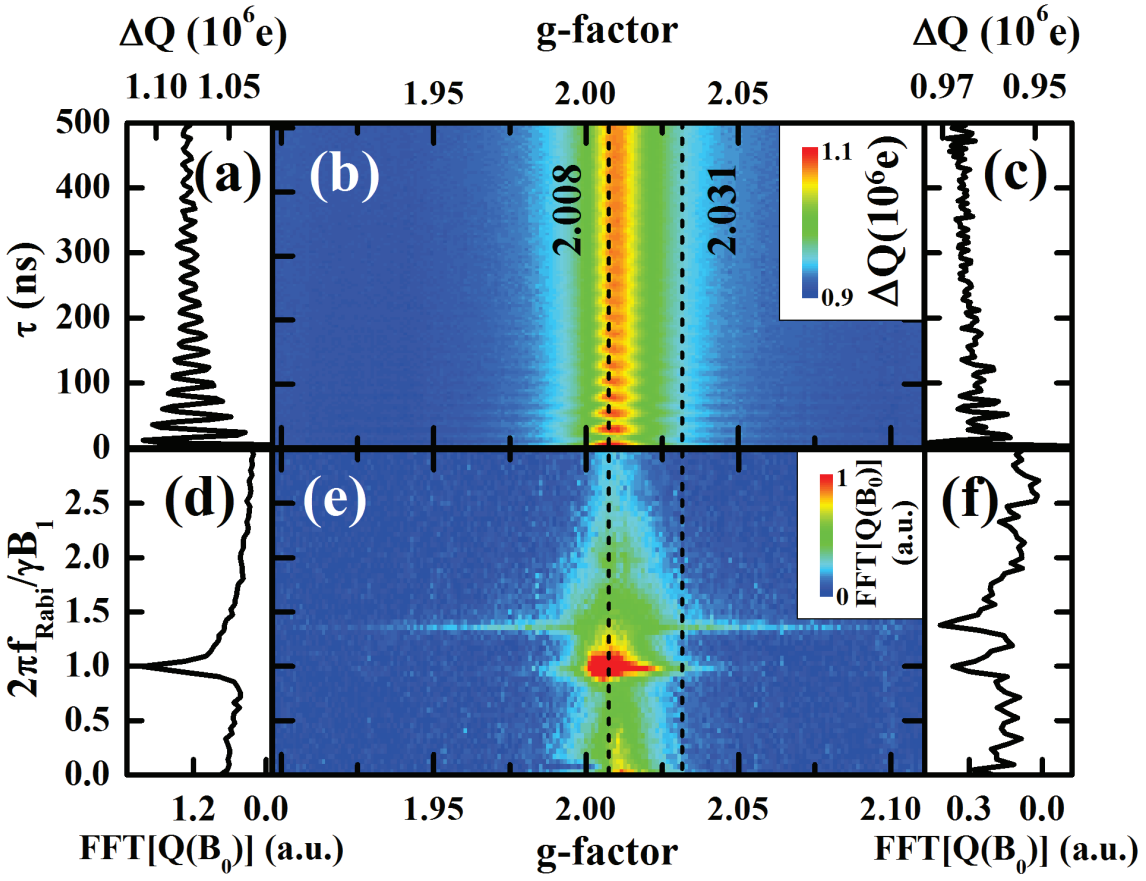

Figure 4.2. Measurement of spin-Rabi nutation with $B_1 = 1.4$ mT. (b) Plot of integrated photocurrent changes ΔQ after pulsed excitation as a function of the applied g-factor and pulse length τ. (a), (c) Pulse length slices from (b) for $g = 2.008$ and $g = 2.031$. (e) Fast Fourier transform of the data in (b) plotted as function of g and the Rabi frequency f_{Rabi} in units of γB_1. (d), (f) Frequency slices from (e) for $g = 2.008$ and $g = 2.031$.

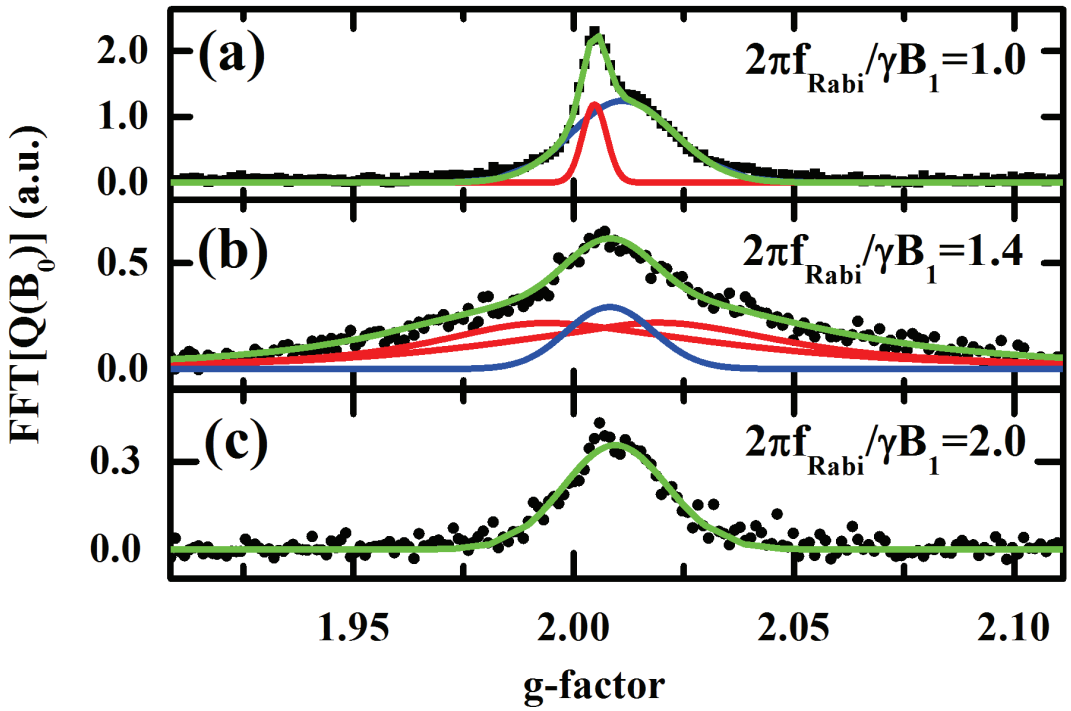

Figure 4.3. Landé g-factor dependence of spin-Rabi nutation with $B_1 = 1.4$ mT. Landé g-factor slices obtained from Fig. 4.2 at (a) $f_{\text{Rabi}} = \gamma B_1$ (weakly coupled spins), (b) $f_{\text{Rabi}} = 1.4\gamma B_1$ (predominantly dipolar coupled spins) and (c) $f_{\text{Rabi}} = 2\gamma B_1$ (predominantly exchange coupled spins). Green curves are final fit results. In (a), red and blue lines are two Gaussian peaks. Assignments of these peaks can be found in text. In (b), red curves are Pake doublet fit and blue curve is broad Gaussian peak representing contribution of high frequency tail of weakly coupled spin pair signal.

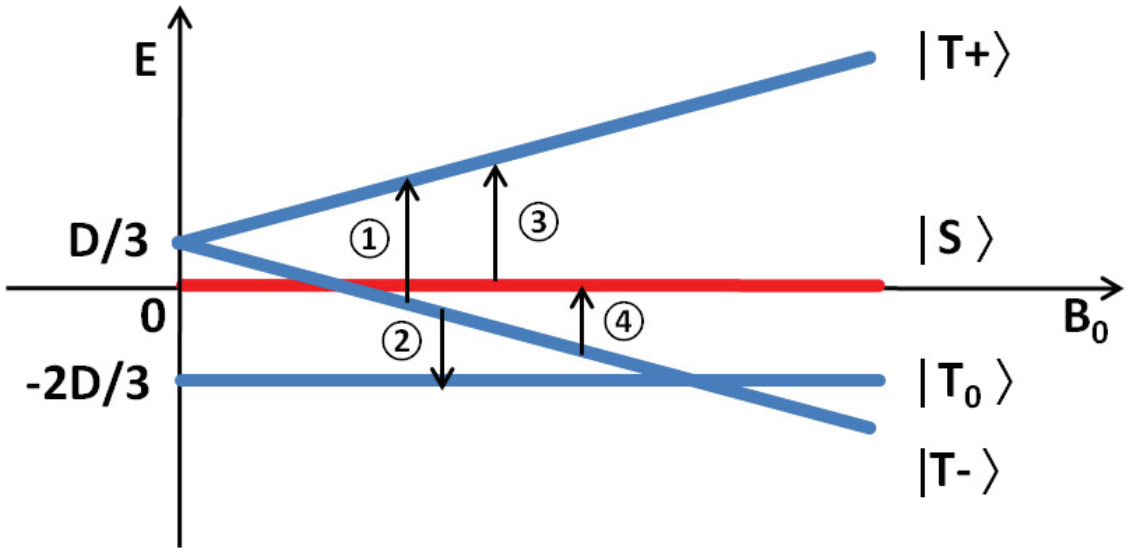

Figure 4.4. The energies of four s=1/2 pair system eigenstates as a function of the magnetic field. For simplicity, splitting due to dipolar interaction is shown only. Arrows indicate $\Delta m = 1$ transitions.

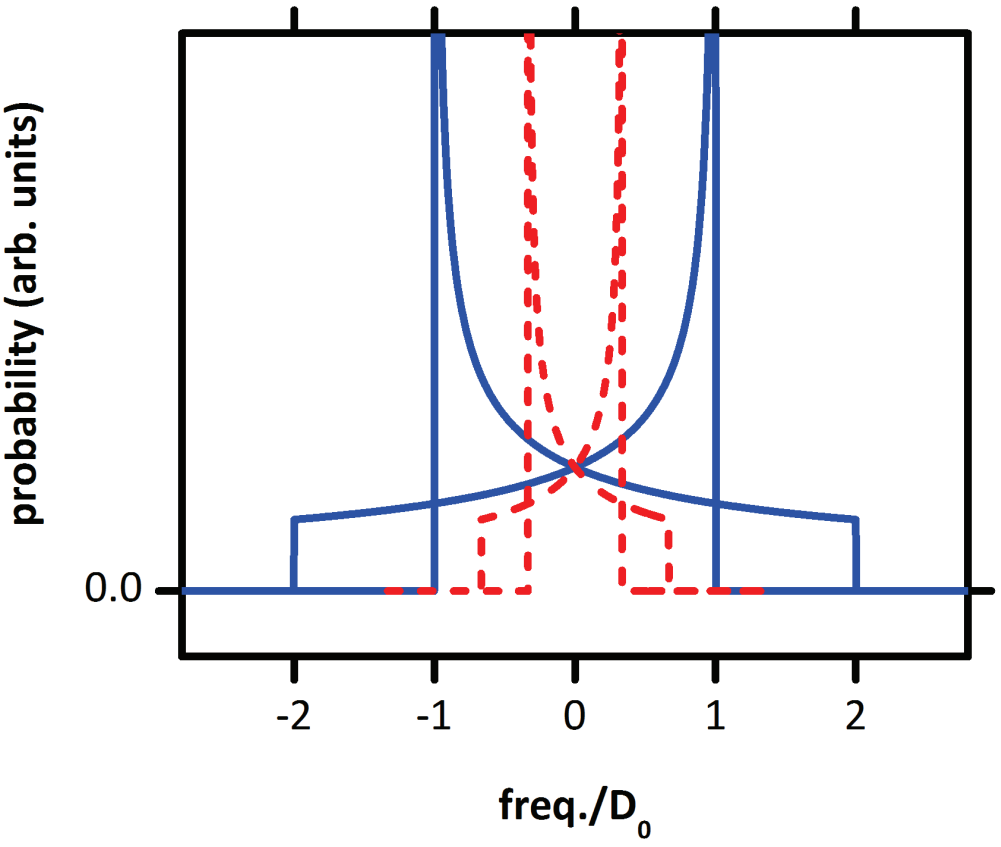

Figure 4.5. Pake patterns for triplet-to-triplet transition (blue solid curves) and triplet–to-singlet transition (red dotted curves). Width of blue solid curve is $3D_0$ and width of red dotted curve is D_0.

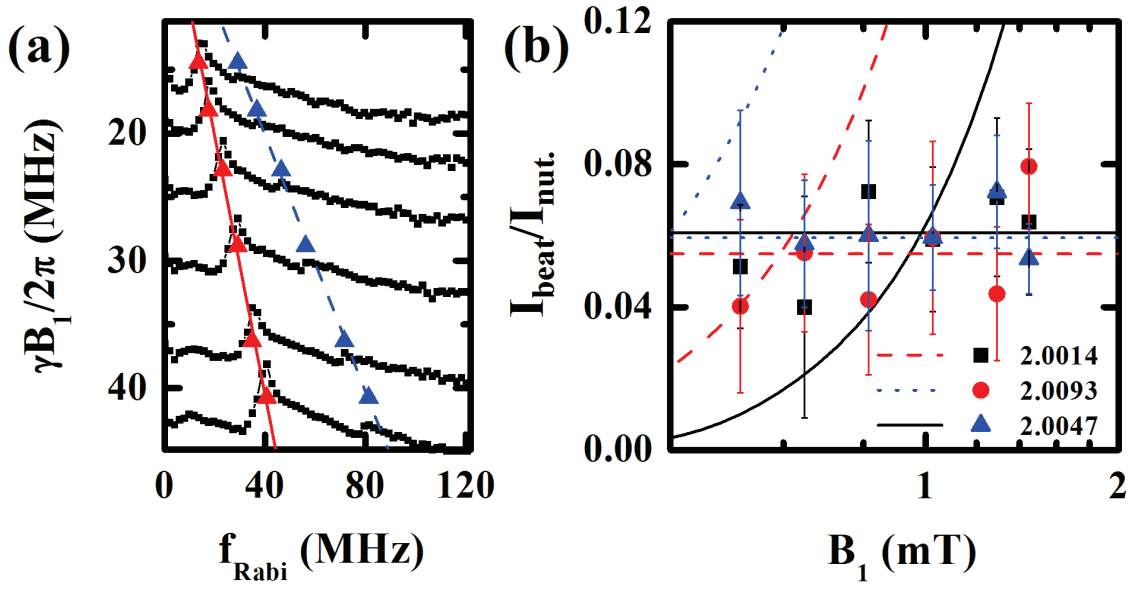

Figure 4.6. Electrically detected Rabi nutations at various B_1 field strength. (a) Nutation spectra measured for $g = 2.0047$ ($B_0 = 347.2$mT) as a function of the applied B_1 field. (b) Plot of the ratio of the beat signal intensity I_{beat} and nutation signal intensity I_{nut} as a function of B_1 for three different magnetic fields around $g = 2.0047$. The solids lines represent the expected B_1-dependence of exchange coupled (constant) and weakly coupled (sloped) pairs.

Table 4.1. Eigenenergies of the four spin s=1/2 pair states.

$\|s,m\rangle$	eigenvalue
$\|1,+1\rangle$	$\frac{1}{3}D + J + g\mu_B B_0$
$\|1,0\rangle$	$-\frac{2}{3}D + J$
$\|1,-1\rangle$	$\frac{1}{3}D + J - g\mu_B B_0$
$\|0,0\rangle$	0

Table 4.2. Transition energy required for triplet-to-triplet transition and triplet-to-singlet transition.

transition	transition energy
1) from T_0 to T_+	$h\nu = g\mu_B B_0 + D$
2) from T_- to T_0	$h\nu = g\mu_B B_0 - D$
3) from S to T_+	$h\nu = g\mu_B B_0 + \frac{1}{3}D + J$
4) from T_- to S	$h\nu = g\mu_B B_0 - \frac{1}{3}D - J$

4.6 References

[1] M. J. Powell, B. C. Easton, and O. F. Hill. *Applied Physics Letter*, 38:794, 1981.

[2] C. Boehme and G. Lucovsky. *Journal of Non-Crystalline Solids*, 299-302:1157–1161, 2002.

[3] S. Choi, H. Yang, M. Chang, S. Baek, H. Hwang, S. Jeon, J. Kim, and C. Kim. *Applied Physics Letter*, 86:251901, 2005.

[4] N.-M. Park, T.-S. Kim, and S.-J. Park. *Applied Physics Letter*, 78:2575, 2001.

[5] F. Zhu, J. Hu, I. Matulionis, T. Deutsch, N. Gaillard, A. Kunrath, E. Miller, and A. Madan. *Philosophical Magazine*, 89:2723, 2009.

[6] H. L. Lao, L. K. Wu, W. Z. Shen, and H. F. W. Dekkers. *Applied Physics Letter*, 91:201922, 2007.

[7] P. M. Lenahan and S. E. Curry. *Applied Physics Letter*, 56:157, 1990.

[8] W. L. Warren, F. C. Rong, E. H. Poindexter, G. J. Gerardi, and J. Kanicki. *Journal of Applied Physics*, 70:346, 1991.

[9] D. R. McCamey, H. A. Seipel, S.-Y. Paik, M. J. Walter, N. J. Borys, J. M. Lupton, and C. Boehme. *Nature Materials*, 7:723, 2008.

[10] T. W. Herring, S.-Y. Lee, D. R. McCamey, P. C. Taylor, K. Lips, J. Hu, F. Zhu, A. Madan, and C. Boehme. *Physical Review B*, 79:195205, 2009.

[11] J. Tauc. *Amorphous and liquid semiconductor*. Plenum, New York, 1 edition, 1974.

[12] J. Robertson. *Philosophical Magazine B*, 63:47, 1991.

[13] S. Habermehl and C. Carmignani. *Applied Physics Letter*, 80:261, 2002.

[14] K. Lips, C. Boehme, and T. Ehara. *Journal of Optoelectronics and Advanced Materials*, 7:13, 2005.

[15] D. R. McCamey, K. J. v. Schooten, W. J. Baker, S.-Y. Lee, S.-Y. Paik, J. M. Lupton, and C. Boehme. *Physical Review Letters*, 104:017601, 2010.

[16] V. Rajevac, C. Boehme, C. Michel, A. Gliesche, K. Lips, S. D. Baranovskii, and P. Thomas. *Physical Review B*, 74:245206, 2006.

[17] A. Gliesche, C. Michel, V. Rajevac, K. Lips, S. D. Baranovskii, F. Gebhard, and C. Boehme. *Physical Review B*, 77:245206, 2008.

[18] J. Wang, S.-Y. Lee, W. Baker, and C. Boehme. *to be published*.

[19] G. E. Pake. *The Journal of Chemical Physics*, 16:327–336, 1948.

[20] N. M. Atherton. *Principles of electron spin resonance*. Ellis Horwood series in physical chemistry. Ellis Horwood, Chichester, 1993.

CHAPTER 5

SPIN-DEPENDENT RECOMBINATION OF POLARON PAIRS IN MEH-PPV

Organic semiconductors are used for various optoelectronic devices like organic light emitting diodes, flat panel displays and solar cells. Aside from their color brilliance and mechanical flexibility, these materials also provide significant advantage in cost and fabrication. In spite of these properties, there is still an insufficient understanding of the fundamental processes that limit quantum- and energy conversion-efficiencies. While spin-dependent electronic transitions (mostly recombination) are an important factor for efficiency (as only charge carrier pairs in a singlet state fluoresce), it is not known how fast the triplet to singlet intersystem crossing rate can be and thus our knowledge of the fundamental efficiency limitations of OLEDs is limited. In order to enhance our understanding of spin-dependent recombination we conducted pulsed Optically Detected Magnetic Resonance (pODMR) measurement on poly[2-methoxy-5-(20-ethyl-hexyloxy)-1,4-phenylene vinylene] (MEH-PPV) based organic light emitting diodes.

This chapter is based on a journal article published in Journal of the American Chemical Society in the year 2011[1] coauthored by Seoyoung Paik, Dane R. McCamey, John M. Lupton, and Christoph Boehme at the University of Utah, U.S.A., and Justin Yu and Paul L. Burn at the University of Queensland, Australia. Deuterated MEH-PPV samples were provided by Justin Yu and Paul L. Burn.

We analyzed the time dependence of photo fluorescence rates via magnetic resonant spin manipulation which changes spin-dependent photoluminescence rates. Using a rate model for the description of exciton precursor pair generation, dissociation, recombination and intersystem crossing we were able to give estimates for various rate coefficients including the intersystem crossing time which is of profound relevance for the efficiency limits of OLEDs and also for the understanding of organic magnetoresistance effects. We also observed

[1]Reprinted with permission from [S.-Y. Lee, S.-Y. Paik, D. R. McCamey, J. Yu, P. L. Burn, J. M. Lupton and C. Boehme, Journal of the American Chemical Society 133 (7), 2019-2021 (2011)]. Copyright 2011, American Chemical Society.

coherent spin effects using pODMR such as spin-Rabi nutation signals. The results of these measurements give information about the mutual coupling of the polarons within the precursor pairs as well as the hyperfine-coupling to surrounding hydrogen nuclei. The results show that polaron pairs are coupled remarkably weakly as both the spin-dipolar coupling and exchange coupling within the pairs is weak and spin-orbit coupling is also observed to be small.

One of the most appealing promises of organic semiconductors is the ability to tune a particular material property by synthetic means. While this approach has been explored widely, for example, in the context of color control for organic light-emitting diodes (OLEDs), there are some important material parameters relating to the spin degree of freedom which have received virtually no attention at all. Organic semiconductors typically consist of low atomic-order number atoms and are characterized by weak spin-orbit coupling, giving rise to exceptional spin lifetimes. In addition, exchange correlations and the high degree of localization of excitations give rise to a distinct splitting of excitations into the singlet and triplet manifold. This splitting controls crucial material properties through spin-dependent dissociation and recombination of charge carriers [1–16]. Although the resulting spin-dependent transport phenomena have been studied for decades, it was recently realized that the electron spin can itself be used as the information carrier in an organic spintronics device [17, 18]. Such devices promise new avenues towards information storage and processing, and sensing and imaging, highlighting the need for a more systematic understanding and control of material characteristics relating to spin [19–21].

In the following sections, we also demonstrate direct control over the hyperfine field strength experienced by charge carriers in a conjugated polymer, and explore the influence of deuteration on spin-dependent device characteristics. By comparing pulsed electrically and optically-detected magnetic resonance (pEDMR and ODMR), we are able to show the equivalence of spin-dependent observables under optical and electrical excitation. The hyperfine field strength controls the coupling between spins, leading to the pronounced effect of spin beating which is detected directly in the photoluminescence (PL) of the polymer.

5.1 Experimental

For pODMR, solution of MEH-PPV (poly[2-methoxy-5-(2'-ethylhexyloxy)-1,4-phenylene-vinylene) was drop-cast and a fiber bundle consisting of several detection fibers and one excitation fiber (at the bundle center) was placed on top of the substrate. Both the substrate and the fiber bundle were fixed by a surrounding quartz tube. A blue light laser(Ar^+

ion laser, wavelength 488 nm, power 10 W/cm^2) was used to illuminate the sample and to therefore to establish a steady state electron-hole pair generation rate. The PL was measured by an Si-PIN photodiode detector. B_1-field pulses with a frequency of 9.6817 GHz were then applied in presence of a variable B_0 field. In order to determine the exact B_1 field strength, spin-Rabi nutations of MEH-PPV were recorded for various microwave powers and the slope of the plot of Rabi frequency as a function of the squareroot of the microwave power was determined as power to B_1 field conversion factor. All measurements were done at $T \simeq 10K$

5.2 Polaron pair recombination model

To understand the transient PL change of an organic semiconductor after a microwave pulse, we consider a simple statistical rate picture based on the Kaplan-Solomon-Mott model [22, 23] illustrated in Fig. 5.1 following the discussions in Chapter 2 and 3. Here, the intermediate pairs consist of strongly Coulombically coupled but at the same time, weakly spin-spin coupled pairs of electron- and hole-polarons. Triplet and singlet polaron pairs can form triplet and single excitons, with rates k_t and k_s, respectively. Recombination of singlet exciton pairs creates photons. Polaron pairs can not only recombine into exciton states, they can also dissociate without recombination. This process increases the sample current and is statistically described by rate coefficients d_t and d_s for triplet and singlet polaron pairs, respectively. The rate picture in Fig. 5.1 also covers the possibility of longitudinal spin relaxation of polaron spins which transform singlet polaron pairs into triplet polaron pairs and vice versa. Spin process, also referred to as spin-mixing, occurs randomly with a rate coefficient k_{SL}. However, by application of magnetic resonance to one or both spin within the polaron pair, one can increase spin-mixing rates [23]. Note that this model in Fig. 5.1. is very similar to the rate model described by McCamey et al. [24], except that in the latter, k_{ISC} considered negligible. Also in contrast to McCamey's work, we use this rate model to make predictions about the number of photons as observable (as needed for pODMR experiments) instead of the number of electrons (as needed for pEDMR experiments). Thus, the model used for the description of the experiments presented in the following is essentially the pODMR rate model discussed in Chapter 3.

In order to extract the rate constants from the measured exponential decay transients, fully analytical solutions for time transient including all rate coefficients and a spin-lattice relaxation time are required. According to Chapter 3, no matter what strength of k_{ISL} is involved in the transition processes, time transients always possess double exponential

functions. We consider the solution shown in the previous chapter (eq. 3.23) as below,

$$\Delta PL/PL_0 = I_1 e^{-m_{12}t} + I_2 e^{-m_{22}t}$$

where $\Delta PL/PL_0$ is the change in PL, relative to the steady state value, I_1 and I_2 are prefactors of each exponential decay function, and m_{12} and m_{22} are the rate coefficients of fast and slow relaxing parts, respectively. Note that the prefactors and rate coefficients are functions of r_s, r_t, d_s, d_t, and k_{ISC}. They always show enhancement and quenching or vice versa, but their relative intensities and time constants are decided by contribution of all rate coefficients. If the intersystem crossing rate, $k_{ISC} = 1/T_{ISC}$, is much larger than other rate coefficients, the enhancement signal relaxes extremely fast, and its decay constant is dominantly determined by $1/T_{ISC}$. But when the quenching relaxes very slowly, the time transient shows a quick drop below zero after a pulse and slowly relaxes back to a steady state. As k_{ISC} becomes smaller, the enhancement signal relaxes slower, and, when k_{ISC} is very small so that it can be negligible, the behavior of time transient will be decided only by k_s, k_t, d_s, and d_t.

5.3 Finding a lower limit on the intersystem-crossing time from a pODMR transient

Fig. 5.2 shows the relative photoluminescence (PL) change $\Delta PL/PL_0$ in an MEH-PPV sample as a function of the time t, right after a 128 ns long microwave pulse with B_1=0.55 mT, at 10 K. An abrupt increase of the singlet pair density due to a resonant pulse results in the increase of the PL which quickly relaxes back to the steady state at around 200 μs. At some point, the increase changes into a quenching signal due to the prevalence of the slower relaxation of the triplet pair density. The experiments represented in Fig. 5.2 were repeated then inresonance (B_0=345.5mT) with a measured transient of 4ms.

Fig. 5.3 displays these data along with a fit result of a double exponential decay function which produced 107(1) μs and 840(20)μs for the fast and slow decay constants, respectively. This double exponential decay behavior is identical to the previously reported transients in many other organic [24–27] and inorganic semiconductors [28–34]. It confirms the intermediate pair model discussed intensively for pEDMR and pODMR experiments in Chapter 3. Applying the analytical solutions obtained in this chapter, the lower limit of the intersystem crossing time T_{ISC}=107(1) μs can be obtained.This is in agreement with the value extracted from cwODMR data by Yang et al. [35]. and another previously reported lower limit of 10 μs [36].

5.4 Polaron pair recombination dynamics in MEH-PPV

Fig. 5.4 displays the plot of the pODMR spectrum of MEH-PPV at 40 μs after a brief pulse was imposed onto the sample. Similar as for the pEDMR spectrum of MEH-PPV [26], the pODMR spectrum can be decomposed into two Gaussian peaks. These spectra cannot be fit with only either one Gaussian or with a Lorentzian peak. Both peaks have almost the same g-values, 2.0021(1) and 2.0018(2), respectively, but different peak width (FWHM) of 1.67(6) mT and 3.5(2) mT, respectively. The existence of these two peaks has been repeatedly confirmed before [1, 26, 27, 37–39]. Similar as in these previous studies, we assign these two peaks as distinct distributions belonging to two different pair-partners within the excitonic precursor pairs. It is not known though which peak corresponds to the electron and which to the hole. McCamey et al. have discussed this question with regard to pEDMR data [26]. Note that the experimental data of both pEDMR as well as pODMR spectra of MEH-PPV could also be fit excellently by three Gaussian peaks: One strong peak at symmetry center of the spectrum and two weaker satellites, with the same peak widths, intensities and separation from the spectral center. This fit approach corresponds to exchange coupled pairs, and it exhibited excellent agreement with both pEDMR and pODMR data. If this second scenario was correct, one would anticipate for spin-Rabi oscillation experiments a strong and B_1 field-independent presence of Rabi-beat oscillation [40] strength. In contrast to this expectation for strongly exchange coupled pairs, McCamey et al. found that any pEDMR observed beat oscillation was strongly B_1 dependent and thus, the fit with two Gaussians representing weakly coupled spin pairs is consistent with the observed data.

5.5 Optically detected spin Rabi nutations of weakly coupled spin pairs

In order to scrutinize the hypothesis that the ODMR detected signals in MEH-PPV originate from the same processes as previously detected EDMR detected signals, spin-Rabi oscillation was measured for a variety of microwave field strength. The goal of these measurements was to verify that for weak B_1-fields, only a spin $s = 1/2$ nutation was detectable in order to confirm the weakly spin-spin coupled character of the excitonic precursor pairs. Previous cwEDMR and cwODMR studies have arrived at this conclusion based on the observation of g-factors around 2 that only weakly coupled spins with $s = 1/2$ are involved in these processes [1, 37–39]. However, it is possible that spin resonances appear at the same g-factor in presence of, for instance strong exchange coupling.

When B_1 is smaller than the Larmor separation (= difference of Larmor frequencies in the pair), a Rabi nutation with frequency γB_1 (γ = gyromagnetic ratio) is expected for weakly coupled spin pairs. When B_1 exceeds the Larmor separation, both pair partners nutate and the observed Rabi frequency will double due to a beating effect within the spin system [23, 40, 41]. In contrast, when a pair is strongly spin-spin coupled, the presence of a beat signal is expected under any applied B_1. Thus, measuring the B_1-dependence allows the discrimination between spin-pairs whose coupling strength exceeds an applied B_1 field or not. In MEH-PPV, the Larmor separation within the excitonic precursor pairs is determined by hyperfine coupling and, thus, it is broadly distributed. For a pODMR detected nutation signal, this means that there will always be the γB_1-nutation signal as well the $2\gamma B_1$ beat signal at the same time. However, with increasing B_1-field, the nutation component will decrease in intensity while the beat component will rise.

The pulse length dependencies of spin Rabi nutations were measured by integrating the enhancement part of the pODMR transient over 16 μs at B_1=0.55 mT. The fast Fourier transformation of these data, FFT[N(τ)](B$_0$), is plotted in Fig. 5.5(a) and (b) for different B_1-fields, respectively. In Fig. 5.5 (a), a signal is present at B_0= 345.5 mT and f_{Rabi}=16(1) MHz. Fig. 5.5(a) also shows a hyperbola structure (white curve) that represents the values of Rabi's frequency formula [23],

$$2\pi f_{Rabi,i} = \sqrt{(\gamma_i B_1)^2 + (\gamma_i B_0 - 2\pi f_{mw})^2}$$

where $2\pi f_{Rabi,i}$ is the Rabi frequency of one pair partner, B_0 the resonance field of the excited spin, γ_i the gyromagnetic ratio, and f_{mw} is the frequency of the microwave. When the Larmor separation is larger than B_1, one of pair partners will have the Rabi frequency of $\gamma_i B_1$ at $\gamma_i B_0 = 2\pi f_{mw}$ while the other one has a frequency a little larger than $\gamma_j B_1$ due to the offresonance contribution, $(\gamma_j B_0 - 2\pi f_{mw})^2$. For small Larmor separation, both pair partners can be flipped together so that they form one two-spin system and a beat frequency appears with $2\pi f_{Rabi,beat} = 2\pi f_{Rabi,i} \pm 2\pi f_{Rabi,j} \simeq 4\pi f_{Rabi,i}$ or 0 because their g-values are almost the same. The expected beat frequencies for small Larmor separation as a function of B_0 are shown as white dotted curve in Fig. 5.5(a).

When an ensemble of spins contributes to an observed Rabi-oscillation and g-values are very homogeneous (the g-distribution is a delta-function), the Rabi-frequency versus B_0-field plot should follow Rabi's frequency formula [40–42]. In contrast, when the g-distribution is very broad due to disorder,the Rabi-frequency pattern is "smeared out" and the Rabi frequency will not follow Rabi's frequency formula anymore. Instead, it is pinned at γB_1 throughout the resonant line [42]. This effect can be seen in Fig. 5.5 (a). The

hyperbola-like signal cannot be observed but instead, a broad signal around B_0=345.5 mT is seen with γB_1=97(1) MHz. Thus, the data in Fig. 5.5 (a) represent an ensemble with a broad distribution of Larmor frequencies.

As previously reported in numerical studies [40, 41], when two spins in a pair have a Larmor separation which is larger than γB_1, two distinguishable hyperbola-like signals appear which have a minimum Rabi frequency at $2\pi f_{Rabi} = \gamma B_1$, as shown in Fig. 2 (c) of Ref. [40] and Fig. 2.(a) iii) and iv) of Ref. [41]. For the data of Fig. 5.5 (a), the B_1 field strength is only 0.55 mT and the Larmor separation is 1.36(1) mT. Two hyperbola curves are not distinguishable in Fig. 5.5 (a). This is because the resolution of B_0 is limited by a few Gauss and also due to the inhomogeneous broadening.

The expectation value of the Larmor separation within the spin pairs can be calculated with,

$$|\Delta g| = \int \int_{-\infty}^{\infty} G_b(g_b^c, \delta g_b) G_n(g_n^c, \delta g_n) |g_b - g_n| dg_b dg_n \tag{5.1}$$

where G_b and G_n are Gaussian distribution functions, δg_b and δg_n are the FWHMs, g_b^c and g_n^c are the peak center positions of the spin pair partners for broad and narrow peaks, respectively. For the presented data, this calculation was done by plugging all parameters obtained from the peak fit results in Fig. 5.4. The results reveal $|\Delta g|$= 1.36(1) mT at X-band. This is larger than B_1=0.55 mT in Fig. 5.5 (a). Note that the beat frequency for small Larmor separation (see eq. 3.34) should be roughly 32 MHz, and the broad and "smeared out" signals can be found in the range from 28 MHz to 48 MHz in Fig. 5.5 (a). Even though the Larmor separation is still larger than the excitation bandwidth $2B_1$, FWHMs of the two peaks 1.67(6) and 3.5(2) mT are still larger than the Larmor separation. In spite of this, a nonnegligible number of pair partners still can be excited simultaneously by a small B_1 field. This is illustrated in Fig. 5.6 where δg is the correlation distance. It is assumed that the spectral data obtained from Fig. 5.4 are from noncorrelated spin pairs. If the spectral data obtained by pODMR are originated from correlated spin pairs, the calculation of $|\Delta g|$ is not possible as long as the correlation relation is not known. Thus we have to figure out if the spins in a pair in this sample are correlated.

It has been predicted that in spin ensembles where two correlated pair partners have broad Larmor frequency distributions, the spin beat signal intensity is always bigger than the spin one half signal as long as the spin distribution due to disorder is not infinitely broader than the applied B_1 field [42]. However, in the case of ensembles of noncorrelated spin pairs, the intensity of the spin beating signal is smaller than the spin one half signal

when the width of spin distribution is larger than B_1. This explanation is in agreement with the nonnegligible but very weak signals around the beat frequency in Fig. 5.5 (a).

It should be emphasized that if spins in a pair are strongly exchange coupled, the $2\gamma B_1$ signal will still appear at low B_1 fields. In contrast, if spin pairs are weakly coupled, the beat frequency is predicted to be larger than $2\gamma B_1$ [41] and the intensity is predicted to be small in disordered and noncorrelated systems at low B_1 fields [42]. Because of the limited frequency resolution in Fig. 5.5 (a), it is hard to identify the second harmonic component at the low B_1 field. Fig. 5.5 (b) shows the Fourier transform of spin-Rabi nutations, FFT[Q(τ)](B$_0$) as a function of B_0, for stronger B_1 (=1.5 mT). In contrast to the weakly coupled spins excited by small B_1 [Fig. 5.5 (a)], not only the γB_1 signal but also the $2\gamma B_1$ signal is visible. Here, B_1 is comparable to, or larger than, the calculated Larmor separation. A plot of the onresonance Rabi frequencies as a function of B_1 is shown in Fig. 5.5 (c). The solid blue line is a linear fit of γB_1 signals, and the blue dashed line is a guide to the eye for $2\gamma B_1$ signals. The linear slope of the maxima of the low frequency component signals is $1.77(1)\times\ 10^{11}$ $rad/T \cdot s$ which is in agreement with the measured gyromagnetic ratio, γ=$1.7607(3)\ \times\ 10^{11}$ $rad/T \cdot s$. At high B_1, the beat frequency is predicted to be close to $2\gamma B_1$ and the intensity of the signal will increases due to power broadening. This prediction is in agreement with the measured onresonance B_1 dependence of FFT[Q(τ)] as in Fig. 5.5 (c). In this figure, the spin one half components are always visible but the beat frequency components are visible only at large B_1 fields, and the corresponding beat frequencies are quite close to $2\gamma B_1$.

Based on the discussion above, it is concluded that excitonic precursor spin pairs found in MEH-PPV (the so called polaron pairs), are weakly spin-spin coupled and they have noncorrelated resonance frequencies. As shown in the following section, these properties can be used to explore the hyperfine interactions of polarons in this material.

5.6 Tuning hyperfine fields in organic semiconductor

Most investigations to date on spin-dependent processes in organic semiconductors have been carried out under static conditions, where it is not possible to coherently manipulate the spin orientations [1–14]. We recently reported applying pEDMR to OLEDs, which enables coherent manipulation of the spin polarization, leading to striking coherent features in macroscopic observables such as the device current [24, 26]. We now use this sensitive technique to correlate materials chemistry with intrinsic spin dynamics. However, instead of measuring a current we detect spin-dependent recombination by a change in PL intensity under resonance.

Fig. 5.7 (a), (b) illustrates our experimental approach. We measure the dynamics of electron and hole spins in a film of MEH-PPV. Optical excitation of the polymer leads to the formation of tightly-bound excitons, which subsequently decay under emission of a photon. However, a small percentage of these excitons may dissociate to form electrostatically-correlated weakly spin-spin coupled electron-hole pairs which typically reside on different chains in the bulk film. We can tune the local hyperfine field by varying the side groups of the polymer backbone (marked in green). Under electron spin resonance (ESR) conditions, a spin flip occurs within the carrier pair, shuttling it reversibly between the singlet and triplet spin manifold. For reasons of energy conservation and wavefunction symmetry, it is easier for a carrier pair in the singlet configuration to form a singlet exciton than for a triplet pair to relax to a triplet exciton [7]: Carrier recombination is spin-dependent and can be monitored by recording the singlet exciton PL yield [13].

5.7 Spin beating induced by hyperfine interaction

The resonance condition can occur either for an individual charge or for both spins together, depending on the intrinsic ESR linewidth of each carrier. The hyperfine field, the random magnetic field originating primarily from the hydrogen nuclei in the polymer, constitutes the dominant ESR line broadening mechanism [1]. As electron and hole wavefunctions need not have precisely the same shape on a polymer chain, it is unlikely that both carrier types will experience the same hyperfine field strength [26]. The hyperfine broadening of the resonance must be seen in conjunction with the intensity of the microwave field, which itself contributes a time-varying magnetic field B_1. Once B_1 exceeds the difference in hyperfine field strengths acting on the two carriers, electron and hole resonances become indistinguishable and both carriers experience resonance. This situation is sketched in panels c), d) of Fig. 5.7: at low driving fields (microwave intensities), only one carrier spin precesses, leading to a spin- type resonance. As the B_1 amplitude is raised to exceed the difference in local hyperfine field of electron and hole, the two spins precess together. The nutation frequency between singlet and triplet configurations is doubled: spin beating occurs.

We recently described this effect in EDMR [26]. Identical behavior is observable here using optical detection, as illustrated in panels e) and f). Such ODMR is much simpler to perform than EDMR as it does not require the incorporation of conductive leads into the ESR resonator, which can potentially distort the local microwave field. A drop-cast sample mounted in a cryostat at 15 K was excited using a c.w. laser at 488 nm, and the PL was

detected by a silicon photodiode. The inset of Fig. 5.7 (e) shows the dependence of the differential PL on the duration of the microwave pulse. As the pulse length is increased, the electron or hole spin precesses further, generating a triplet carrier pair from a singlet carrier pair, and vice versa. This precession leads to an oscillation in the singlet and triplet population density with pulse length, giving rise to Rabi flopping in the PL intensity. The curve can be accurately fit by a single-frequency transient function [23] as will be explained later. The Fourier transformation, the green curve in the main panel of Fig. 5.7 (e), of the time dependent data as well as a fit with two Fourier transformed transient functions (red, blue) reveals only a single frequency component, as expected for a spin-1/2 resonance. At high microwave powers, panel (f), the Rabi frequency increases (inset). In addition, now both the Fourier analysis of the data and the fit to both the time domain and frequency domain data reveal a distinct harmonic component to the resonance: spins either precess on their own or together. The fit curves (green, blue, and red) in Fig. 5.7 (e), (f) are obtained not only to separate two Rabi nutation curves from experimental data but also to quantify the contributions of each curves. These quantities are later used to estimated the difference in hyperfine field experienced by electron and hole.

The fit curves in Fig. 5.7 (e), (f) are obtained as follows. Optically-detected spin Rabi nutation under the influence of inhomogeneity in the spin distribution can be described by the transient function, introduced in previous chapter (eq. 3.35), derived originally in Ref. [23]. Let's recall this function as below

$$\Delta^{\text{eff}} = \int_{-\infty}^{\infty} \Phi(\omega_L) \frac{\gamma^2 B_1^2}{\gamma^2 B_1^2 + (\omega - \omega_L)^2} \sin^2(\kappa\tau\sqrt{\gamma^2 B_1^2 + (\omega - \omega_L)^2}) d\omega_L \tag{5.2}$$

where τ is the length of the resonant pulse radiation, κ becomes 1/2 for large Larmor separation and 1 for small larmor separation, and $\Phi(\omega_L)$ represents the Landé g-factor distribution. $\Phi(\omega_L)$ can be replaced, if we assume that electron-hole pairs are weakly coupled and noncorrelated, by the superposition of two Gaussian density distribution functions of which peak parameters, widths and center positions, are obtained from the resonance lines in Fig. 5.8 (c) and (d). Note that Fig. 5.8 (c) is the same as Fig. 5.4. Exact values for B_1 could be obtained from the Rabi frequencies of spin-1/2 nutation components of fast Fourier transformed spin Rabi nutations. Note that this function should be used as a fit function for the data collected at high microwave power, and this can be approximated to the integral of zeroth order first-kind Bessel function at low microwave power [25]. For data analysis in time domain spectroscopy, the obtained raw data transients were Fourier transformed and the resulting frequency domain data are then subjected to fits with Fourier transformed transients, obtained from eq. 5.2, for a quantitative analysis of the different

oscillation components. As a control procedure, we also carried out direct fits of the time domain data (the raw data) with eq. 5.2, for the two known harmonic components which led to identical results for the fraction of spins.

Practical challenges for the fit process arise because of the limited frequency resolution and limited sampling rate. The frequency resolution is determined by the longest pulse duration, 498 ns in this experiment. This definite value for the longest pulse length increases the uncertainties in the fit results. In addition, all sampled data with a finite sampling rate are band-limited and this is usually negligible as long as the sampling rate is faster than Nyquist rate [43]. Note that the Nyquist frequency is the double of the highest frequency of a nonzero signal of the real transient. If the spin Rabi nutation transient arises from nonpower broadened isolated single spins, it can be described by a simple harmonic function. In this case, full recovery of the real transient is possible as long as the sampling frequency is larger than twice the most dominant harmonic frequency because the simple harmonic function consists of only a single frequency component. However, the real Rabi nutations in our sample were influenced by power broadening, and in addition the transient function is not a simple harmonic function: this function consists of a dominant harmonic component and other components in a wide frequency range. Because of this situation, the required Nyquist rate should be orders of magnitude higher than both the nutation and beat frequencies, which is experimentally not implementable. Refer to Fig. 3.7. To overcome this problem, the experimental data were fit with a frequency-resolution-limited and band-limited fit function using a 4 ns sampling time (as used for the data collection) and limiting the longest pulse lengths to the real values.

In Fig. 5.7 (e) and (f), plots are presented of Fourier transforms of the raw data, along with the fit result for two peaks as well as the two individual fit components. The fit function shows an excellent agreement with the Fourier transform of the experimental data. As mentioned above, fitting the time domain data directly leads to identical fit results for the magnitude of both oscillation components (for both the absolute values as well as their errors) compared to the fits of the Fourier transformed raw data.

5.8 Effect of deuteration on $|B_{hyp}|$

The magnitude of the microwave field at which the beat oscillation signal dominates provides an estimate of the difference in hyperfine field experienced by electron and hole, $|B_{hyp}|$. This value can also be estimated by fitting to the resonance lines [26] as long as hyperfine fields within the individual pairs are not correlated. However, without a route to

direct control of the hyperfine field, a model fit alone is not sufficient proof that the intrinsic spin properties really are dominated by nuclear fields: other broadening mechanisms such as spin-orbit coupling or dipolar interactions could also contribute. To conclusively probe for hyperfine effects, we compare conventional MEH-PPV to a deuterated compound in Fig. 5.8. Here, only the polymer side groups are deuterated (panels a, b). The differential PL in panels c) and d) can be described by a superposition of two Gaussians, attributed to electron and hole carrier spin-1/2 resonances [26]. As expected, the resonance is narrower for the deuterated compound with a smaller hyperfine coupling constant [19]. From the line fits we extract $|B_{hyp}|$=1.36(1) mT (1.31(3) mT) for the hydrogenated (deuterated) sample. With such a small difference, it is difficult to confirm, based on linewidth change alone, that deuteration really influences $|B_{hyp}|$. However, the direct time-domain analysis of hyperfine-field-mediated spin beating, which is not prone to error by hyperfine field correlation between the two pair partners, provides clear support for the influence of deuteration(supporting info). Fig. 5.8 (e), (f) plots the fractions of the numbers of spin pairs that produce beat oscillation signals (red) and pure spin-1/2 nutation signals (blue) for both materials, extracted from the Rabi-flopping curves like Fig. 5.7 (e), (f). Those fractions were obtained as follows.

The goal of the experiments presented is to measure the ratio of the number I_{beat} of spin pairs which produce an optically detectable spin-beating signal and the number I_{nut} of spin pairs which produce optically detectable spin-1/2 Rabi nutations for a given applied microwave power. This ratio is referred to as "ratio of spins" or 'fraction of spins'

$$fraction = \frac{2 \times I_{beat}}{I_{nut} + 2 \times I_{beat}} \tag{5.3}$$

where the factor 2 arises because the beating signal requires twice as many spins to nutate for the same signal intensity as a spin-1/2 nutation signal [23, 41].

For a given pair of two spins with s=1/2, B_1 and the difference of the pair partners' Larmor frequencies $\Delta\omega$ determine whether the pairs' spin-dependent decay probability will oscillate with Ω_n or Ω_b, called the nutation and beat frequencies, respectively. When $B_1 < \Delta\omega$, spin 1/2 Rabi nutation will take place. When $B_1 > \Delta\omega$, beat oscillations will become dominant [41]. Since $\Delta\omega$ is randomly distributed due to the hyperfine fields, a measurement of the ratio of spins as a function of B_1 reveals information about the expectation value of the difference of the hyperfine fields $|B_{hyp}|$ which is equal to B_1 when $I_{beat} = I_{nut}$ [26]. In order to determine the ratio of spins experimentally, transient nutation data must be analyzed with regard to the two harmonic components with frequency ratio $\Omega_b/\Omega_b = 2$. The obtained crossover point through this procedure (1.38(10) mT hydrogenated; 1.15(8) mT

deuterated; confidence level 95%) in Fig. 5.8 (e), (f) reveals a significant difference between the two materials.

Values are derived for $|B_{hyp}|$ for the protonated and deuterated MEH-PPV. For each material, two values are obtained, one from line-shape analysis and one from the spin-beat signals. The $|B_{hyp}|$ obtained from the line shape analysis is an estimate based on the assumption that the Larmor separation of the spin pairs is determined by two independent Gaussian probabilities that are described by the resonance lines shown in Fig. 5.8 (c),(d) [see Supporting Information of Ref. [26]]. This assumption may be wrong and if so, the inaccurate value obtained from the spectral data may be different from the true value. This deviation is part of the problem of using simple ODMR spectra (continuous wave or pulsed) for the determination of hyperfine field strengths, as is commonly done [19]. In contrast, if a correlation exists between the Larmor frequency distributions of the two pair partners (the electron and hole polarons), the spin-beat experiment will accurately reflect this. Thus, when the spin-beat experiment reveals lower values for than the spectral data as is the case in our study, the spin-beat data must be correct and therefore provides evidence that some correlation between the Larmor frequencies of the two individual charge carriers exists.

5.9 Conclusion

Deuteration of the polymer reduces the hyperfine field [19–21] so that electron and hole experience simultaneous resonance at lower microwave intensities. Thus, a sample in which line broadening is not dominated by hyperfine fields should display spin beating even at low microwave driving fields. As a next step, the entire backbone of the polymer should be deuterated, and the effect of symmetric versus asymmetric backbone substitution explored. Suffice to note that the present effect of deuteration ($\sim 20\%$ change) is significantly weaker than expected for an isotropic system. A quantitative comparison of the hyperfine effects seen here and in the recent study by Nguyen et al. [19] is not possible since exact charge carrier wavefunctions are not known in either one of the materials. In our study, the sidegroups were deuterated and not the backbone, whereas Ref. [19] reports deuteration of the backbone alone. The carriers appear to only weakly penetrate the sidegroups. Controlled deuteration thus offers a route to map the location and extent of the carrier wavefunction.

5.10 Acknowledgement

Acknowledgment is made to the DoE (Grant DESC0000909) and the donors of the American Chemical Society Petroleum Research Fund (Grant PRF 48916-DNI10) for sup-

port of this research. C.B. thanks the NSF for a CAREER Award (No. 0953225). P.L.B. is recipient of an Australian Research Council Federation Fellowship (No. FF0668728), and J.M.L. is a David and Lucile Packard Foundation Fellow. S.-Y. Lee thanks Kipp J. van Schooten for sample preparation and cooperation in pODMR experiments, and William J. Baker for cooperation in pODMR experiments.

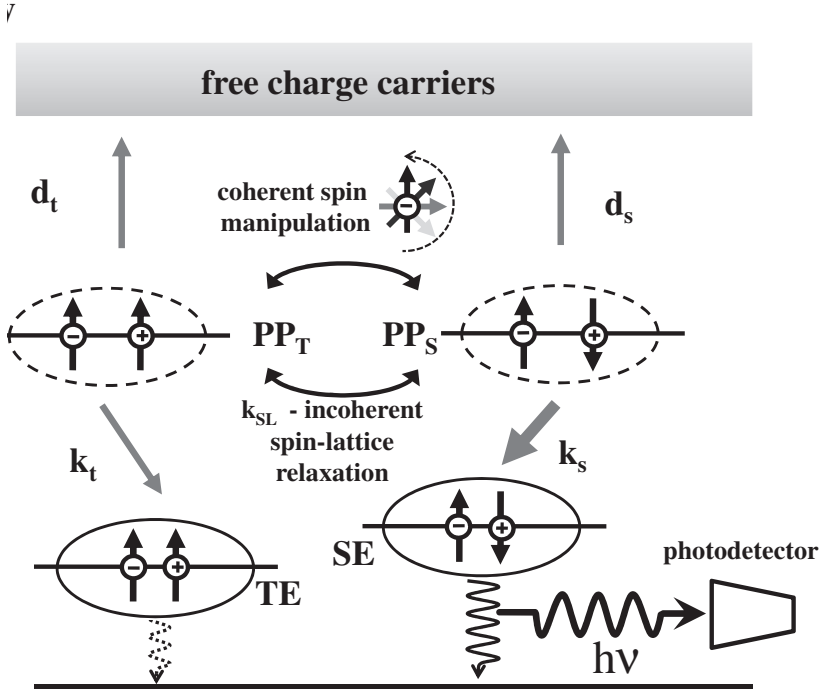

Figure 5.1. Illustration of spin-dependent excitonic charge carrier recombination in organic semiconductors. Upon encounter, electrons and hole (which are usually polaronic states) form weakly spin- but strongly Coulomb-coupled intermediate pairs. The pairs can exist in parallel and antiparallel configurations with pure triplet character or singlet/triplet mixtures, respectively. Triplet polaron pair will either thermally dissociate or recombine into triplet excitons. Singlet state will either dissociate at a different dissociation rate or recombine into singlet states. Changes of the precursor spin states with magnetic resonance can change netdissociation or netrecombination rates, which then influence conductivity or optical emission, respectively.

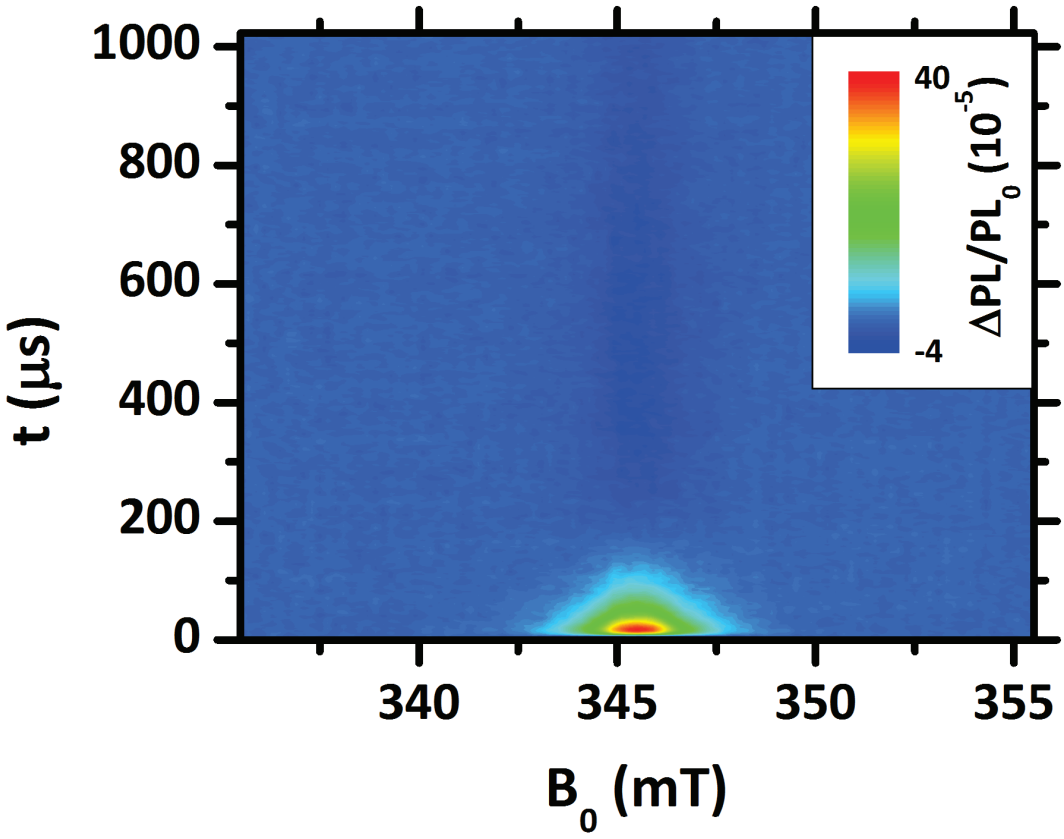

Figure 5.2. Photoluminescence change of MEH-PPV as a function of the time after a short (128ns) microwave pulse and a function of the magnetic field B_0. One can recognize an enhancement signal right after pulse for magnetic fields around B_0=345.5mT followed by slowly relaxing weak quenching signal.

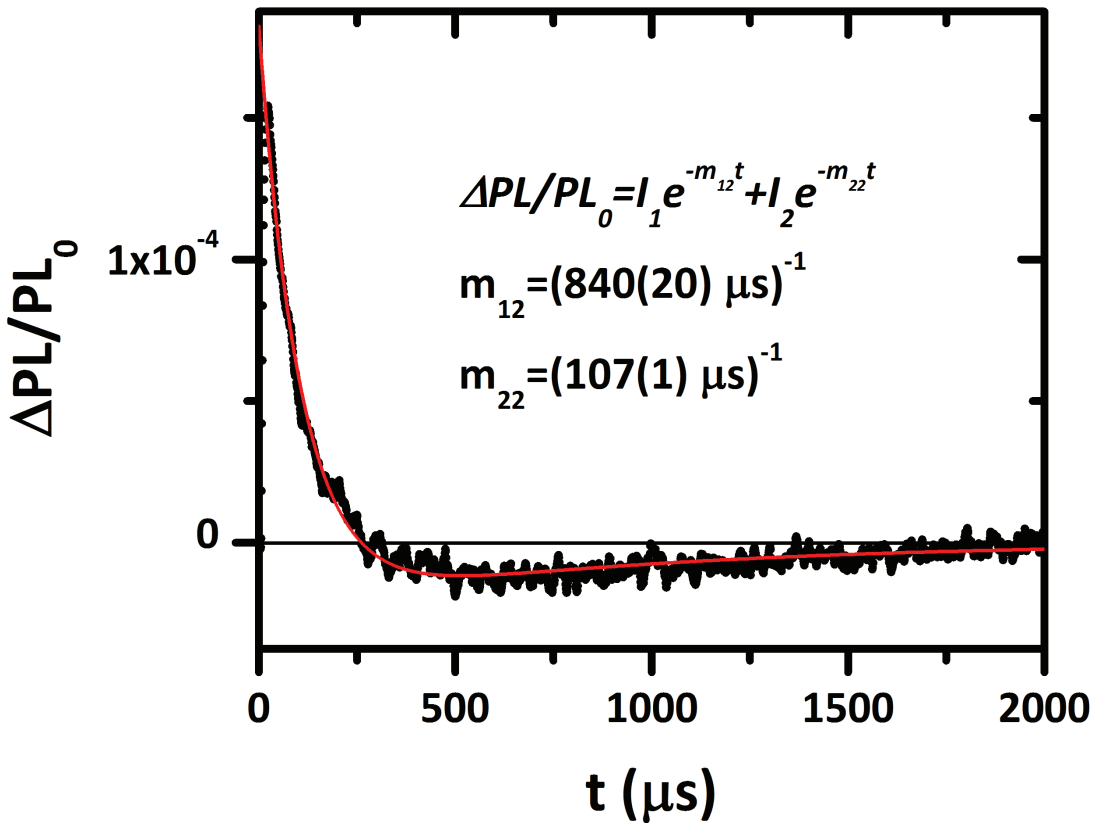

Figure 5.3. Transient behavior of PL change at onresonance B_0 fields, 345.5 mT. Double exponential function can explain enhancement-quenching behavior very well and two time constants can be extracted.

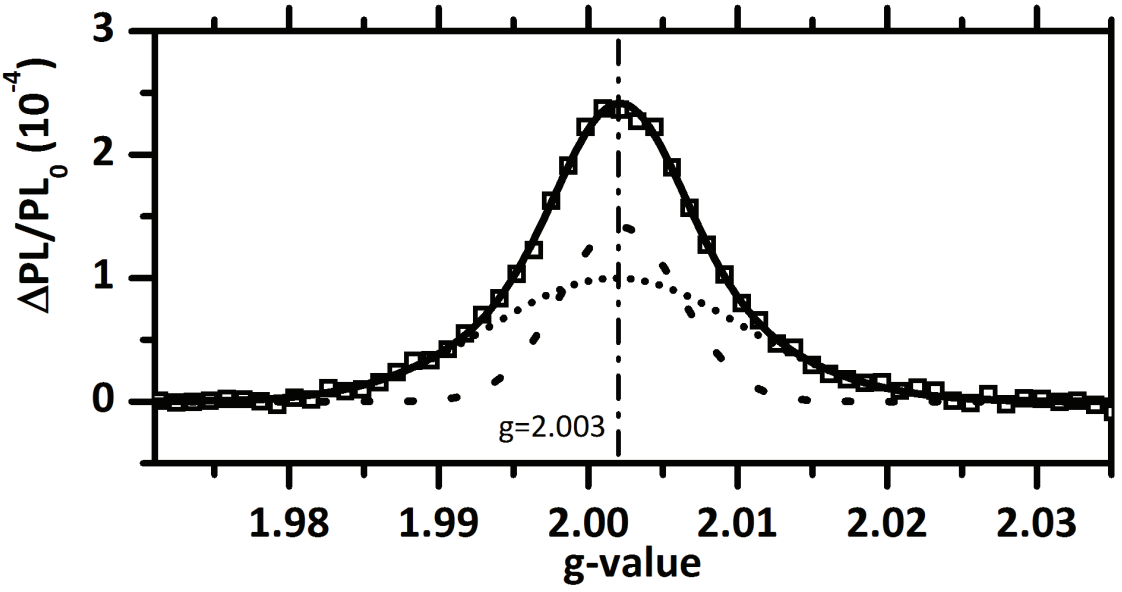

Figure 5.4. PODMR spectrum obtained at a time $t = 40\,\mu$s after a pulsed excitation of MEH-PPV with the magnetic field expressed as g-values. A fit function consisting two Gaussian peaks, one narrow(FWHM=1.68(6) mT) and the other broad(FWHM=3.6(1) mT), is in good agreement with the data. For details see text.

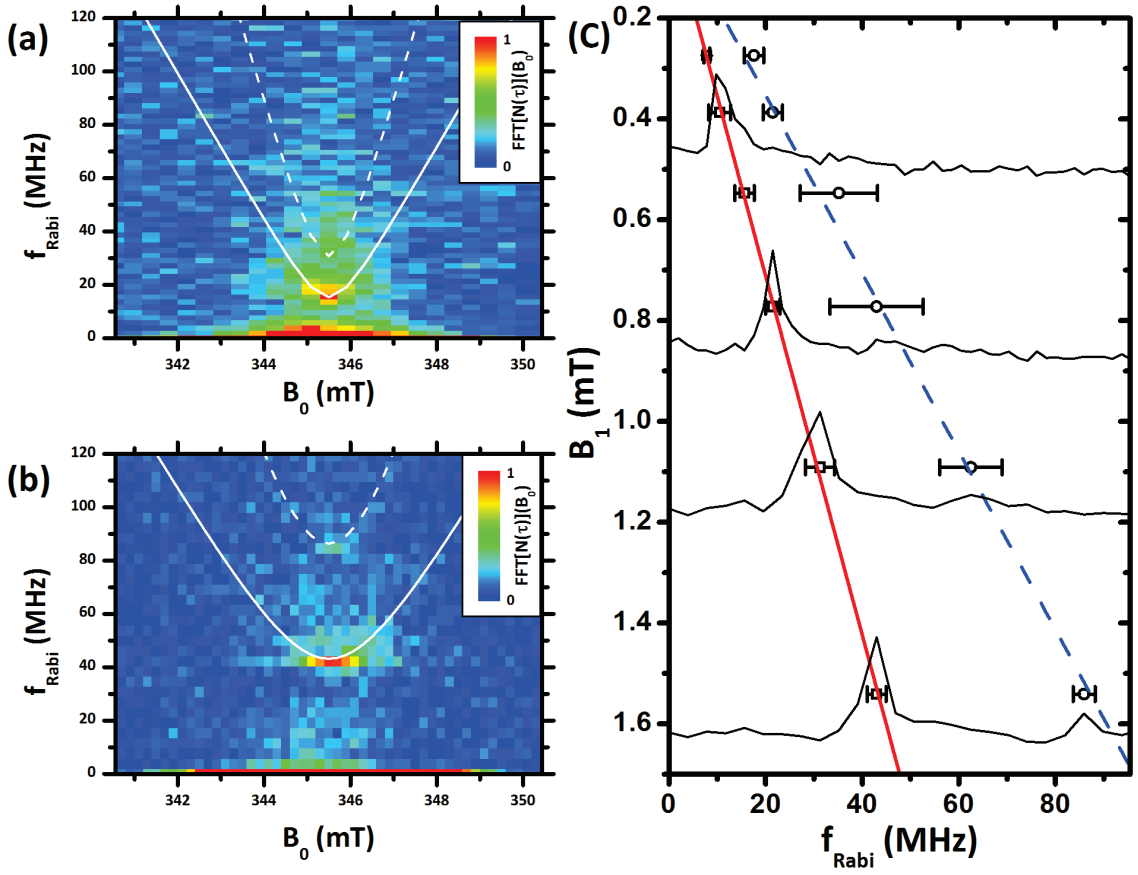

Figure 5.5. Intensity of pODMR signals of MEH-PPV as a function of the applied B_0 and spin-frequency. The displayed data are obtained from a FFT[N(τ)](B_0) of a pulse length dependence measurement. The measurements were carried out at (a) at B_1=0.55 mT and (b) at B_1=1.54 mT. (c) FFT of opticalled detected Rabi nutations at an on resonance B_0 field measured at various B_1 strengths. The curves in (a) and (b) are predictions of Rabi frequencies (solid) and spin Rabi-beat frequencies (dotted) as a function of B_0, based on Rabi-frequency formula (see Chapter 3). The red solid line in (c) is the linear fit of $2\pi f_{Rabi}$ vs. B_1 whose slope is 1.77×10^{11} rad/sT. This is very close to the gyromagnetic ratio. The blue dashed line is a guide to the eye showing $2\pi f_{Rabi} = 2\gamma B_1$.

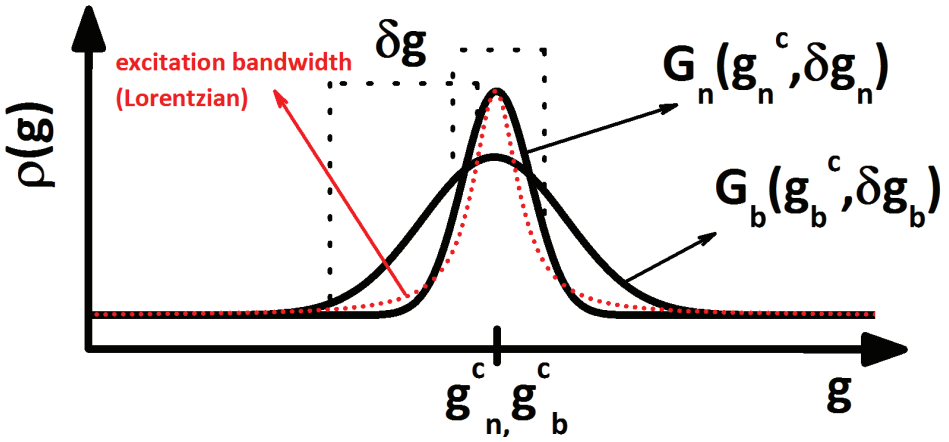

Figure 5.6. Larmor frequency distribution of noncorrelated spin pair partners expressed in g-factors. g_n^c and g_b^c are Landé g-factors of the narrow and broad peaks, respectively, and, δg_n and δg_b are the FWHM of two peaks, respectively. δg is the correlation length. The red dotted curve indicates the excitation bandwidth determined by the B_1 field strength.

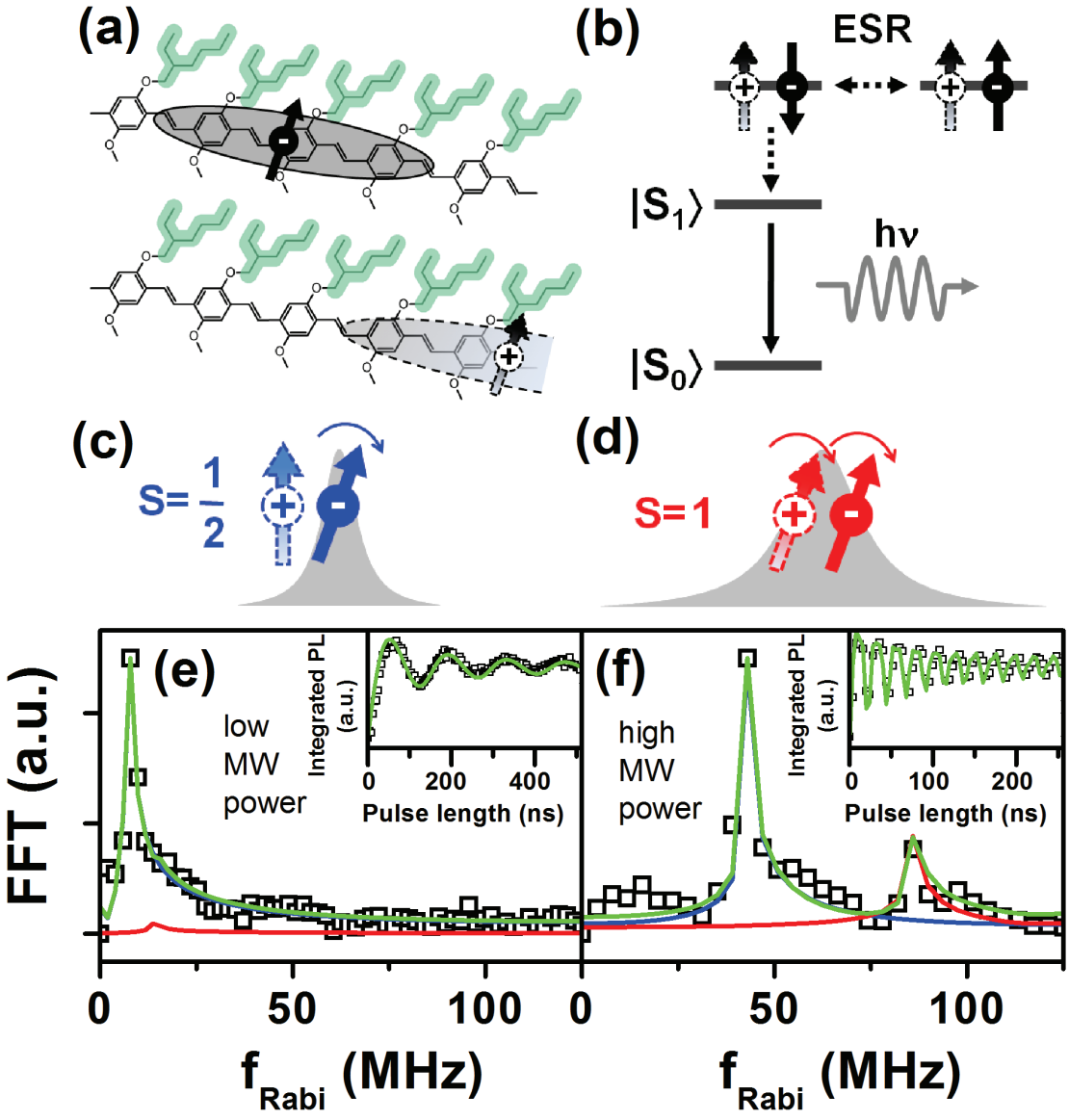

Figure 5.7. Coherent spin manipulation in organic semiconductors monitored by PL-detected spin resonance. (a) Charge carrier pairs are formed in MEH-PPV by optical excitation. (b) Under spin resonance conditions, a spin flip can occur, which is recorded by a change in singlet exciton emission intensity. (c) At low microwave intensities, only one spin precesses at a time, whereas both spins precess together at high intensities (d). (e) Inset: Rabi flopping in the polymer PL is dominated by a single frequency component at low intensities as shown by the Fourier transform in the main plot (X-band 9.8 GHz radiation). (f) At high intensities, spin beating occurs, leading to a harmonic appearing in the Fourier transform. The green lines in the time domain and frequency domain plots correspond to fits of the experimental raw data and its Fourier transform, respectively. Blue lines show the fundamental contribution in the oscillation, red lines indicate the beat signal. The data analysis procedure is outlined in main text.

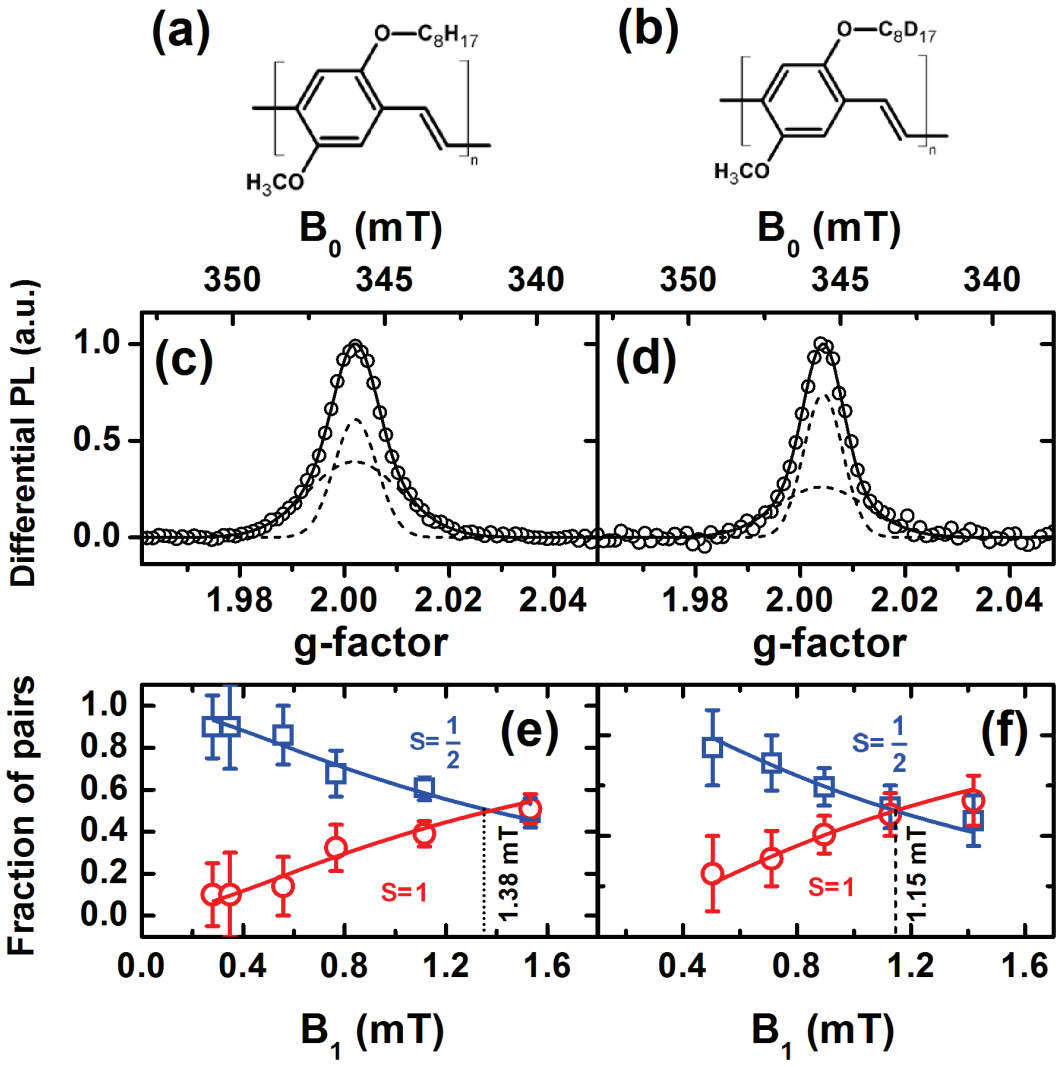

Figure 5.8. Effect of deuteration of the polymer side groups on the ODMR resonance spectrum and on spin beating [cf. Fig. 5.7 (f)]. (a), (b) Structures of the polymers studied. (c), (d) The differential PL resonance spectrum is accurately described by a superposition of two Gaussians, representing electron and hole resonances. (e), (f) Fourier analysis of the beating transients [see Fig. 5.7 (e), f)] allows the extraction of the spin-1 and spin- contributions to the resonance. The crossing point of the two as a function of microwave field strength B1 offers an estimate of the difference in local hyperfine fields experienced by a carrier pair. The dotted curves in (e) are the predictions. See details in text.

5.11 References

[1] F. A. Castro, G. B. Silva, L. F. Santos, R. M. Faria, F. Nüesch, L. Zuppiroli, and C. F. O. Graeff. *Journal of Non-Crystalline Solids*, 338-340:622–625, 2004.

[2] V. Dyakonov, G. Rösler, M. Schwoerer, and E. L. Frankevich. *Physical Review B*, 56:3852, 1997.

[3] S. Kuroda, K. Marumoto, N. C. Greenham, R. H. Friend, Y. Shimoi, and S. Abe. *Synthetic Metals*, 119:655–656, 2001.

[4] P. A. Lane, X. Wei, and Z. V. Vardeny. *Physical Review B*, 56:4626, 1997.

[5] L. S. Swanson, J. Shinar, and K. Yoshino. *Physical Review Letters*, 65:1140, 1990.

[6] M. Segal, M. A. Baldo, M. K. Lee, J. Shinar, and Z. G. Soos. *Physical Review B*, 71:245201, 2005.

[7] M. Wohlgenannt, C. Yang, and Z. V. Vardeny. *Physical Review B*, 66:4, 2002.

[8] E. L. Frankevich, A. A. Lymarev, I. Sokolik, F. E. Karasz, S. Blumstengel, R. H. Baughman, ouml, and H. H. rhold. *Physical Review B*, 46:9320, 1992.

[9] J. Kalinowski, M. Cocchi, D. Virgili, P. Di Marco, and V. Fattori. *Chemical Physics Letters*, 380:710–715, 2003.

[10] T. L. Francis, O. Mermer, G. Veeraraghavan, and M. Wohlgenannt. *New Journal of Physics*, 6:185, 2004.

[11] F. Ito, T. Ikoma, K. Akiyama, A. Watanabe, and S. Tero-Kubota. *The Journal of Physical Chemistry B*, 109:8707–8717, 2005.

[12] M. Reufer, M. J. Walter, P. G. Lagoudakis, A. B. Hummel, J. S. Kolb, H. G. Roskos, U. Scherf, and J. M. Lupton. *Nature Materials*, 4:340 – 346, 2005.

[13] Y. Sheng, T. D. Nguyen, G. Veeraraghavan, Mermer, Ouml, M. Wohlgenannt, S. Qiu, and U. Scherf. *Physical Review B*, 74:045213, 2006.

[14] J. M. Lupton and C. Boehme. *Nature Materials*, 7:598–598, 2008.

[15] M. Segal, M. A. Baldo, R. J. Holmes, S. R. Forrest, and Z. G. Soos. *Physical Review B*, 68:075211, 2003.

[16] U. E. Steiner and T. Ulrich. *Chemical Reviews*, 89:51–147, 1989.

[17] V. A. Dediu, L. E. Hueso, I. Bergenti, and C. Taliani. *Nature Materials*, 8:707–716, 2009.

[18] Z. H. Xiong, D. Wu, Z. Valy Vardeny, and J. Shi. *Nature*, 427:821–824, 2004.

[19] T. D. Nguyen, G. Hukic-Markosian, F. Wang, L. Wojcik, X.-G. Li, E. Ehrenfreund, and Z. V. Vardeny. *Nature Materials*, 9:345–352, 2010.

[20] N. J. Rolfe, M. Heeney, P. B. Wyatt, A. J. Drew, T. Kreouzis, and W. P. Gillin. *Physical Review B*, 80:241201, 2009.

[21] W. J. Mitchell, P. L. Burn, R. K. Thomas, G. Fragneto, J. P. J. Markham, and I. D. W. Samuel. *Journal of Applied Physics*, 95:2391–2396, 2004.

[22] D. Kaplan, I. Solomon, and N. F. Mott. *J. Physique Lett.*, 39:51–54, 1978.

[23] C. Boehme and K. Lips. *Physical Review B*, 68:245105, 2003.

[24] D. R. McCamey, H. A. Seipel, S.-Y. Paik, M. J. Walter, N. J. Borys, J. M. Lupton, and C. Boehme. *Nature Materials*, 7:723, 2008.

[25] W. Harneit, C. Boehme, S. Schaefer, K. Huebener, K. Fostiropoulos, and K. Lips. *Physical Review Letters*, 98:216601, 2007.

[26] D. R. McCamey, K. J. v. Schooten, W. J. Baker, S.-Y. Lee, S.-Y. Paik, J. M. Lupton, and C. Boehme. *Physical Review Letters*, 104:017601, 2010.

[27] C. Boehme, D. R. McCamey, K. J. v. Schooten, W. J. Baker, S.-Y. Lee, S.-Y. Paik, and J. M. Lupton. *Physica Status Solidi (b)*, 246:2750, 2009.

[28] A. R. Stegner, C. Boehme, H. Huebl, M. Stutzmann, K. Lips, and M. S. Brandt1. *Nature Physics*, 2:835, 2006.

[29] C. Boehme and K. Lips. *Journal of Materials Science: Materials in Electronics*, 18:S285–S291, 2007.

[30] C. Boehme, F. Friedrich, T. Ehara, and K. Lips. *Thin Solid Films*, 487:132, 2005.

[31] C. Boehme and K. Lips. *Physica Status Solidi (c)*, 1:1255 – 1274, 2004.

[32] S. Y. Paik, S. Y. Lee, W. J. Baker, D. R. McCamey, and C. Boehme. *Physical Review B*, 81:075214, 2010.

[33] T. W. Herring, S.-Y. Lee, D. R. McCamey, P. C. Taylor, K. Lips, J. Hu, F. Zhu, A. Madan, and C. Boehme. *Physical Review B*, 79:195205, 2009.

[34] J. Behrends, A. Schnegg, C. Boehme, S. Haas, H. Stiebig, F. Finger, B. Rech, and K. Lips. *Journal of Non-Crystalline Solids*, 354:2411–2415, 2007.

[35] C. G. Yang, E. Ehrenfreund, M. Wohlgenannt, and Z. V. Vardeny. *Physical Review B*, 75:5, 2007.

[36] D. R. McCamey, S. Y. Lee, S. Y. Paik, J. M. Lupton, and C. Boehme. *Physical Review B*, 82:125206, 2010.

[37] J. D. Ceuster, E. Goovaerts, A. Bouwen, J. C. Hummelen, and V. Dyakonov. *Physical Review B*, 64:195206, 2001.

[38] K. Murata, Y. Shimoi, S. Abe, S. Kuroda, T. Noguchi, and T. Ohnishi. *Chemical Physics Letters*, 227:191–201, 1998.

[39] G. B. Silva, L. F. Santos, R. M. Faria, and C. F. O. Graeff. *Physica B: Condensed Matter*, 308-310:1078–1080, 2001.

[40] A. Gliesche, C. Michel, V. Rajevac, K. Lips, S. D. Baranovskii, F. Gebhard, and C. Boehme. *Physical Review B*, 77:245206, 2008.

[41] V. Rajevac, C. Boehme, C. Michel, A. Gliesche, K. Lips, S. D. Baranovskii, and P. Thomas. *Physical Review B*, 74:245206, 2006.

[42] C. Michel, A. Gliesche, S. D. Baranovskii, K. Lips, F. Gebhard, and C. Boehme. *Physical Review B*, 79:052201, 2009.

[43] R. J. Marks. *Introduction to Shannon sampling and interpolation theory.* Springer texts in electrical engineering. Springer-Verlag, New York, 1991.

LIST OF PUBLICATIONS

Publications first-authored by the author

Understanding the modulation frequency dependence of continuous wave optically/electrically detected magnetic resonance
S.-Y. Lee, S.-Y. Paik, D. R. McCamey, and C. Boehme
in preparation.

Tuning hyperfine fields in conjugated polymers for coherent organic spintronics
S.-Y. Lee, S.-Y. Paik, D. R. McCamey, J. Yu, P. L. Burn, J. M. Lupton and C. Boehme
J. Am. Chem. Soc. **133**, 072019 (2011). http://dx.doi.org/10.1021/ja108352d

Spin-dependent processes in amorphous silicon-rich silicon-nitride
S.-Y. Lee, S.-Y. Paik, D. R. McCamey, J. Hu, F. Zhu, A. Madan, and C. Boehme
Appl. Phys. Lett. **97**, 192104 (2010). http://dx.doi.org/10.1063/1.3509406

Publications co-authored by the author

Spin-dependent dynamics of polaron pairs in organic semiconductors
D. R. McCamey*, S.-Y. Lee*, S.-Y. Paik, J. M. Lupton, and C. Boehme
Phys. Rev. B **82**, 125206 (2010). (∗corresponding authors)
http://dx.doi.org/10.1103/PhysRevB.82.125206

Hyperfine-field mediated spin beating in electrostatically-bound charge carrier pairs
D. R. McCamey, K. J. van Schooten, W. J. Baker, S.-Y. Lee, S.-Y. Paik, J. M. Lupton, and C. Boehme
Phys. Rev. Lett. **104**, 017601 (2010). http://dx.doi.org/10.1103/PhysRevLett.104.017601

Pulsed electrically detected magnetic resonance in organic semiconductors
C. Boehme, D. R. McCamey, K. J. van Schooten, W. J. Baker, S.-Y. Lee, S.-Y. Paik, J. M. Lupton
Phys. Stat. Sol B. **246**, 11-12, 2750 (2009). http://dx.doi.org/10.1002/pssb.200982357

Experimental discrimination of geminate and non-geminate recombination in a-Si:H
T. W. Herring, S.-Y. Lee, D. R. McCamey, P. C. Taylor, K. Lips, J. Hu4 F. Zhu, A. Madan, and C. Boehme
Phys. Rev. B **79**, 195205 (2009). http://dx.doi.org/10.1103/PhysRevB.79.195205

Crystal orientation induced spin Rabi beat oscillations of point defects at the c-Si(111)/SiO_2 interface
S.-Y. Paik, S.-Y. Lee, D. R. McCamey, and C. Boehme
in preparation.

T_1- and T_2-spin relaxation time limitations of phosphorous donor electrons near crystalline silicon to silicon dioxide interface defects

S.-Y. Paik, S.-Y. Lee, W. J. Baker, D. R. McCamey, and C. Boehme
Phys. Rev. B **81**, 075214 (2010). http://dx.doi.org/10.1103/PhysRevB.81.075214